Studies on fluorophore-loaded polymer microbeads and luminescence lifetime encoding in flow cytometry

DISSERTATION

zur Erlangung des akademischen Grades
Doctor rerum naturalium (Dr. rer. nat.)
im Fach Physik (Spezialisierung: Experimentalphysik)

eingereicht an der Mathematisch-Naturwissenschaftlichen Fakultät
Humboldt-Universität zu Berlin
von

M.Sc. Daniel Kage

erarbeitet an der

BAM
Bundesanstalt für Materialforschung und -prüfung

Bundesanstalt für Materialforschung und -prüfung

Gutachter:
1. PD Dr. Stefan Kirstein
2. Prof. Dr. Oliver Benson
3. apl. Prof. Dr. Michael Kumke

Dekan der Mathematisch-Naturwissenschaftlichen Fakultät: Prof. Dr. Elmar Kulke
Präsidentin der Humboldt-Universität zu Berlin: Prof. Dr.-Ing. Dr. Sabine Kunst

Datum der Disputation: 04.09.2019

Zusammenfassung

Die vorliegende Dissertation umfasst zwei Themenblöcke: Zum einen wurden die optisch-spektroskopischen Eigenschaften von fluoreszenten, farbstoffbeladenen Polymer-Mikropartikeln untersucht. Zum anderen wurde die Anwendbarkeit solcher Polymer-Mikropartikel mit unterschiedlichem Lumineszenzabklingverhalten zur Erweiterung des Parameterraumes in der Durchflusszytometrie mittels Lumineszenzlebensdauer-Kodierung evaluiert.

Die Charakterisierung der farbstoffbeladenen Mikropartikel erfolgte mit diversen Methoden der optischen Spektroskopie. Am Beispiel von Polymethylmethacrylat-Partikeln, die mit dem Farbstoff Rhodamin 6G beladen wurden, konnte so ein besseres Verständnis des Einbaus der Farbstoffmoleküle und ein umfangreiches Bild der daraus resultierenden Fluoreszenz-Charakteristika gewonnen werden. Es zeigten sich spektrale Verschiebungen und eine Verbreiterung in den Fluoreszenz-Anregungs- und Emissionsspektren in Abhängigkeit sowohl des Partikeldurchmessers als auch der Farbstoffkonzentration. Zudem war eine verminderte Fluoreszenz-Quantenausbeute mit steigender Farbstoffkonzentration insbesondere bei kleinen Partikeln zu beobachten. Des Weiteren deuten Veränderungen der Fluoreszenzabklingkinetik und der Fluoreszenzanisotropie auf intrapartikuläre Energiewanderungsprozesse bei zunehmender Farbstoffkonzentration hin.
Es stellte sich heraus, dass die Beladungseffizienz eine starke Abhängigkeit vom mittleren Durchmesser der Partikel und von der Konzentration der im Polymerisationsprozess verwendeten Synthesekomponenten aufweist. Darauf basierend konnte herausgearbeitet werden, dass sich synthesebedingt eine besonders farbstoffreiche Schicht an der Oberfläche der Partikel bildet, die sich in ihren Eigenschaften wesentlich von den sterisch eingebauten Farbstoffmoleküle im Partikelvolumen unterscheidet. Hohe Farbstoffkonzentrationen in dieser Oberflächenschicht führen vermutlich zu inhomogener Farbstoffverteilung und Aggregation, was zu den beobachteten Veränderungen in den Fluoreszenzeigenschaften der Partikel führt. Diese Interpretation der experimentellen Ergebnisse konnte qualitativ durch einen Algorithmus zur Simulation der Energiewanderung auf Basis von Zufallsbewegungen bestätigt werden.

Die Anwendbarkeit der Lumineszenzlebensdauer als Kodierungsparameter in der Zeitdomäne konnte unter Verwendung eines unikalen Durchflusszytometers für zeitaufgelöste Einzelpartikel-Messungen analysiert werden. Der von einem Industriepartner grundlegend entwickelte Prototyp wurde im Rahmen dieser Arbeit getestet und optimiert. Die wohl größte Herausforderung bei der Lebensdauermessung in der Durchflusszytometrie besteht in der kurzen Interaktionszeit zwischen Objekt und Anregungslicht von wenigen zehn Mikrosekunden. Insbesondere spielen hier die Zahl der detektierten Photonen, das Signal-Untergrund-Verhältnis und die maximale vom Detektor verarbeitbare Photonendichte eine wichtige Rolle. Synthetische Daten wurden herangezogen, um den Einfluss einzelner Messparameter und -bedingungen sowie der Methode der Datenanalyse unabhängig voneinander abzuschätzen. Im Ergebnis konnte festgestellt werden, dass die Lumineszenzlebensdauer prinzipiell als Kodierungsparameter in der Zeitdomäne zugänglich ist. Auf dem bisherigen Stand der Geräteentwicklung war es möglich, drei lebensdauerkodierte Partikelpopulationen sicher zu trennen und fünf Populationen zu erkennen. Allerdings besteht weiterer Forschungs- und Entwicklungsbedarf, um eine zuverlässige und robuste Anwendung dieser Detektionsmethode in der Durchflusszytometrie zu ermöglichen.

Abstract

This thesis comprises two main topics. First, the optical-spectroscopic properties of fluorescent microbeads loaded with organic dyes were studied. In the second part, the feasibility of time-domain luminescence lifetime encoding in flow cytometry based on such microbeads that exhibit different luminescence intensity decay kinetics was assessed.

The study of the dye-loaded polymer microbeads was based on several optical-spectroscopic methods. Poly(methyl methacrylate) beads loaded with the dye rhodamine 6G were used as an example system to achieve a better understanding of the dye incorporation procedure. A comprehensive image of the fluorescence properties of these beads was developed. Spectral shifts and broadening of the fluorescence excitation and emission spectra were observed in dependence on the mean diameter of the beads and the dye loading concentration. Similarly, a significantly reduced fluorescence quantum yield was observed with increasing dye loading concentration especially in small beads. Moreover, changes in the fluorescence decay dynamics and of the fluorescence anisotropy indicated the existence of an intra-particulate energy migration process at increased dye loading concentrations.
Beads were dissolved to determine the actual dye concentration by means of absorption spectroscopy. The dye loading efficiency turned out to be strongly dependent on the mean diameter of the beads and on the amounts of certain compounds used for the bead synthesis. It was deduced that a layer with high local dye concentration forms around each bead. The properties of this layer substantially differ from those of the sterically incorporated dye molecules in the bead core. The high dye concentration in this layer results in an inhomogeneous dye distribution and aggregation accompanied by the respective changes of the fluorescence characteristics of the beads. A simulation of the energy migration process based on a random walk algorithm confirmed the interpretation of the experimental results.

For the assessment of luminescence lifetime encoding in time-domain flow cytometry, a unique setup with capabilities for time-resolved single-particle measurements was used. This prototype device was provided by a project partner. It was tested and optimized in the course of this study. The main issue of lifetime determination in flow cytometry is represented by the short interaction time of only tens of microseconds of the objects with the excitation light spot. Especially the achievable photon counts, the signal-to-background ratio and the acceptable maximum light intensity impinging on the detector are crucial. Synthetic data were used to study certain measurement parameters and conditions as well as the data analysis procedure independently of other influences. As a result, luminescence lifetime is generally applicable as an encoding parameter in time-domain flow cytometry. At the current state of development, three populations can be separated based on their lifetime codes and five populations are distinguishable. However, further research and development is needed to ensure reliability and robustness in applications.

Contents

Abbreviations and notation vii

1. Introduction 1

2. Theoretical basics 3
2.1. Molecular structure . . . 3
2.2. Interaction of molecules and light . . . 6
2.3. Excited state dynamics, radiative decay and quenching mechanisms . . . 9
2.4. Impact of the surrounding . . . 11
2.5. Excitation energy transfer and migration . . . 11

3. Experimental methods 15
3.1. Absorption spectroscopy . . . 15
3.2. Photoluminescence spectroscopy . . . 16
3.2.1. Steady-state photoluminescence spectroscopy . . . 17
3.2.2. Time-resolved photoluminescence spectroscopy . . . 17
3.2.3. Photoluminescence anisotropy measurements . . . 19
3.2.4. Inner filter effects . . . 20
3.3. Confocal laser scanning microscopy . . . 20
3.4. Flow cytometry . . . 21
3.5. Bead synthesis . . . 23

4. Optical-spectroscopic characteristics of dye-loaded polymer microbeads 25
4.1. The dye loading concentration . . . 26
4.2. Optical spectroscopy . . . 30
4.2.1. Steady-state fluorescence spectroscopy . . . 31
4.2.2. Time-resolved fluorescence spectroscopy . . . 32
4.2.3. Fluorescence anisotropy . . . 35
4.2.4. Fluorescence quantum yield . . . 38
4.2.5. Synopsis . . . 40
4.3. Random walks for energy migration simulation . . . 42
4.3.1. Shape of the dye distribution . . . 46
4.3.2. Thickness of the quenching shell . . . 50
4.3.3. Mean dye molecule distance . . . 51
4.3.4. Bead diameter . . . 53
4.4. Summary . . . 55

5. Luminescence lifetime encoding in flow cytometry **57**
5.1. Characterization of suitable lifetime-encoded luminophore systems 58
5.2. Simulated decay curves and lifetime determination 59
5.3. Assessment of instrument capabilities and data analysis 60
5.3.1. Photon count number 61
5.3.2. Signal-to-background ratio 63
5.3.3. Time range 65
5.3.4. Bin width 67
5.3.5. Detector operating range 68
5.3.6. Flow speed 70
5.3.7. Synopsis 71
5.4. Encoding capabilities 72
5.5. Application of lifetime encoding 73
5.6. Summary 76

6. Conclusions & Outlook **77**

A. Appendix **81**
A.1. Measurement artifacts due to bead concentration effects 81
A.2. Mathematical background for the random walk simulations of energy migration . . 84
A.2.1. Generation of dye molecule distributions 84
A.2.2. Parameters 86
A.3. Convergence behavior and reproducibility of the random walk simulations 86
A.4. Numerical simulation of luminescence decay curves 87
A.4.1. Analytical approach for mono-exponential decays 88
A.4.2. Von Neumann rejection for multi-exponential decays 88
A.5. Analytical expression for the standard deviation of lifetimes obtained from curve fitting 90

Bibliography **91**

Danksagung **99**

Selbstständigkeitserklärung **101**

Abbreviations and notation

Abbreviation	Description
AO	Atomic orbital
AOT	Aerosol-OT (dioctyl sulfosuccinate)
BP	Bandpass
BS	Beam splitter
CLSM	Confocal laser scanning microscopy
DM	Dichroic mirror
FCM	Flow cytometry
FL	Fluorescence channel (FCM)
FLIM	Fluorescence lifetime imaging microscopy
FRET	Förster resonant energy transfer
FSC	Forward scatter channel (FCM)
FWHM	Full width at half maximum
IR	Infrared
IRF	Instrument response function
K30/K90	PVP chain lengths
LP	Longpass filter
LT	Lifetime (excited state, photoluminescence, fluorescence)
M	Mirror
MCP	Microchannel plate or multichannel plate
MO	Molecular orbital
ND	Neutral density filter
NIR	Near-infrared
PMMA	Poly(methyl methacrylate)
PMT	Photomultiplier tube
PRNG	Pseudo-random number generator
PVP	Polyvinylpyrrolidone
QD	Quantum dot
QY	Quantum yield (photoluminescence, fluorescence)
Rh6G	Rhodamine 6G
SSC	Side scatter channel (FCM)
TCSPC	Time-correlated single photon counting
TRANES	Time-resolved area-normalized emission/excitation spectrum
TRES	Time-resolved emission/excitation spectroscopy/spectrum
UV	Ultraviolet

Symbol	Description
A	Absorbance or amplitude in decay functions
A_{bead}	Surface area of a bead
B	Background in decay functions
c, c_{dye}	Molar concentration
c_{beads}	Mass concentration (beads)
c_{nom}, c_{eff}	Nominal and effective dye loading concentration in beads
d_{dd}, d_{hk}	Dye-dye distance
d_{qs}	Thickness of the quenching shell
D	Diameter (of beads)
f	Dye loading efficiency (beads)
$F_{\mathrm{D}}(\lambda)$	Normalized emission spectrum
G	Correction factor (anisotropy)
h	Identifier of a random molecule
I, I_{M}, I_0, I_{S}, $I_{\parallel/\perp}$	Intensity (signal, luminescence), model intensity, initial intensity, steady-state intensity, intensity at different polarizer orientations
j	Bin index for binned data, general summation or identifier index
k	Identifier of a random molecule or number of bins
k_{B}	Boltzmann constant
l	Path length (cuvette)
m_{beads}	Mass of dissolved beads
n	Refractive index or integer to enumerate states etc.
M	Number of runs
n^*	Density of excited molecules
N	Number of atoms in a molecule or photon counts
N_{A}	Avogadro constant
p, P	Probability density, probability
$\vec{Q}, \vec{q}$	Nuclear/electronic coordinates
r	Anisotropy or distance or radial coordinate or auxiliary variable
R	Radius of a bead
R_{F}	Förster radius
S_n	Singlet state n
SBR	Signal-to-background ratio

Symbol	Description
SD, $SD_{\mathrm{num/ana}}$	Standard deviation, numerically or analytically determined
t	Time
T_n	Triplet state n
T	Temperature or transmittance
V	Volume
V_{bead}	Volume of a single bead
V_{beads}	Volume of beads
V_{mol}	Volume per molecule
V_{sol}	Solvent (sample) volume
$w(x)$,$w'(x)$	Probability distribution
x, y, z	Cartesian coordinates
α_r, α_ϑ	Normalization constants
$\alpha^{(*)}$, $\beta^{(*)}$	Proportionality constants
γ, γ_{ra}, γ_{iq}, γ_{eq}, γ_{ET}, γ_{t}	Luminescence decay rate constants, radiative, internal/external quenching, energy transfer, transfer step
ϵ, ϵ_{A}	Molar absorption coefficient (acceptor)
η	Viscosity or exponent in probability distribution
ζ, ζ', ζ^*	Uniformly distributed random variable
ϑ	Polar angle
θ	Upper integration limit
Θ	Rotational correlation time
κ	Orientation factor
λ, $\lambda_{\mathrm{fl,ex}}$, $\lambda_{\mathrm{fl,em}}$, λ_{det}	Wavelength, excitation, emission, detection
ξ	Random variable
ρ_{PMMA}	Mass density of PMMA
τ, τ_{ra}, τ_0, τ_{mean}, τ_{m}	Luminescence lifetime, radiative, undisturbed, mean, maximum
τ_{ref}, τ_{cal}, τ_{not}	Reference, calculated, notional lifetimes
φ	Azimuthal angle
ϕ_{fl}, ϕ_0, ϕ_{exp}	Quantum yield (fluorescence), undisturbed QY, experimental
$\psi_{\mathrm{c/e}}$	Nuclear/electronic wave function
Ψ	Molecular wave function

1. Introduction

The use of photoluminescence-based techniques is widespread among bioanalytics, medical diagnostics, and other research areas [1–4]. Many analytical methods that are based on fluorescence detection rely on encoding strategies to distinguish between different analytes or labels [5]. In these cases, encoding is commonly based on fluorescence intensity measurements or readout of spectral characteristics via intensity ratios to identify the respective analytes. Typical examples are bead-based (immuno)assays or the investigation of labeled cells in flow cytometry [5–8]. Flow cytometry is an important tool for biomedical research that is highly dependent on multiplexed labeling. However, the common encoding strategies suffer from issues such as the sensitivity to random fluctuations of the excitation intensity or due to noise in the case of intensity encoding and the spectral overlap of different labels in the case of spectral encoding. Both limit the number of codes that can be employed. Scientific questions, however, will rather become more complex than simpler and the need for higher degrees of multiplexing is already present nowadays [2, 3, 9]. Hence, it is advisable to consider other options of encoding for analytical purposes. Luminescence lifetime encoding in general [10–17] and for flow cytometry in particular [18–24] is a concept that has already been discussed for decades and occasionally applied. The idea behind lifetime encoding is to discriminate different labels or autofluorescent analytes based on their characteristic luminescence lifetime. There are two potential advantages of this approach. On the one hand, the luminescence lifetime could be used as an additional source of information during measurements [25]. Thereby, it either reduces classification uncertainty or it acts as a stand-alone encoding parameter to allow an increased number of codes as demanded. On the other hand, fast and affordable electronics could replace sophisticated optical setups [26]. Even for low degrees of spectral multiplexing, multiple excitation light sources and detectors are required. Instead, a single pulsed light source and a detector with suitable readout electronics can be used to reduce costs and complexity of instrumentation. However, high-throughput techniques, such as flow cytometry, only allow measurement times on the order of tens of microseconds per object (e.g. cells, particles, beads). The determination of luminescence lifetimes within such a short time remains challenging and thus lifetime encoding does not play a role in routine applications yet.

There are two main classes of techniques for time-resolved measurements [18]: time-domain and frequency-domain techniques. Both approaches are theoretically equivalent in terms of time resolution [27]. Generally, frequency-domain methods require higher signal intensities than time-domain methods and the time-domain representation of a decay curve can simplify data interpretation. So far, however, most literature reports on time resolved measurements for flow cytometry have frequency-domain methods [24, 28–31] and specific applications [32–37] as their subjects of discussion. There are few reports on time-domain measurements in microfluidic systems and flow cytometry [38–40]. Nevertheless, a systematic study of capabilities and limits of time-domain methods for lifetime determination and encoding in high-throughput techniques with short inter-

action times and low photon count numbers seems to be currently lacking, though it could be useful for analytical and scientific applications at lower available signal intensities.

Carrier systems for multiplexing codes are often luminophore-loaded micron-sized polymer beads [7, 41], particularly for bead-based assays. Moreover, such beads serve as tools for calibration and instrument performance control in optical microscopy and flow cytometry [42–48]. Such applications require a high degree of reproducibility, not only but especially, in terms of optical-spectroscopic properties. Considering the increasing precision, complexity, and versatility of measurement techniques, the quality requirements on these microbeads are increasing and will continue to do so. Despite this development, the body of literature on polymer-encapsulated dyes mainly deals with nanometer-sized particles [49] or non-particulate systems such as thin polymer films [50]. Studies on micron-sized beads often describe the preparation and application but do not detail optical-spectroscopic properties [51].

Accordingly, there are two foci for this work.
One chapter is devoted to a study of the optical-spectroscopic properties of dye-loaded polymer microbeads [52]. Beads made of poly(methyl methacrylate) (PMMA) that were loaded with rhodamine 6G (Rh6G) were subject to an in-depth investigation. The optical properties of PMMA and the wide-spread use of Rh6G for different purposes make this combination a reasonable starting point. The aim was to achieve a more comprehensive understanding of the dye incorporation process, the influence of the dye loading concentration, and the impact of the size of the beads on their fluorescence characteristics. Besides the spectral properties, also the fluorescence decay dynamics, anisotropy, and quantum yield were investigated. Moreover, the dependence of the dye incorporation efficiency on synthesis conditions was determined and conclusions regarding the dye distribution could be drawn. Based on these optical-spectroscopic measurements of dispersed bead ensembles, a theory describing the observed features was developed. This theory was supported by the results from a random walk algorithm for the simulation of energy migration in these beads.
Another chapter provides a basic assessment of luminescence lifetime encoding in time-domain flow cytometry [53]. A prototype flow cytometry setup with capabilities for time-resolved measurements on the nanosecond time scale was tested and optimized using a set of lifetime-encoded polymer beads as a reference system. Additionally, synthetic data was generated and analyzed to study the impact of single parameters decoupled from other effects. Based on experiments and simulations, the impact of the number of accumulated photons, the signal-to-background ratio, the time-resolution, as well as some aspects of data analysis and detector characteristics could be examined. Finally, the feasibility of lifetime encoding in time-domain flow cytometry in one spectral channel and simultaneous readout of a spectrally different intensity signal in another spectral channel could be demonstrated.

A brief introduction to the theory of photoluminescence of molecular systems is given in Chap. 2 followed by descriptions of the employed experimental techniques in Chap. 3. The properties of Rh6G-loaded PMMA microbeads are discussed in Chap. 4 and the studies on lifetime encoding in flow cytometry are presented in Chap. 5. A final summary with suggestions for future work is given in Chap. 6.

2. Theoretical basics

This chapter is devoted to the theoretical basics of molecular photoluminescence and molecular interactions relevant to the results discussed later. The concepts and theories provided here can be found in standard textbooks on molecular photophysics and optical spectroscopy [1, 27, 54–60].

2.1. Molecular structure

The electronic structure of a molecular system is determined by the interaction between the atoms it consists of. Thus, in theory, knowing the quantum mechanical wave function that exactly describes the entirety of all electrons and nuclei in a molecule would allow the prediction of its properties. However, already on the level of single atoms the form of the corresponding Hamiltonian that encompasses all interactions often becomes excessively intricate and the resulting Schrödinger equation cannot be solved analytically. Therefore, simplifications and intuitive approaches to an approximation of molecular structure are unavoidable. A key approximation is the assumption that nuclear motion and electronic motion can be represented by decoupled wave functions. This is the Born-Oppenheimer approximation which is based on the idea that electrons can follow nuclear motions quasi-instantaneously due to the considerable mass difference [55, 58]. Consequently, the overall wave function $\Psi(\vec{q},\vec{Q})$ of a molecular system may be separated into a product of a nuclear wave function ψ_c and an electronic wave function ψ_e. The nuclear wave function ψ_c only depends on the nuclear coordinates $\vec{Q}$. The electronic wave function ψ_e depends on the electronic coordinates $\vec{q}$ and contains the nuclear coordinates as parameters. Thus, we can write [58]

$$\Psi(\vec{q},\vec{Q}) = \psi_\mathrm{e}(\vec{q}|\vec{Q})\psi_\mathrm{c}(\vec{Q})\,.$$

The nuclei and the electrons may now be inspected independently of each other. An established approach to characterize the electronic structure of a molecule is to view the interaction between the electrons of the component atoms in terms of atomic orbitals (AOs) that overlap and form molecular orbitals (MOs). Smaller AOs that are lower in energy will overlap less than spatially extended ones with higher energy. Thus, mostly the outer orbitals determine atomic interaction in molecules. The MOs formed by the AOs determine how the electrons distribute around the backbone of nuclei and how strong and directed bonds between the atoms are. Even more important for optical spectroscopy is that the energetic landscape of the MOs also defines optically active transitions of a molecule. Two overlapping AOs form a pair of one bonding and one anti-bonding MO. Those AOs that basically stay unaffected represent non-bonding MOs that mostly maintain the shape of the original AO. Depending on the type of overlap, MOs are further divided into two subtypes [57]. When the involved AOs have overlap collinear along the bond that they form, the resulting MO is called a σ orbital. In case of lateral overlap of the AOs, the resulting MO is a π orbital.

The electrons in a molecule occupy the MOs, maximum two electrons in the same orbital due to the Pauli exclusion principle. The electronic state of the molecule should be strictly distinguished from the occupation configuration of the MOs. The electronic configuration determines the electronic state of the molecule, but the electronic state of the molecule only considers the molecule as a whole. This idea is depicted in the energy diagram of MOs and the resulting molecular states in Fig. 2.1. Typically, only the highest occupied MOs and therefore only a limited number of electrons are considered since the lower MOs are not involved in common photophysical processes [54]. In the example, this is a bonding π orbital, a non-bonding orbital and an anti-bonding π^* orbital. The electronic ground state of the overall molecule is obtained when the electrons only fill the

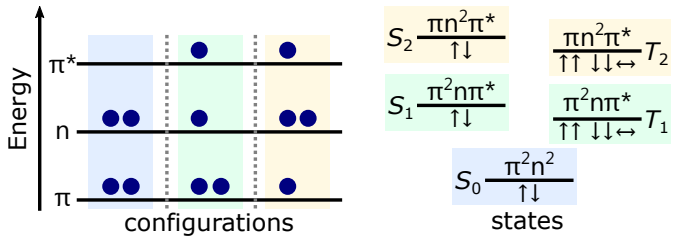

Figure 2.1: Illustration of molecular orbitals and states (based on [54]). On the left side, different occupation schemes of molecular orbitals are shown. The right side gives the resulting states of a molecule.

MOs lowest in energy. Here, the four electrons considered reside in a bonding π orbital and a non-bonding orbital. The ground state has a multiplicity of one since all MOs are occupied with two electrons with anti-parallel paired spins ('out of phase' [54]). It will be denoted S_0 for being the lowest singlet state. When the molecule is in an excited electronic state, at least one electron occupies a higher MO. Thus, two singly occupied MOs occur. Here, the Pauli principle does not necessarily require paired anti-parallel spins. Anyway, the spins could still be anti-parallel giving rise to an excited singlet state S_n, where n is some integer number. However, they could also combine to be both parallel up, both parallel down, or one up and one down but with non-vanishing net spin ('in phase' [54]). These three states are usually viewed as one molecular state which is called a triplet state T_n, where n is some integer number usually excluding 0 as the ground state is often a singlet state. The triplet states are always slightly lower in energy than the respective singlet states with the same number n as the unpaired electrons correlate their motion differently to increase their mean distance in the triplet states (exchange interaction) [54]. Thus, the occupation of the same MOs can result in different molecular states depending on the spin orientation. In the given example, the first excited singlet and triplet states (S_1 and T_1) arise from an electron occupying the anti-bonding π^* orbital instead of the non-bonding orbital. The second excited states are based on an electron from the bonding π orbital being promoted to the anti-bonding π^* orbital. In many optically active substances, there is a system of π orbitals that is delocalized over a large fraction of the molecule and determines its optical-spectroscopic properties.

So far, we only focused on the electronic structure. However, the molecule as a whole can be subject to vibrations and rotations in addition. According to the Born-Oppenheimer approximation, the electron cloud is assumed to quasi-instantaneously follow the nuclear movement. In the case of

non-linear molecules with N atoms there are $3N - 6$ degrees of freedom for each, vibrational and rotational motion [55]. For linear molecules, both numbers increase to $3N - 5$. Since vibrational energy and angular momentum are quantized, vibrational and rotational motion add discrete energy levels to the molecular states. Thus, the molecular electronic states depicted in Fig. 2.1 are extended by a set of vibrational energy levels which in turn are further accompanied by a set of rotational levels. The energy of molecular vibrations is determined by the electrostatic interactions within the bonds and between the nuclei. Several approximations for this interaction exist. To a first approximation, molecular bonds may be viewed as harmonic oscillators and molecules as rigid rotors [55]. Figure 2.2 shows the potential energy curve of a Morse potential [60] and the

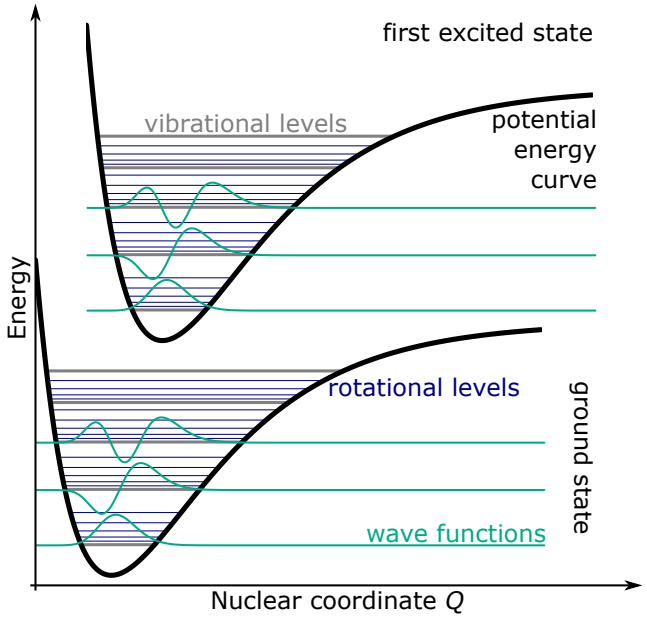

Figure 2.2: Potential energy curves for a Morse potential for the ground state and the first excited state. The gray horizontal lines indicate the energy of the vibrational levels. The blue horizontal lines represent rotational energy levels. The wave functions are displayed as cyan curves.

corresponding vibrational energy levels as well as the wave functions are displayed by the gray horizontal lines and the cyan curves. Typical energy levels of rotational motion are indicated by the blue horizontal lines. The corresponding energy differences between vibrational and rotational states are, much smaller than those of the electronic states. As a rule of thumb, electronic states usually have energy differences on the order of eV, vibrational states differ by hundreds of meV, and rotational states are only several meV apart from each other [56]. Consequently, molecules at room temperature are usually found in some excited rotational state but in the vibrational ground state.

2.2. Interaction of molecules and light

Transitions between the states of molecules are due to uptake or release of the energy amount that corresponds to the energy difference between the two involved states. For the electronic states of a molecular system this commonly includes the absorption or emission of photons in the ultraviolet (UV), visible, or near-infrared (NIR) range which is the core of photoluminescence spectroscopy. Other types of spectroscopy [55] such as Raman spectroscopy or IR absorption spectroscopy will not be discussed.

The transitions between molecular states have to obey different quantum-mechanical selection rules [54–56] which may not always be strictly predictable since they are based on properties of the molecular wave function in the initial and final state of the transition. Here, we only consider electronic excitation by absorption of a photon and the subsequent transitions back to the ground state. The involved processes can be summarized in a Jabłoński diagram [27] as shown in Fig. 2.3. The diagram displays the molecular singlet and triplet states similar to Fig. 2.1. In addition, it

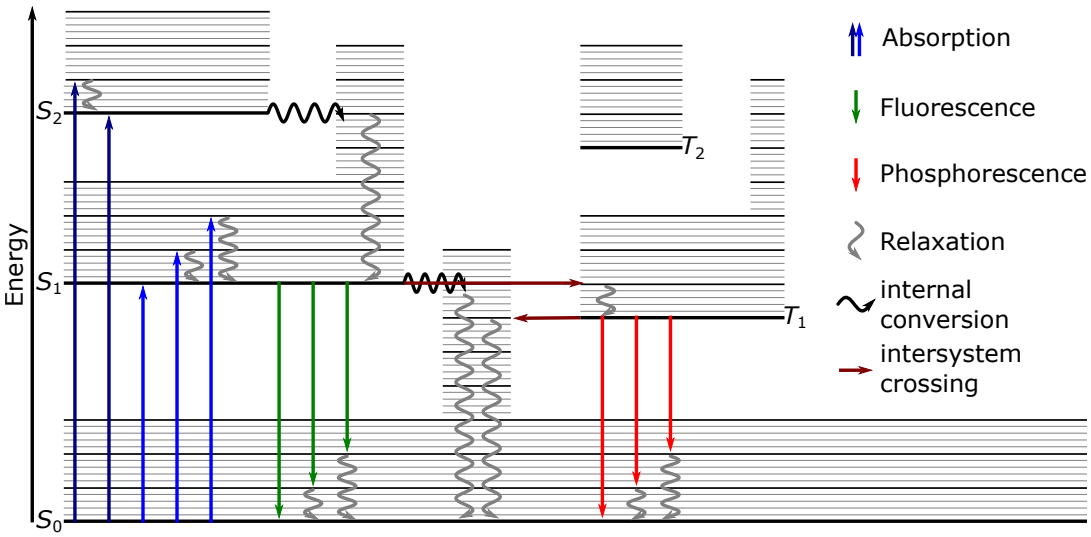

Figure 2.3: A Jabłoński diagram (based on [27]). Excitation of a molecule by absorption of photons is indicated by the blue arrows. Upon excitation to a higher singlet state or a higher vibrational level, the molecule usually goes to the vibrational ground state of the first excited singlet state by internal conversion and relaxation. De-excitation of the molecule is possible by numerous processes such as intersystem crossing and subsequent phosphorescence, internal conversion, or fluorescence.

comprises vibrational and rotational sublevels explained in Fig. 2.2. We will now go through an overview of the cycle starting with excitation from the ground state by absorption of a photon and ending again in the ground state by de-excitation due to different pathways.

1. Absorption
   At room temperature, the thermal energy ($k_\mathrm{B}T \approx 25$ meV for $T \approx 293$ K) is significantly smaller than typical energy differences between vibrational states. Thus, molecules are usually found in the vibrational ground state of the electronic ground state S_0. Excited rotational states, however, may be occupied. Upon absorption of a photon, the molecule is brought to an excited electronic singlet state, typically S_1, possibly a higher singlet state. The process of absorption happens within femtoseconds [54]. Depending on the photon energy, the molecule might also have vibrational energy after excitation. Direct excitation to triplet states would require interaction of the electron spin and the photon to conserve angular momentum. This interaction is often negligible.

2. Vibrational relaxation
   Collisions or close-contact interaction with other molecules and, seldomly, low-energy photon emission [55] will bring the molecule to the lowest vibrational level of the excited electronic state. This relaxation takes place within several picoseconds and is much faster than most other processes that can occur.

3. Internal conversion
   From an excited singlet state, the molecule might go to a lower-lying singlet state by entering an iso-energetic vibrational level of the lower electronic state. This is the common pathway for bringing the molecule from a higher singlet state S_n to the first excited singlet state S_1.

4. Fluorescence
   The emission of a photon upon transition from a higher singlet state S_n to the ground state S_0 is called fluorescence. Kasha's rule states that fluorescence almost exclusively occurs from the first excited singlet state S_1 [1]. The molecule might reach an excited vibrational state of the electronic ground state and thus fluorescence can be followed by additional vibrational relaxation.

5. Intersystem crossing
   Transitions between singlet and triplet states are usually forbidden due to conservation of angular momentum (which includes spin). It may, however, be more likely in molecules that exhibit stronger spin-orbit coupling, e.g. due to the presence of heavier atoms [54].

6. Phosphorescence
   The emission of a photon upon transition from a triplet state to the ground state is called phosphorescence. As with intersystem crossing, this is spin-forbidden and only occurs under certain circumstances. Therefore, phosphorescence is characterized by much longer decay times and should be distinguished from fluorescence.

The energy differences between initial and final states in a transition translate into the energy of the absorbed or emitted photons and therefore the spectral characteristics of a molecule. The probabilities for the different transitions to occur govern the excited state dynamics and consequently define how long on average a molecule resides in a certain state and which pathways are preferred in de-excitation.

The probabilities for the processes listed above to occur and compete with each other depend on the quantum-mechanical matrix elements that describe them [54–56]. The resulting selection rules, e.g., forbid transitions involving a change in multiplicity. However, such restrictions may be lifted in certain molecules so that not all of these transitions are strictly forbidden but rather just have much lower probability than others.
Upon excitation to a higher excited singlet state S_n, internal conversion to a lower singlet state is much more likely than fluorescence. The reason is the relatively small energy differences between the higher electronic states that allow for larger overlap of the wave functions of iso-energetic vibrational levels from two different singlet states [27]. Therefore, the probability for an iso-energetic transition to a higher vibrational level of a lower electronic state (black horizontal arrows in Fig. 2.3) is larger than that for a radiative transition between the singlet states. The energy difference between S_1 and S_0, however, is large enough to drastically decrease the overlap between the vibrational levels of these states and therefore fluorescence is favored. A practical consequence of this behavior is that the emission characteristics of a molecule are usually independent of the excitation wavelength as according to Kasha's rule fluorescence mostly occurs from S_1.
The general principle of vibrational wave function overlap, called the Franck-Condon principle, also determines which transitions between the vibrational levels of S_0 and S_n are favored. Due to the Born-Oppenheimer approximation, it is assumed that electronic transitions are 'vertical', i.e., they proceed without changes in the nuclear coordinates. If the nuclear geometries of the electronic ground state and the excited state are similar, then the transition between same vibrational levels has the highest probability and the spacing of the vibrational levels is similar as well. When the

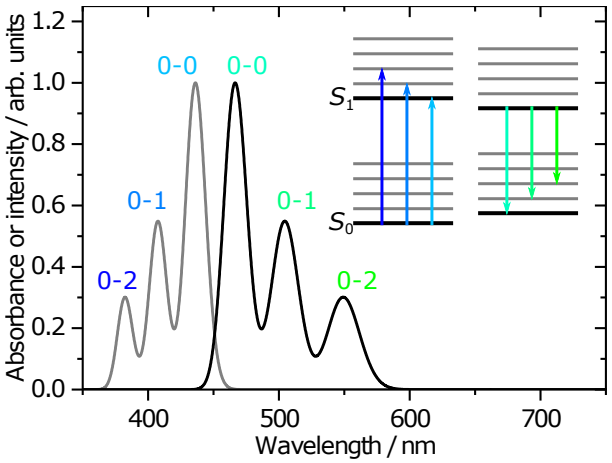

Figure 2.4: Absorbance and fluorescence emission spectra of a fictive substance. Excitation starts from the solvent-relaxed S_0 and goes to S_1 not in equilibrium with the solvent. The three indicated transitions correspond to the three peaks in the absorbance spectrum. Solvent relaxation lowers S_1 in energy. Emission occurs to higher vibrational levels of S_0 not in equilibrium with the solvent. Each indicated transition corresponds to one peak in the emission spectrum. The energy difference between the $0-0$ transition stems from the solvent relaxation.

geometries differ, this behavior changes. This can be seen in Fig. 2.2: due to the shift of the equilibrium coordinate and possible differences in the shape of the potential energy curve between the electronic ground state and excited state, the wave function overlap of states with unequal vibrational energy can be increased. Transitions between these states with larger wave function overlap exhibit a higher probability. This translates to the spectral intensity of certain peaks in absorbance and emission spectra that represent the respective transitions. Due to the Franck-Condon principle, the fluorescence spectrum often resembles a mirror image of the absorbance spectrum which is depicted in Fig. 2.4. Here, the transitions between the vibrational levels are assigned to peaks in artificial absorbance and fluorescence emission spectra. As a result of the relaxation to the vibrational ground state, significant fractions of the fluorescence emission occur at longer wavelength than absorption. This is termed the Stokes shift. The Stokes shift can also be defined as the (energy) difference between the spectral positions of the maxima in absorption and emission [61]. If the transitions between the vibrational ground states were most probable, one would expect zero Stokes shift since the energy gap in the Jabłoński diagram, Fig. 2.3, is the same for both absorption and emission. However, the Franck-Condon principle is not the only source of Stokes shift. Usually, the fluorophores arrange in an energetic minimum with their surrounding, e.g. solvent molecules. Since electron distribution and possibly also the nuclear geometries differ between ground state and excited state, the fluorophore and solvent molecules will rearrange in the excited state to lower its energy [27]. Thus, the energy gap between the ground state in equilibrium with the environment and the excited state not in equilibrium is larger than the energy gap between the excited state in equilibrium and the ground state not in equilibrium with the environment. Therefore, also the transitions between the vibrational ground states can exhibit an energy gap as indicated in Fig. 2.4.

2.3. Excited state dynamics, radiative decay and quenching mechanisms

According to Kasha's rule and due to vibrational relaxation, an excited molecule usually returns to the vibrational ground state of the first excited electronic state S_1 by internal conversion within several picoseconds [1, 27]. The lifetime τ of S_1, i.e. the average time that the molecule resides in the excited state, is commonly on the order of nanoseconds [54]. It is determined by the rate constants of the possible de-excitation pathways. The molecule might fluoresce, which is a radiative decay with the associated rate constant γ_{ra}. Alternatively, there are two major non-radiative decay channels [56]: internal conversion and intersystem crossing, which can be summarized as internal quenching with a rate constant γ_{iq}. Intersystem crossing could, theoretically, be followed by phosphorescence emission which would count as a radiative pathway. For most organic fluorophores, the probability is very low and the triplet state energy may rather be dissipated by another intersystem crossing and internal conversion [56]. This means, the overall decay rate constant neglecting phosphorescence and additional external quenching is

$$\tau^{-1} = \gamma = \gamma_{\mathrm{ra}} + \gamma_{\mathrm{iq}}\,. \tag{2.1}$$

An ensemble of excited molecules with density n^* therefore decays with time t according to

$$\begin{aligned} \frac{\mathrm{d}n^*}{\mathrm{d}t} &= -(\gamma_{\mathrm{ra}} + \gamma_{\mathrm{iq}})n^* \\ n^*(t) &= n_0^* \mathrm{e}^{-(\gamma_{\mathrm{ra}}+\gamma_{iq})t} = n_0^* \mathrm{e}^{-\gamma t}\,, \end{aligned} \tag{2.2}$$

where n_0^* is the initial density of excited molecules. Thus, for an ensemble of excited molecules with identical rate constants, the resulting decay of the excited state population is mono-exponential. The corresponding fluorescence intensity decay is

$$I(t) \sim \gamma_{\mathrm{ra}} n^*(t) = \gamma_{\mathrm{ra}} n_0^* \mathrm{e}^{-\gamma t}\,, \tag{2.3}$$

which consequently is a mono-exponential function as well. If the decay behavior observed in an experiment is not mono-exponential, there are various possible reasons. Multi-exponential decay could be caused by the presence of different fluorescent species or microenvironmental differences across the sample volume under investigation. Deviation from mono-exponential decay kinetics might also be caused by intermolecular quenching, which in addition shortens the decay time [27]. A definition of the excited state lifetime independent of a certain decay function is given by [1]

$$\tau = \frac{\int_0^\infty t I(t)\,\mathrm{d}t}{\int_0^\infty I(t)\,\mathrm{d}t}\,. \tag{2.4}$$

Quenching processes can be dynamic or static. Dynamic quenching adds an additional decay channel to the system that competes with the intrinsic ones. In the simplest case, this is another rate constant for external quenching, γ_{eq}, that is added to Eq. (2.1):

$$\gamma = \gamma_{\mathrm{ra}} + \gamma_{\mathrm{iq}} + \gamma_{\mathrm{eq}}\,. \tag{2.5}$$

Dynamic quenching happens in the excited state and therefore occurs simultaneously with the other de-excitation pathways. It consequently alters the decay kinetics by at least shortening the fluorescence lifetime. In contrast, static quenching requires a modification (e.g. complex formation) that already occurs in the ground state. A statically quenched system may still absorb light but radiative transition back to the ground state is prohibited. Since statically quenched systems are commonly assumed to not emit light at all, they do not contribute to the fluorescence emission in any way and therefore do not alter the decay dynamics [1].

The fluorescence quantum yield ϕ_{fl} is defined as the ratio of the number of emitted photons and the number of absorbed photons. It is related to the overall rate constant γ and the radiative rate constant γ_{ra} by

$$\phi_{\mathrm{fl}} = \frac{\gamma_{\mathrm{ra}}}{\gamma}\,.$$

Consequently, dynamic quenching affects the effective decay rate as well as the quantum yield such that the change in quantum yield and the change in the effective lifetime $\tau = \gamma^{-1}$ are proportional,

$$\tau = \tau_{\mathrm{ra}} \phi_{\mathrm{fl}}\,, \tag{2.6}$$

as long as the radiative lifetime $\tau_{\mathrm{ra}} = \gamma_{\mathrm{ra}}^{-1}$ stays the same. Static quenching also reduces the quantum yield but does not alter the decay kinetics as it leaves the non-quenched molecules unaffected. Thus, dissimilar variations in decay kinetics and quantum yield indicate a mixture of both processes.
The fluorescence quantum yield is usually independent of the excitation wavelength. This rule of thumb is known as Vavilov's law [1] and rests on the same physical principles as Kasha's rule.

2.4. Impact of the surrounding

The surrounding of a luminophore has a multitude of effects on its photophysical properties [1, 27] and only a very brief selection shall be mentioned here. Amongst other factors and depending on the specific transitions of the luminescent system under consideration, the viscosity, polarity, and proticity of the surrounding matrix, the capability to form hydrogen bonds, as well as the refractive index can have an impact on the properties of a luminophore. Furthermore, the pH value and the presence of gases (e.g. oxygen, nitrogen oxides, carbon oxides) or metal ions, and also the temperature can change the optical-spectroscopic properties of a luminescent system.

The viscosity of a matrix influences the mobility of luminophores with the special case of solid matrices that restrict lateral movement to a great extent and reduce rotational freedom. The ability of a fluorophore to change its orientation during the exited state lifetime has an impact on the observable fluorescence anisotropy, see also Sec. 3.2.3. Further impact on the spectral properties can be due to solvent polarity. This is often used as a keyword to address spectral shifts or the solubility limit which has an influence on the formation of aggregates or complexes. However, it is actually too simplifying to encompass the complex interaction of solute and solvent [27]. Beyond that, the dielectric environment, namely the refractive index, modifies the radiative rate constant. The temperature influences decay rates and varies the mobility and thereby possible quenching due to diffusion as well as it changes the probability for occupation of rotational and vibrational levels.

2.5. Excitation energy transfer and migration

Excitation energy can be transferred from one molecular system, the donor, to another one, the acceptor. Such an energy transfer may either be radiative or non-radiative [27]. The radiative transfer is a simple emission of a photon from the donor and subsequent absorption by the acceptor. Non-radiative transfer is based on mechanisms different from photon exchange. The most common is Förster resonant energy transfer (FRET), which is a dipole-dipole interaction on the scale of several nanometers [27, 62]. As the term 'resonant' indicates, the energy transfer only works when there is a set of two states in the donor whose energy difference matches that of two states in the acceptor. From a spectroscopic point of view, this means that a fundamental prerequisite for both radiative and non-radiative transfer is the overlap of the donor emission spectrum and the acceptor absorption spectrum.

This is shown in Fig. 2.5 for two fictive substances D and A. If the donors and acceptors are chemically different, it is called a heterotransfer. For chemically identical donors and acceptors, it is a homotransfer. The spectra in Fig. 2.5 show three possibilities: heterotransfer $D^* \rightarrow A$ as well as homotransfer $A^* \rightarrow A$ and $D^* \rightarrow D$. In a homotransfer, the overlap of the absorption and

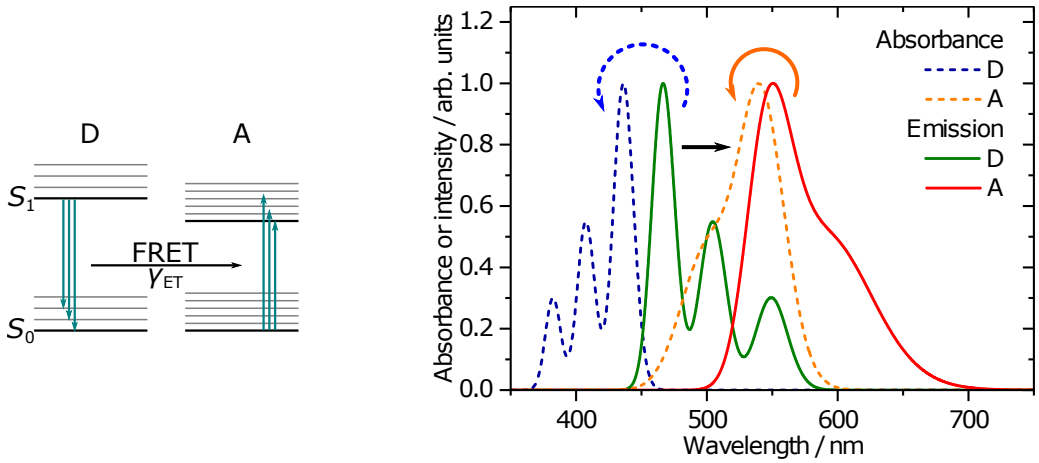

Figure 2.5: Energy diagram and artificial absorbance and fluorescence emission spectra of two fictive substances D and A. Based on the spectral overlap, there could be significant energy transfer from D^* to A (black arrow). Moreover, homotransfer (orange and blue arrow) would occur in substance A ($A^* \rightarrow A$) and, to a lower extend due to the different Stokes shift, in substance D ($D^* \rightarrow D$).

luminescence emission spectrum is closely related to the Stokes shift: a small Stokes shift leads to larger overlap, a large Stokes shift results in weak overlap. That is why the homotransfer in the example of Fig. 2.5 would potentially be more efficient among A than among D.

The impact on the optical-spectroscopic properties is different between radiative and non-radiative transfer. Radiative transfer does not influence the properties of the donor or acceptor on the molecular level. Non-radiative transfer, in contrast, changes the decay kinetics of the donor as it introduces another decay channel with rate constant γ_{ET} to Eq. (2.5):

$$\gamma = \gamma_{\mathrm{ra}} + \gamma_{\mathrm{iq}} + \gamma_{\mathrm{eq}} + \gamma_{\mathrm{ET}} \,.$$

An additional decay channel such as FRET will lead to faster decay, i.e. shorter excited state lifetime. The value of γ_{ET}, however, might differ across an ensemble of donors depending on the nature of the transfer process and the distribution of the donors and acceptors. In the case of FRET, the rate constant for a donor-acceptor pair separated by a distance r from each other is given by [27]

$$\gamma_{\mathrm{ET}} = \frac{1}{\tau_0} \left(\frac{R_{\mathrm{F}}}{r} \right)^6$$

where τ_0 is the donor lifetime in absence of acceptors and R_{F} is the so-called Förster radius. The Förster radius determines the distance at which the transfer rate constant γ_{ET} equals the undis-

turbed fluorescence decay rate constant τ_0^{-1} of the donor. The Förster radius can be calculated from a normalized fluorescence emission spectrum $F_\mathrm{D}(\lambda)$ of the donor and the molar absorption coefficient $\epsilon_\mathrm{A}(\lambda)$ of the acceptor as [27]

$$R_\mathrm{F} = \frac{9 \ln 10}{128 \pi^5} \kappa^2 \frac{\phi_0}{N_\mathrm{a} n^4} \int_0^\infty F_\mathrm{D}(\lambda) \epsilon_\mathrm{A}(\lambda) \lambda^4 \mathrm{d}\lambda \tag{2.7}$$

with κ: orientation factor, ϕ_0: fluorescence quantum yield of the donor in the absence of FRET, N_a: Avogadro constant, and n: refractive index of the surrounding medium. As in the case of FRET, the transfer rate constants may depend strongly on the distances between individual donors and acceptors and on the number of acceptors close enough to a donor. Thus, for ensembles with an undefined distance distribution, the prediction of the resulting decay kinetics in a sample can become rather complex if not practically impossible. An intrinsically mono-exponential decay, cf. Eq. (2.2) could stay mono-exponential if the FRET rate constant was the same for every donor and therewith indeed a constant. Since this is usually not given, FRET is likely to not only alter the effective lifetime, but also the class of function that describes the donor luminescence decay. Nevertheless, the luminescence decay of the ensemble of donors is definitely faster in the presence of acceptors since the additional decay channel always increases the decay rate irrespective of its precise value. The luminescence decay of the acceptors might appear to be slowed down as it is coupled to the donor decay. Moreover, the spectral intensities of donors and acceptors may deviate from the situation without the energy transfer.

In systems that allow for numerous subsequent transfer steps, the excitation energy may travel around the system as it is passed between molecules, hence the term ‘energy migration’. This requires a sufficiently high density of luminophores ensuring short distances between donors and possible acceptors. A gradient in the concentration of luminophores might lead to a directed transport of excitation energy into the direction of higher concentration. As long as the energy migration is due to a homotransfer, there is no impact on the decay kinetics [27] as the number of excited molecules does not change [63], cf. Eq. (2.2). However, spectroscopically different acceptors or even traps with lower-lying energy levels can act as energy sinks and draw excitation energy from the ensemble which then represents another decay channel and has an impact on the decay kinetics.

3. Experimental methods

This chapter is an overview of the experimental techniques used for the presented studies. It covers the basics of absorption and photoluminescence spectroscopy, confocal laser scanning microscopy and flow cytometry with time resolution as well as a brief outline of the bead synthesis.

3.1. Absorption spectroscopy

Measurements of the absorption of electromagnetic radiation in the visible light spectrum often provide first insights into the landscape of electronic and vibrational transitions of a system under investigation. A standard setup for absorbance measurements is displayed in Fig. 3.1. From a broadband light source spectrum (typically a xenon or deuterium lamp), a certain narrow wavelength range is chosen with a dispersion element (typically a grating monochromator). The beam

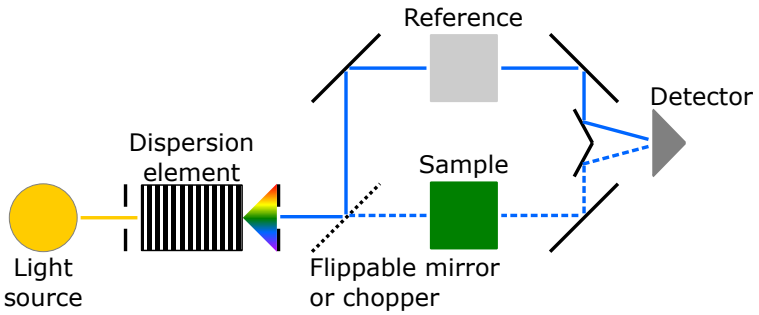

Figure 3.1: Schematic drawing of a dual-beam absorption spectrometer. A narrow wavelength range is cut from the spectrum of the broad band light source and sent to the sample and reference positions. The beam path is periodically changed with a flippable mirror or a chopper to alternate the channel for which the transmittance is measured. The absorbance is calculated from the intensity values in both channels. Wavelength-dependent information is obtained by scanning across the desired spectral region.

is sent alternately to the sample or the reference position and the intensity is measured with the same detector. Alternatively, a beam splitter and two detectors can be used. A blank sample that does not contain the species of interest but resembles the transmittance properties of the matrix (solvent) and the cuvette is required. The blank spectrum may either be measured once with the blank in the sample position or simultaneously with every sample spectrum with the blank placed in the reference position.

An absorption spectrum is actually based on a measurement of the intensity of the transmitted light which, neglecting reflection and scattering, is given by the Lambert-Beer law [55]

$$I(l) = I_0 \cdot 10^{-\epsilon c l} \,. \tag{3.1}$$

Here, $I(l)$ is the remaining light intensity of an initial intensity I_0 after traveling a distance l in the sample with chromophore concentration c and molar absorption coefficient ϵ. The molar absorption coefficient depends on the wavelength of the light, i.e., $\epsilon = \epsilon(\lambda)$. Depending on which quantity is known, either the sample concentration or the molar absorption coefficient may be calculated from the measured absorbance

$$A = -\log_{10} \frac{I}{I_0} = \epsilon c l \,. \tag{3.2}$$

Deviations from Eqs. (3.1) and (3.2) might occur, e.g., for very high light intensity (saturation effect) or scattering samples [1, 55]. Absorbance spectra only provide information about transitions from the ground state to the excited states. Excited state dynamics remain unknown.

The spectrometer used for the presented studies was an *Analytik Jena Specord 210 Plus* and measurements were carried out on solutions at room temperature in standard quartz glass cuvettes with 1 cm path length. The spectral band width and step size were set to 1 nm which mainly determines the spectral resolution.

3.2. Photoluminescence spectroscopy

Photoluminescence measurements probe the spectral characteristics and dynamics of the excited states. The sample is excited with light from the ultraviolet, visible, or infrared spectral range. The excitation may be continuous or pulsed, depending on the purpose of the measurement. Emission of photons from the sample is accordingly measured in a time-integrating manner (steady state) or with time resolution on the time scale of the photoluminescence decay under investigation. A schematic drawing of a photoluminescence spectrometer is given in Fig. 3.2. The excitation light source used here was either a standard xenon lamp (steady state) or a pulsed supercontinuum laser (time-resolved). The excitation monochromator cuts a defined part out of the spectrum of the light source and passes it on to the sample chamber. A polarizer can be used to set the polarization of the light incident on the sample. Part of the excitation light is reflected to a reference detector by a beam splitter to monitor the light source intensity to correct for fluctuations. The light emitted from the sample is collected at an angle of 90° with respect to the excitation channel. This geometry avoids that transmitted excitation light enters the emission light path. Again, a polarizer can be used to only detect emitted light with a certain polarization. A monochromator is used to only allow a defined spectral fraction of the emitted light to reach the detector. For detection, photomultiplier tubes (PMTs) or multichannel-plate photomultiplier tubes (MCP-PMTs) are used.

The photoluminescence spectrometers used to acquire the data to be discussed were *Edinburgh Instruments FSP920* and *FLS920* spectrometers. Measurements were performed in standard 1 cm × 1 cm quartz glass cuvettes at room temperature (≈ 293 K) and particulate samples were stirred to avoid sedimentation.

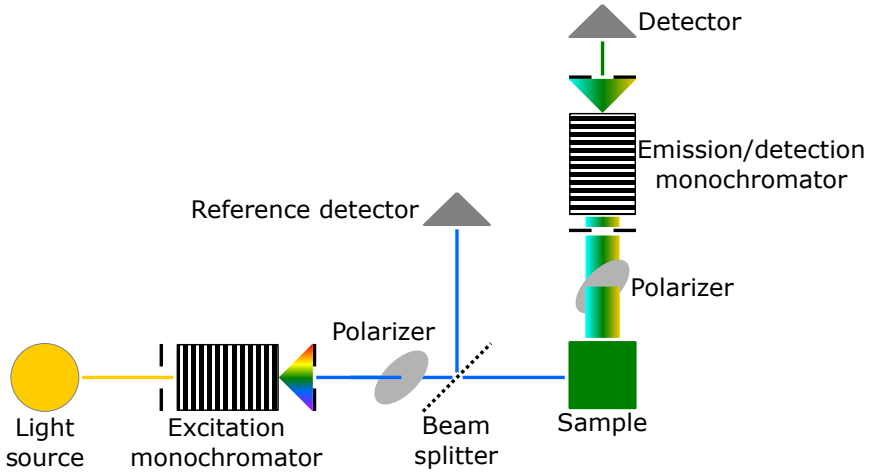

Figure 3.2: Schematic drawing of a photoluminescence spectrometer. The light source may be a standard xenon lamp or a continuous wave or pulsed laser. The bandpass is chosen with the excitation monochromator. Polarizers in the excitation and emission light path allow for photoluminescence anisotropy measurements. The reference detector is used to correct the emission signal intensity for fluctuations in the excitation intensity. An emission monochromator sets the emission bandpass.

3.2.1. Steady-state photoluminescence spectroscopy

In steady-state spectroscopy, the sample is illuminated with a continuous flux of light and the emission intensity is measured time-integrated. Common modes of operation are the acquisitions of photoluminescence excitation and emission spectra. In both cases, a wavelength-dependent intensity curve is obtained.

For excitation spectra, the excitation wavelength is scanned and the emission intensity is measured at a fixed detection wavelength. Such a spectrum is similar to an absorption spectrum though it does not provide information about non-fluorescent chromophores that only absorb light since transitions with solely non-radiative de-excitation pathways do not emit photons that could be detected. The intensity in an excitation spectrum is determined by the amount of absorbed light and the luminescence quantum yield for the chosen excitation and emission wavelengths.
For emission spectra, the excitation wavelength is fixed and the detection wavelength is scanned to obtain emission intensities at different wavelengths.

The excitation light source used was a standard xenon lamp and detection was carried out with a *Hamamatsu R2658P* PMT.

3.2.2. Time-resolved photoluminescence spectroscopy

Studies of excited state dynamics require a sufficient temporal resolution on the time scale relevant to the studied processes. For the case of fluorescence, this time scale is usually on the order of nanoseconds [54]. A standard technique for measuring photoluminescence intensity decays is time-correlated single photon counting (TCSPC) [64]. The sample is excited by an excitation light

source that provides δ-like pulses with respect to the required time resolution. Subsequently, single photons emitted from the sample are detected with a suitable detector, e.g. an MCP-PMT. The time delay between the arrival of the excitation pulse at the sample and the first emitted and detected photon from the sample is measured. This is repeated for numerous cycles resulting in a histogram of arrival times that forms the photoluminescence intensity decay curve. The temporal resolution of the overall system depends on the excitation pulse length and the response of the detection system. Moreover, optical components introduce additional wavelength-dependent effects. A good estimate of the time resolution can be found by measuring an instrument response function (IRF) with a scattering, non-luminescent sample under equal excitation and emission wavelengths. The IRF contains the temporal characteristics of the overall system including light source, detector, and electronics.

In the simplest case, the photoluminescence decay is mono-exponential, cf. Eq. (2.3), and the slope of the intensity decay curve on a semi-logarithmic plot is directly related to the excited state lifetime. In more complex systems, however, the decay is often multi-exponential or non-exponential with multiple lifetimes from, e.g., different species or molecules situated in different microenvironments. A decay model can be fitted to the acquired data. However, since the measured decay curve represents a convolution of the true decay (δ-pulse response of the sample) with the IRF, the model function cannot be fitted directly to the data. Instead, the decay model I_M has to be convolved with the IRF and the result of the convolution must be fitted to the data [64]:

$$I(t) = \int_0^t I_\mathrm{M}(t-t')IRF(t')\,\mathrm{d}t' \,.$$

The fit parameters, especially the lifetimes, may give insight into photophysical processes or only provide qualitative information. This depends on the used model and the specific conditions. In the case that the effect of the instrument characteristics is negligible, i.e. when the luminescence lifetime of a sample is much longer than the temporal width of the IRF and there are no further distortions, the mean (intensity-averaged) luminescence lifetime can be calculated from [27]

$$\tau_\mathrm{mean} = \frac{\int_0^\infty tI(t)\mathrm{d}t}{\int_0^\infty I(t)\mathrm{d}t} \approx \frac{\sum_{j=1}^{j_\mathrm{max}} t_j I_j}{\sum_{j=1}^{j_\mathrm{max}} I_j} \,. \tag{3.3}$$

Here, j denotes the bins of a measured decay curve with the respective number of counts I_j and time t_j of a certain bin.

The acquisition of multiple photoluminescence decay curves at different excitation or emission wavelengths allows the combination of spectral and temporal information. It is possible to reconstruct spectra at different time points during the decay, so called time resolved emission (or excitation) spectra, TRES [64]. To this end, a model decay function is fitted to each decay curve. Commonly, some multi-exponential decay function

$$I_{\mathrm{M}(\lambda)}(t) = \sum_j A_j(\lambda)\mathrm{e}^{-\frac{t}{\tau_j(\lambda)}} + B$$

with wavelength-dependent amplitudes A_j, background parameter B, and lifetimes τ_j is employed.

Thus, a noise-free representation of the fluorescence decay at each wavelength combination under investigation is obtained. The time-resolved spectrum at time t can then be obtained from the set of these decays as [65]

$$I(t,\lambda) = I_{\mathrm{s}}(\lambda)\frac{\sum_j A_j(\lambda)\mathrm{e}^{-\frac{t}{\tau_j(\lambda)}}}{\sum_j A_j(\lambda)\tau_j(\lambda)}$$

where $I_s(\lambda)$ is the steady-state (i.e. time-integrated) intensity spectrum of the sample. It is often worthwhile to area-normalize these spectra (time-resolved area-normalized emission spectra, TRANES) [65]. Such spectra provide information beyond time-integrated spectra and can be used to investigate the decay dynamics of different species in one sample.

The excitation light source for pulsed excitation was an *NKT Photonics SC400-2-PP* supercontinuum laser and time-resolved detection was carried out with a *Hamamatsu R3809U-50* MCP-PMT.

3.2.3. Photoluminescence anisotropy measurements

The probability for absorption of a photon by a molecule is highest when its transition dipole moment of absorption and the electric field vector of the incident radiation are parallel [27]. During the excited state lifetime, the molecule might rotate or change its orientation otherwise and therewith the transition dipole moment for emission rotates. Also, an intrinsic deviation between absorption and emission transition dipole moment orientation may exist. This means that the polarization of the incident and emitted radiation can differ. This difference can be measured using polarizers in the excitation and emission light paths (cf. Fig. 3.2) and it is given by the anisotropy r [66]

$$r = \frac{I_{\parallel} - I_{\perp}}{I_{\parallel} + 2I_{\perp}} = \frac{I_{\mathrm{VV}} - GI_{\mathrm{VH}}}{I_{\mathrm{VV}} + 2GI_{\mathrm{VH}}}\,, \qquad G = \frac{I_{\mathrm{HV}}}{I_{\mathrm{HH}}}\,,$$

where $I_{\parallel}$ is the photoluminescence intensity measured with both polarizers parallel and $I_{\perp}$ is the intensity for crossed polarizers. For the typical L-geometry as depicted in Fig. 3.3, the corresponding polarizer orientations in excitation and emission for correct measurements are vertical-vertical (VV), vertical-horizontal (VH), horizontal-vertical (HV), and horizontal-horizontal (HH). The G factor needed to correct for polarization-dependent sensitivity and transmittance of the optical components has to be measured with horizontally polarized excitation light as this guarantees sample-independent emission intensity for all polarizer orientations in the emission channel.

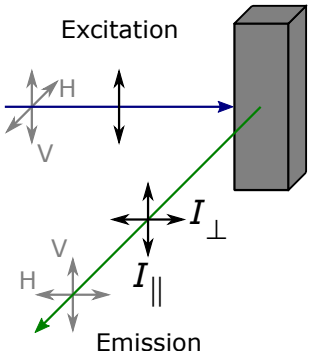

Figure 3.3: Arrangement for anisotropy measurements.

High photoluminescence anisotropy is expected for molecules with low rotational freedom, e.g. in viscous or even rigid matrices. If there is no structural anisotropy, such as preferred molecular orientation, in the sample itself, the maximum (fundamental) anisotropy is $r = 0.4$ [27]. Apart from molecular rotation during the excited state lifetime, the anisotropy can be decreased by reabsorption of radiation, energy transfer processes, or scattering. Especially energy migration causes a depolarization of the emission due to multiple steps among molecules with different orientation [27].

3.2.4. Inner filter effects

In samples with a high density of luminophores, so called inner filter effects occur [27].
The excitation inner filter effect occurs when the incident light is mostly absorbed close to the cuvette wall facing the light source and in turn almost no light reaches the cuvette center. Consequently, the cuvette center which is in focus of the detection system is subject to diminished excitation density whereas the luminophores located away from the cuvette center absorb most of the incident light but cannot contribute to the signal intensity at the detector. Thus, the measured intensity might be comparatively high for excitation wavelengths where light is actually barely absorbed by the sample as this light is able to reach the focal volume and contribute to the signal. In extreme cases, this might lead to an inversion-like distortion of excitation spectra with high intensities at wavelengths of low sample absorbance and lower intensity at wavelengths of high sample absorbance.
The emission inner filter effect is caused by reabsorption of photons formerly emitted by the sample itself. This, understandably, affects the blue edge of the emission spectrum as it often partially overlaps with the red edge of the absorption spectrum. Consequently, the measured emission spectrum lacks intensity on the blue edge which causes distorted or apparently shifted spectra. Luminophores with a small Stokes shift are especially prone to such distortions.

The emission inner filter effect may also have an impact on the measured photoluminescence decay kinetics and the photoluminescence anisotropy. Due to reabsorption of emitted photons, the measured photoluminescence decay curve will be distorted and the apparent lifetime will be longer than the actual lifetime [56, 67]. In addition, a too high sample concentration can artificially decrease the obtained luminescence anisotropy [27].

3.3. Confocal laser scanning microscopy

As the term suggests, in confocal laser scanning microscopy (CLSM) a laser spot is scanned across the sample or a defined region of the sample. Thereby, a pixelwise image of photoluminescence intensity, transmittance or even luminescence decay curves or spectra of the sample can be acquired. A schematic drawing of a CLSM setup is shown in Fig. 3.4. Multiple laser light sources providing different excitation wavelengths are coupled into the system via fiber optics. The beam is scanned across the chosen range by means of a moving mirror assembly and then focused onto the sample with the objective. Transmitted light can be detected giving rise to a transmission image. Light emitted by the sample is collected with the same objective as used for excitation and directed to a set of detectors with a beam splitter or dichroic mirror. Each channel may be used for different spectral ranges determined by filters and grating monochromators, thus different spectral channels can be visualized. When pulsed lasers are used, also time-resolved (TCSPC, cf. Sec. 3.2.2) measurements can be carried out. The technique of generating an image with false-colors assigned to fluorescence (luminescence) lifetimes in each pixel is called fluorescence lifetime imaging microscopy (FLIM). Both spectrally and time-resolved microscopy combine spatial resolution with optical-spectroscopic investigation of a specimen.

The setup used was an *Olympus FV1000* extended with a *PicoQuant FLIM upgrade kit.*

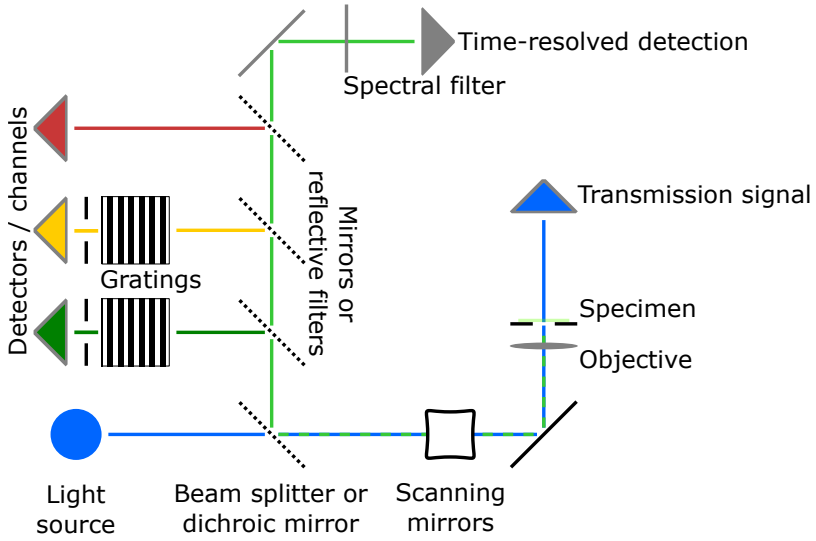

Figure 3.4: Schematic drawing of a confocal laser scanning microscope with four detectors and capabilities for spectrally resolved measurements. The light source represents different continuous wave or pulsed lasers that are coupled into the system via optical fibers. The excitation beam can be scanned across the sample. This provides spatially resolved photoluminescence and transmission information. Also, pixelwise measurements of luminescence decay curves is possible.

3.4. Flow cytometry

Flow cytometry (FCM) is employed to analyze single objects (e.g. cells, particles, luminescent beads, biomolecular assemblies) dispersed in a liquid sample. The sample is sent through a flow cell as displayed in Fig. 3.5 for an example of a basic flow cytometry setup. Single objects in the sample are hydrodynamically focused in the flow cell by a surrounding stream of sheath fluid. The flow cell is illuminated by one or several lasers of different wavelengths. Objects passing the laser spot give rise to light scattering which is measured as a forward scatter (FSC) or side scatter (SSC) signal. Objects exhibiting autofluorescence or attached luminophores will emit light that can be detected in various fluorescence (FL) channels with appropriate optical filters. Thus, spectroscopic characteristics can be measured on a single-particle level for a large number of objects.

Conventional FCM only generates intensity signals for every available channel. More information, however, can be deduced with time-resolved detection that tracks the excited state dynamics of each object passing the flow cell. Generally, time-resolved methods are divided into frequency domain and time domain techniques [18]. For our setup, we used a time-domain photon counting technique. A prototype lifetime flow cytometry (LT-FCM) device, *Quantum Analysis pantau*, was provided by `Quantum Analysis GmbH` for assessment and development [53]. The schematic drawing in Fig. 3.5 shows the optical setup. The excitation laser emitting at 488 nm is modulated with a square wave of 5 MHz frequency that switches between 100 and < 0.1 mW output power. Next to the common side scatter (SSC) and fluorescence (FL) channels, a detector for time-resolved

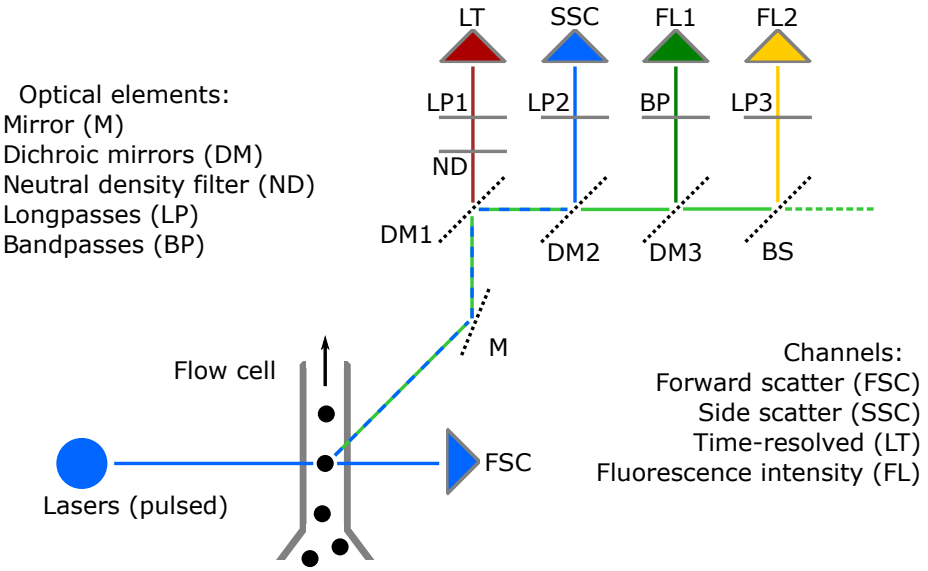

Figure 3.5: Schematic drawing of a flow cytometer with a pulsed laser as excitation light source and five detectors. Objects in the sample pass the flow cell and cause specific signals at the different detectors when crossing the laser beam. Accessible information includes scattered light intensity, photoluminescence characteristics and also luminescence decay dynamics on a single-particle level. A list of the optical components is given in Tab. 3.1.

signal readout (lifetime, LT) was installed. The FSC channel was not available in our setup and is only shown for the reason that it is a standard channel in FCM. All optical components with their specifications are listed in Tab. 3.1. Time-resolved detection is based on photon counting and provides photoluminescence intensity decay curves in the time domain. In contrast to conventional TCSPC, more than one single photon per pulse can be detected. The rate of impinging photons can therefore be much higher than in TCSPC and is mainly limited by the detector dead time.

Element	Optical characteristics
M	Mirror
DM1	Dichroic mirror (620 nm)
ND	Neutral density filter
LP1	Longpass (630 nm)
DM2	Dichroic mirror (500 nm)
LP2	Longpass (435 nm)
DM3	Dichroic mirror (538 nm)
BP	Bandpass ($[520 \pm 14]$ nm)
BS	Beam splitter (90:10)
LP3	Longpass (530 nm)

Table 3.1: List of optical elements in the LT-FCM.

The temporal resolution, that means the time bin width, of our detection system was 2.5 ns, the maximum delay for photon detection after the pulse was 60 ns. These characteristics determine the lower and upper limit of reasonably measurable luminescence decays.

Usually, a sample speed of 1 µl/s with a sample volume of several hundreds of microliters was used. The low sample speed was used because a main limitation in processing speed of the prototype instrument is the manageable data rate. Low sample speeds allow for larger separations between the objects in the stream and therefore result in a better counting efficiency. The actual flow speed of the mixture of sheath fluid and sample through the flow cell is determined by the pressure in the flow cell. The pressure applied to the sheath fluid stream was within the range of 30 to 180 hPa (typically 40 hPa). It determines the speed of the objects passing the flow cell and accordingly the measurement time window per object. This measurement time window amounts to 10 to 70 µs.

3.5. Bead synthesis

Dye-loaded polymer microbeads used in the presented studies were obtained from `PolyAn GmbH`. These beads are made of poly(methyl methacrylate) (PMMA) loaded with rhodamine 6G (Rh6G) during synthesis. The beads were synthesized in a dispersion polymerization process [52, 68] and the dye was directly added to the reaction mixture. According to the presumed mechanism of particle formation [68, 69], the formation and aggregation of PMMA nuclei and the growth of particles compete with the adsorption of stabilizer. Thus, the final beads are covered by a layer of adsorbed stabilizer. The stabilizers used for the studied beads are polyvinylpyrrolidone (PVP) and aerosol-OT (AOT, dioctyl sulfosuccinate). The chemical structures of Rh6G, PMMA, PVP, and AOT are shown in Fig. 3.6.

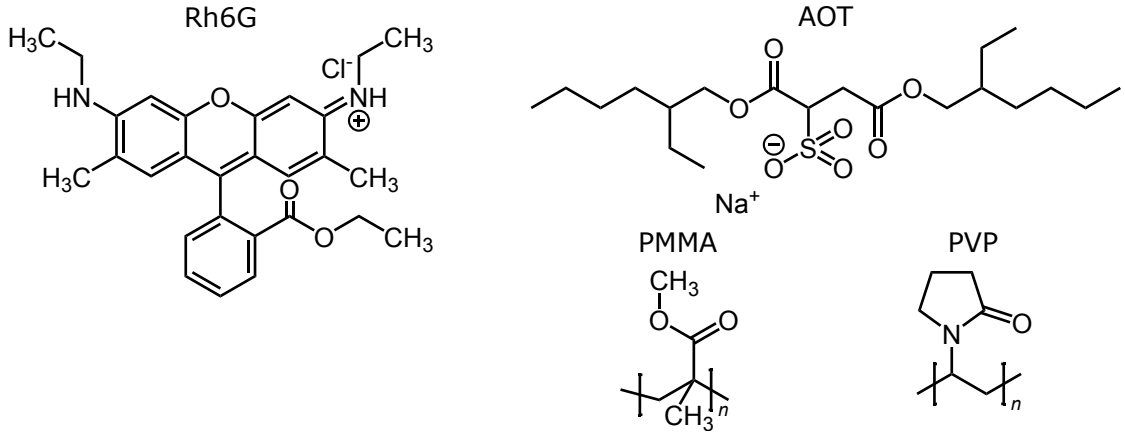

Figure 3.6: Chemical structures of the compounds involved in the bead synthesis.

The nominal dye loading concentration c_{nom} is the molar concentration in the reaction volume (i.e. joint volume of methanol and MMA) of dye applied during synthesis. The effective dye concentration c_{eff} denotes the actual concentration in the beads. This is illustrated in Fig. 3.7. Panel (a) shows the reaction mixture in the beginning of the bead synthesis with homogeneously distributed solved dye at a nominal dye concentration c_{nom}. The nominal dye loading concentration is comparable between all samples since the amount of MMA and the overall reaction volume were the same across all samples. In panel (b), beads have formed and taken up part of the dye from the reaction mixture. The molar dye concentration per bead volume is called the effective dye loading concentration c_{eff}. The ratio of these two quantities is the dye loading efficiency f.

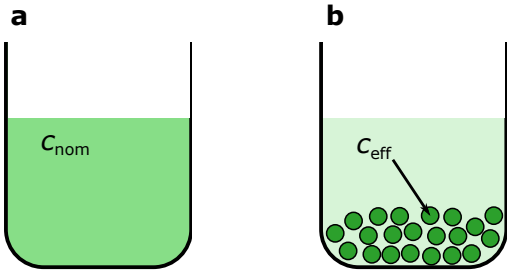

Figure 3.7: Illustration of the dye loading concentration. (a) The nominal dye (loading) concentration denotes the molar dye concentration in the reaction volume at the beginning of the synthesis. (b) The effective dye loading concentration is the molar dye concentration per bead (polymer) volume in the final beads.

4. Optical-spectroscopic characteristics of dye-loaded polymer microbeads

Dye-loaded polymer microbeads are an important tool in many fluorescence-based applications and techniques such as bead-based assays, fluorescence microscopy, and the calibration of flow cytometers and fluorescence imaging systems. Despite this fact, very few reports on the optical-spectroscopic properties of such beads exist and valuable pieces of information are missing. This includes information on spectral shape and position of absorption and emission bands, the fluorescence decay kinetics and the fluorescence quantum yield as well as the mechanisms that cause possible variations of these characteristics such as, e.g., concentration self-quenching or surface effects. An in-depth study of these properties for micrometer-sized beads made of poly(methyl methacrylate) (PMMA) loaded with rhodamine 6G (Rh6G) presented here is a first step to extend the knowledge in this field.

Spectroscopy on particulate samples is prone to measurement artifacts due to light scattering. Thus, an evaluation of possible effects on the results is given in Sec. A.1. All following studies are carried out with appropriately low bead concentrations according to Fig. A.3 to ensure reliable measurement results.

The sample synthesis was carried out by `PolyAn GmbH`. The beads were fabricated in a dispersion polymerization procedure [68] which was briefly explained in Sec. 3.5 and elsewhere [52]. A comprehensive set of bead samples exhibiting different mean diameters and dye loading concentration was studied. Beads are classified by diameter in small (< 3 µm), intermediate (3–8 µm), and large (> 8 µm) beads. At first sight, these beads seem to be characterized by their size and loading concentration. However, it was unclear whether they additionally differ in optical-spectroscopic properties other than the obvious difference in absolute fluorescence intensity per bead. Thus, a detailed study of the spectral properties and the excited state dynamics was performed.

We start with a determination of the actual, i.e. the effective, dye loading concentration in the beads. Then, spectral properties and fluorescence decay dynamics are be discussed. Further fluorescence characteristics including measurements of the fluorescence anisotropy and the fluorescence quantum yield are investigated. Finally, a model that explains the observed characteristics is presented and evaluated with numerical random walk simulations.

Parts of this chapter are based on Ref. [52]. A list of all investigated samples and their key properties is given in Tab. 4.1 at the end of the experimental section of this chapter.

4.1. The dye loading concentration

The nominal dye loading concentration, c_{nom} is the applied molar concentration of dye during synthesis. From the point of view of the synthesis, it is comparable among different bead samples since the applied mass of MMA was the same for all samples. However, the effective dye loading concentration c_{eff}, i.e. the actual concentration of dye molecules in the polymer beads, might differ from the nominal loading concentration as depicted in Fig. 3.7. For dyes with known molar absorption coefficient, the dye concentration in a solution can be determined via absorbance measurements, cf. Eq. (3.2). In particulate samples, however, light scattering makes a precise determination of the absorbance impossible without sophisticated setups. Therefore, dried bead samples with precisely defined bead mass were dissolved in acetone and subsequently the dye concentration in the resulting solution was determined from the measured absorbance. The effective dye loading concentration c_{eff} as dye moles per polymer volume V_{beads} can be calculated from

$$c_{\mathrm{eff}} = \frac{c_{\mathrm{dye}}\, V_{\mathrm{sol}}}{V_{\mathrm{beads}}} = \frac{c_{\mathrm{dye}}\, V_{\mathrm{sol}}\, \rho_{\mathrm{PMMA}}}{m_{\mathrm{beads}}}\,,$$

where c_{dye} is the molar dye concentration obtained upon dissolving a mass m_{beads} of beads with mass density ρ_{PMMA} in a volume V_{sol} of acetone. Using the Lambert-Beer law, see Eq. (3.2), and the mass concentration of dissolved beads $c_{\mathrm{beads}} = \frac{m_{\mathrm{beads}}}{V_{\mathrm{sol}}}$ one finds

$$c_{\mathrm{eff}} = \frac{A\, \rho_{\mathrm{PMMA}}}{\epsilon\, c_{\mathrm{beads}}\, l}\,. \tag{4.1}$$

The maximum of the molar extinction coefficient of Rh6G in acetone is $\epsilon = 97(1)\cdot 10^3$ l/mol cm. To have a common measure independent of the nominal dye loading concentration c_{nom} for all samples, a dye loading efficiency needs to be defined. The point of 0 % efficiency clearly corresponds to the case where no dye is incorporated into the beads. The definition of 100 % efficiency, however, could follow different approaches. It could be, e.g., defined as all dye available during synthesis being incorporated in the beads or as the final dye concentration in the beads being the same as the dye concentration in the reaction volume. Moreover, it might be necessary to further consider how much of the available MMA was actually converted to PMMA beads. Such a level of detail is not required for the following discussions. Thus, the loading efficiency is simply defined as the ratio of the effective molar dye loading concentration per polymer volume and the nominal molar dye concentration in the reaction volume:

$$f = \frac{c_{\mathrm{eff}}}{c_{\mathrm{nom}}}\,.$$

It will be given in arbitrary units.

As mentioned before, the effective dye loading concentration of the beads, and therewith the loading efficiency, was determined from absorption measurements on solutions of dissolved beads. The dye loading efficiency depends on the mean bead diameter as depicted in Fig. 4.1(a). A distinct tendency towards increased loading efficiency with decreasing mean bead diameter was observed. Furthermore, there is also a correlation between the dye loading efficiency and the amount of

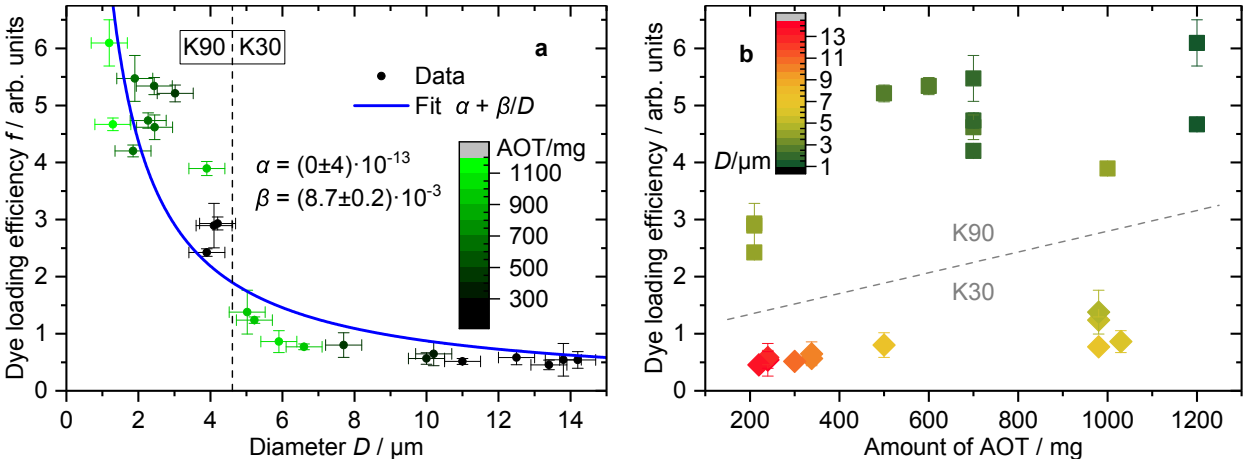

Figure 4.1: Dependencies of the dye loading efficiency on (a) the mean bead diameter and (b) the amount of AOT used during synthesis per 185 ml reaction volume. The symbols are color-encoded: (a) from black to green for small to large amounts of AOT, (b) from green to red for small to large bead diameters. The terms K30/90 denote the chain length of PVP. There is a clear tendency towards higher loading efficiency at decreased bead diameter in (a). The blue curve depicts a fit of Eq. (4.2) to the data. The dependence of the loading efficiency on the amount of AOT in (b) is interdependent with the chain length of PVP.

co-stabilizer AOT used as depicted in Fig. 4.1(b). Increasing the amount of AOT increases the dye loading efficiency. However, there is a mismatch between samples synthesized using PVP of different chain lengths: PVP-K30 or PVP-K90. Upon changing to K90, lower amounts of AOT can lead to even higher dye loading efficiency than obtained with more AOT using K30. The two different variants of PVP are used to achieve different bead diameter ranges as indicated by the vertical line in Fig. 4.1(a). The mean bead diameter is mainly determined by the amount of PVP and AOT [52, 68], see also Sec. 3.5. Consequently, the observed dependence on the bead diameter, Fig. 4.1(a) might only be an apparent one which is actually correlated with the synthesis conditions, Fig. 4.1(b). Especially the co-stabilizer AOT is assumed to play an important role as it is anionic and may therefore interact with the cationic Rh6G. This is the most likely reason for the dependence of the dye loading efficiency on the amount of AOT used. Nevertheless, the loading efficiency also depends on the chain length of the PVP used. This ambiguity suggests that not only the amount of AOT governs the incorporation efficiency of the dye into the forming polymer beads.

During the synthesis, aggregation of PMMA nuclei occurs concurrently with the adsorption of stabilizer (PVP) and co-stabilizers (AOT) [68, 69]. The final beads will have a shell of adsorbed stabilizers which can only be removed by extensive washing of the beads [68]. Combining this with the assumption of preferential binding of Rh6G to AOT, there should be distinct differences between the incorporation mechanism and the microenvironment of dye in the bead core and at the surface. Dye molecules in the core are randomly incorporated and sterically kept in place.

Therefore, the dye molecules in the core are assumed to be homogeneously distributed. Close to the bead surface, however, there is a specific accumulation of AOT-bound Rh6G molecules which form a shell with high dye loading concentration. Such a behavior is in agreement with both findings of Figs. 4.1(b) and (a): on the one hand, the loading efficiency depends on the amount of AOT because it binds Rh6G. On the other hand, it also depends on the bead diameter since AOT is located at the surface and the mean diameter determines the surface-to-volume ratio. As a result, it stands to reason to assume two contributions to the overall loading efficiency: one describing the bulk (core) loading efficiency and one that describes the surface-related incorporation. In the simplest case (without surface effects), the effective dye loading concentration c_{eff} is proportional to the nominal dye loading concentration c_{nom}:

$$c_{\mathrm{eff}} = \alpha^* \, c_{\mathrm{nom}} \, .$$

The proportionality constant α^* is dimensionless. Thus, the amount of dye in a bead of volume V_{bead} is given by

$$c_{\mathrm{eff}} \, V_{\mathrm{bead}} = \alpha^* \, c_{\mathrm{nom}} \, V_{\mathrm{bead}} \, .$$

In case of surface-specific incorporation, an additional term must be included that is governed by the bead surface area A_{bead} and represents a surface density of molecules. Thus, the adapted equation reads

$$c_{\mathrm{eff}} \, V_{\mathrm{bead}} = \alpha \, c_{\mathrm{nom}} \, V_{\mathrm{bead}} + \beta^* \, c_{\mathrm{nom}} \, A_{\mathrm{bead}} \, ,$$

where α is the coefficient for bulk incorporation when also surface-related incorporation is present and β^* is the proportionality constant for surface-specific incorporation. We obtain an expression for the effective dye loading concentration upon division by the bead volume of a bead with diameter D. One finds

$$\begin{aligned} c_{\mathrm{eff}} &= \alpha \, c_{\mathrm{nom}} + \beta^* \, \frac{A_{\mathrm{bead}}}{V_{\mathrm{bead}}} \, c_{\mathrm{nom}} \\ &= \alpha \, c_{\mathrm{nom}} + \beta^* \, \frac{\pi \, D^2}{\frac{1}{6} \pi \, D^3} \, c_{\mathrm{nom}} \\ &= \alpha \, c_{\mathrm{nom}} + \beta \, \frac{1}{D} \, c_{\mathrm{nom}} \end{aligned}$$

and the loading efficiency is given by

$$f = \frac{c_{\mathrm{eff}}}{c_{\mathrm{nom}}} = \alpha + \beta \, \frac{1}{D} \, . \tag{4.2}$$

A fit of Eq. (4.2) to the data obtained from absorbance measurements on the dissolved beads is shown in Fig. 4.1(a). The agreement between fit and data is acceptable and supports the overall concept. However, for small beads there are large discrepancies between the data points and the fit function which questions the suitability of the proposed model. A possible issue could be the complex interplay of the involved parameters such as the PVP chain length, the amount of AOT, the surface-to-volume ratio and the amount of dye. Also, the exclusive adsorption of PVP and AOT at the bead surface is not certain. In addition, it is possible that the parameter α for core

incorporation is not truly a constant. It might rather depend on, e.g., the balance of AOT and Rh6G since the amount of 'free' dye that is not bound to AOT determines how much dye is left to be incorporated into the core of a bead. Furthermore, the ratio of available surface and AOT influences how effective the incorporation close to the surface would be. Thus, the constants might in fact not be constant but dependent on the precise synthesis conditions. The results of the fit are to be interpreted with care due to the mentioned variation in the data points and deficiencies of the model.
Despite that, it seems to be clear that the relevance of the near-surface incorporation is superior to the core incorporation. This is supported by the fact that the dye loading efficiency in large beads is significantly lower than in small beads, cf. Fig. 4.1. The respective parameter α is basically zero and even for the largest beads investigated the surface term βD^{-1} dominates. Therefore, at least in small beads, the dye concentration near the surface is assumed to be much higher than in the core.

Moreover, preliminary results from dissolving beads synthesized without AOT compared to beads with AOT are shown in Fig. 4.2. It displays absorbance spectra of beads of similar size but different nominal dye loading concentration. For convenience, the spectra have been divided by

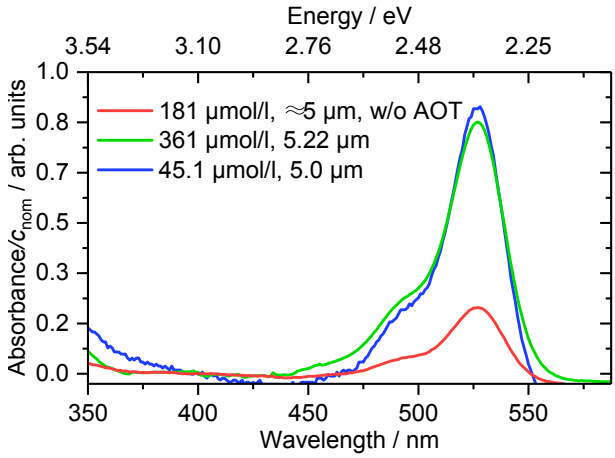

Figure 4.2: Absorbance spectra of beads synthesized with and without AOT. The spectra have been scaled by the applied nominal dye loading concentration and therefore reflect the dye incorporation efficiency. Indeed, these preliminary results show the striking impact of AOT on the dye incorporation. Spectra have been corrected for baseline distortion due to normalization.

the nominal dye loading concentration. Consequently, the displayed values are a measure of the dye incorporation efficiency. Obviously, the two samples synthesized using AOT show similar incorporation efficiency. The sample synthesized without AOT, however, exhibits a much lower incorporation efficiency. This emphasizes the importance of AOT for the dye loading process and supports the hypothesis of complexation of AOT and Rh6G.

Altogether, the determination of the effective dye loading concentration showed that small beads tend to exhibit a significantly higher dye incorporation efficiency than larger ones. Generally, it

is reasonable to assume that small beads are not only more strongly affected by the near-surface accumulation of dye due to their larger surface-to-volume ratio. Also, the higher concentration of AOT used in the synthesis of small beads reduces the amount of 'free' Rh6G not bound to AOT that is available for steric incorporation into the bead core. This gives rise to a further increased difference in local dye concentration between near-surface and core regions in small beads whereas large beads might exhibit rather homogeneous dye distributions.

A value for the mean dye-dye distance in the beads can be deduced from the relation between the effective dye loading concentration c_{eff} and the measured absorbance A defined in Eq. (4.1). The number of dye molecules per PMMA volume is the reciprocal of the volume per dye molecule which is given by

$$V_{\mathrm{mol}}^{-1} = c_{\mathrm{eff}}\, N_{\mathrm{A}}\,.$$

Here, N_{A} is the Avogadro constant and ρ_{PMMA} is the mass density of PMMA. It is assumed that each dye molecule occupies a spherical volume and the mean dye-dye distance is the diameter of the spherical volume per molecule:

$$d_{\mathrm{dd}} = \sqrt[3]{\frac{6\,V_{\mathrm{mol}}}{\pi}}\,. \tag{4.3}$$

Using Eq. (4.1), the dye-dye distance can be rewritten as

$$d_{\mathrm{dd}} = \sqrt[3]{\frac{6 \cdot m_{\mathrm{beads}}(\mathrm{mg}) \cdot \epsilon(\mathrm{l/mol\,cm}) \cdot l(\mathrm{cm})}{\pi \cdot \rho_{\mathrm{PMMA}}(\mathrm{mg/nm^3}) \cdot A \cdot V_{\mathrm{sol}}(\mathrm{l}) \cdot N_{\mathrm{A}}(\mathrm{mol^{-1}})}} \tag{4.4}$$

where m_{beads} is the mass of the beads dissolved in a volume V_{sol} of acetone, ϵ is the maximum of the molar extinction coefficient of Rh6G in acetone, l is the path length (i.e. the dimension of the cuvette), and A is the maximum of the absorbance measured in dissolved beads. The mean dye-dye distances range from 8.81(7) nm in the smallest beads with the high nominal dye loading concentration to 33(6) nm in large beads with low nominal dye loading concentration. Especially in small beads and close to the bead surface, the local distances between dye molecules may be significantly shorter than the average.

For the sake of simplicity and to keep the relation to the synthesis more clear, the following discussions will refer to the nominal dye loading concentration.

4.2. Optical spectroscopy

The optical-spectroscopic properties of luminophores may change when they face different microenvironments [1, 27, 56]. In the case of dye-loaded polymer beads, bead size, proximity of dye molecules to interfaces, and the dye loading concentration discussed in the preceding section may affect these properties. A set of Rh6G-loaded beads was subject to an in-depth optical-spectroscopic characterization [52].

4.2.1. Steady-state fluorescence spectroscopy

Fluorescence excitation and emission spectra of Rh6G-stained beads with different diameters and comparable nominal dye loading concentrations are shown in Fig. 4.3(a) and (b). Spectra of a dye solution in water serve as references. The excitation spectra, Fig. 4.3(a), of all bead samples are slightly redshifted with respect to the spectrum of the dye in water. Moreover, smaller beads display spectral broadening with respect to larger beads. The emission spectra, Fig. 4.3(b), of large and intermediately sized beads perfectly match those of the dye in aqueous solution. In contrast, small beads exhibit redshifted and broadened emission spectra. Unlike the broadening and shift in the excitation spectra, there is a clear distinction between the small beads exhibiting a shift and the larger beads exhibiting no shift.

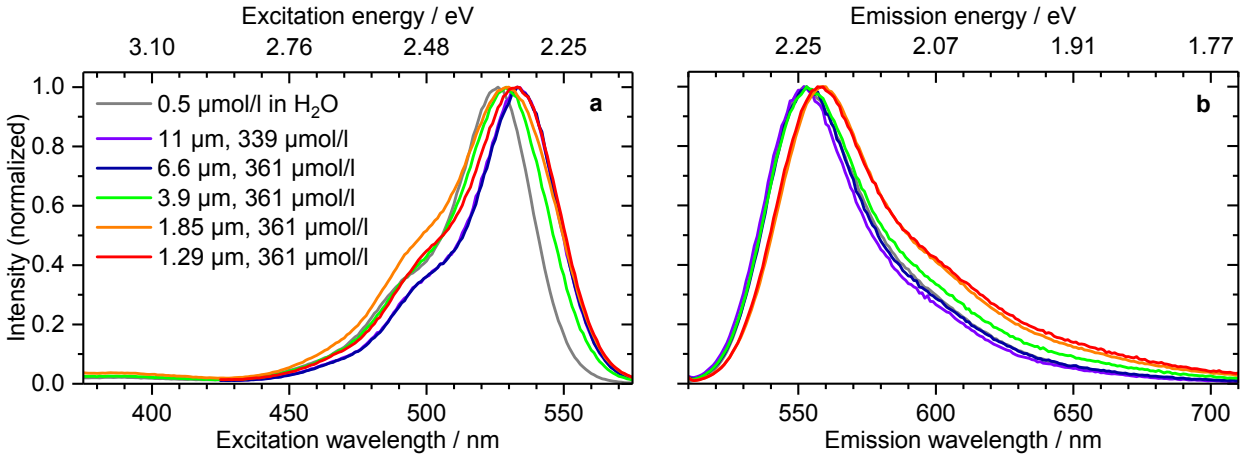

Figure 4.3: Fluorescence spectra of PMMA-beads of different mean diameters loaded with similar nominal concentrations of Rh6G. Spectra of Rh6G in water are displayed for comparison. (a) Excitation spectra, $\lambda_{fl,em}$=600 nm. (b) Emission spectra, $\lambda_{fl,ex}$=500 nm. The bead mass concentration was in the range of 0.05–1 mg/ml. Spectral shifts and broadening are observed for dye incorporated in beads and are more pronounced in beads with small diameters.
Previously published, adapted with permission from Ref. [52]. ©2018 American Chemical Society.

The redshift of the maxima of the excitation spectra from 526 nm in water to maximum 533 nm in PMMA beads is in agreement with absorbance measurements on PMMA films stained with Rh6G [70]. It could be explained by polar or ionic interactions between the cationic dye and the carbonyl or carboxyl groups of the surrounding PMMA. Additionally, the microenvironment, e.g. the dielectric properties, within the beads is different between the PMMA core and the PVP-AOT shell. The broadening of the excitation spectra can be attributed to the larger surface-to-volume ratio which leads to a larger influence of the dispersion medium (water). As water is able to penetrate and swell PMMA [71–73], an interaction of the near-surface molecules with water is likely. These molecules would contribute with a spectrum similar to that of Rh6G in water which is not redshifted. The superposition of the redshifted spectra from Rh6G surrounded by PMMA and those from Rh6G exposed to water leads to the observed broadening of the overall spectrum in smaller beads. In addition, the higher effective dye concentration in small beads could give rise

to near-surface aggregation and formation of (fluorescent) aggregates. Thus, there probably exist three species: dye monomers in the core, near-surface monomers, and near-surface aggregates. The absorption spectra of fluorescent Rh6G dimers are known to exhibit two peaks [70, 74] with a splitting of approximately 130 to 230 meV around the monomer peak depending on the solvent [74]. Such dimers, when fluorescent, could further contribute to the broadening of the excitation spectra of small beads where aggregation is supposed to be most severe.

Spectral shifts in fluorescence emission between Rh6G in water and PMMA films have been reported before as well [70]. The peak shift from 552 nm in water to maximum 559 nm in PMMA beads obtained here is slightly smaller than the value of 40 meV (from 553 to 563 nm) for PMMA films [70]. However, we observe a shift for small beads but not for intermediate and large ones even though larger beads face a weaker impact from surface effects and possible water penetration. Thus, the microenvironment that larger beads provide to the dye molecules is dominated by the polymer matrix and should be more similar to bulk or thin film than that of small beads. Consequently, a better agreement of spectral shifts in larger beads and thin films rather than small beads and thin film would have been expected. Similar to the excitation spectra, the shift and broadening could as well be caused by fluorescent near-surface aggregates [74]. Also, the different microenvironment provided by the stabilizer shell could lead to a spectral shift in emission. Alternatively, the shift could be caused by bead-internal reabsorption. Even though reabsorption effects due to the number density of beads in a sample could be excluded, bead-internal reabsorption is determined by the dye concentration within the bead itself. Another explanation could be based on an energy transfer process among the dye molecules. Excitation energy transfer such as Förster resonant energy transfer (FRET) could lead to an apparent redshift in the emission spectrum as the energy will preferably travel to the sites of lowest energy [75]. The mean dye-dye distances calculated by means of Eq. (4.4) can be as low as around 9 nm which is still relatively large for FRET to occur. However, due to the supposedly inhomogeneous dye distribution especially in small beads, dye-dye distances are probably significantly lower in near-surface regions. There, energy transfer is likely to happen. In this case, time-resolved data are helpful for clarification since they provide information on decay channels and variations in decay dynamics.

4.2.2. Time-resolved fluorescence spectroscopy

Depending on the specific circumstances, energy transfer or migration can have an impact on the fluorescence decay kinetics.

Figure 4.4(a) shows fluorescence decay curves of a subset of samples whose spectral properties were discussed above and presented in Fig. 4.3. For comparison, a fluorescence decay curve of Rh6G solved in water is shown as well. The first observation to note is the faster fluorescence decay in all particulate samples compared to the aqueous solution. It is known that, if several simplifying assumptions are made, the radiative rate turns out to be proportional to the squared refractive index of the surrounding medium of a fluorophore [56]. Even though there is no rigorous physical justification of this behavior [76], it is widely accepted and has been observed before for Rh6G [77]. Thus, the generally faster fluorescence decay in the particulate systems compared to the aqueous solution is attributed to the refractive index of PMMA (1.491 at 20 °C, 587.6 nm) [78] being higher than that of water (1.333 at 20 °C, 589 nm) [79].

Furthermore, differences in the decay curves between differently sized beads are observed. Whereas the large beads display mono-exponential decays, the intermediately sized and small beads exhibit multi-exponential decays as displayed in Fig. 4.4(a). In intermediately sized beads, additional slow decay components occur. In small beads, the slower decay components observed in intermediate beads are retained, but additional short decay components come into play. As apparent from Fig. 4.4(b), there is a complex interplay of both size and dye loading concentration. It turns out

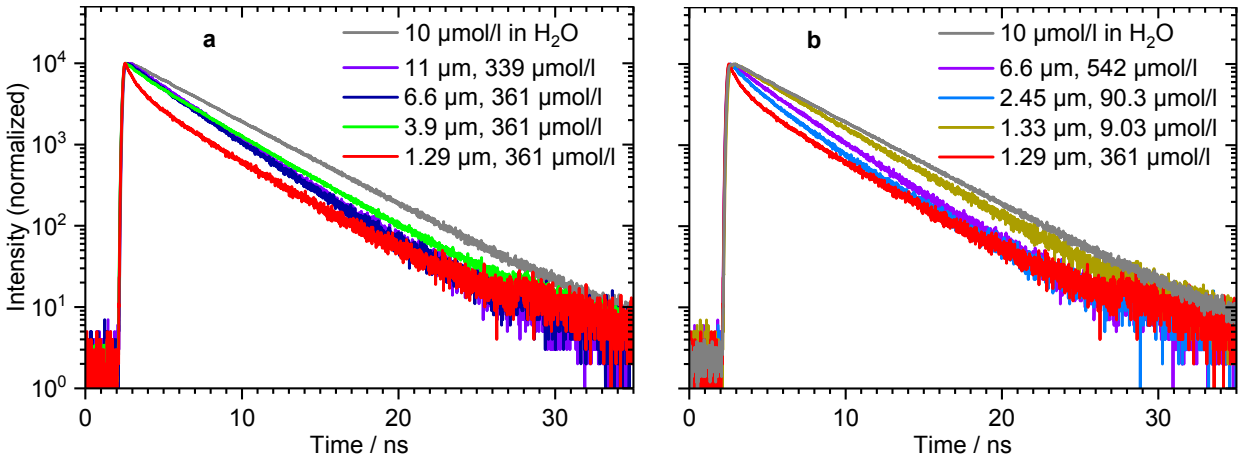

Figure 4.4: Fluorescence decay curves of (a) Rh6G-loaded beads with similar nominal dye loading concentration and different diameters. The fluorescence decay of Rh6G in aqueous solution is shown for comparison. (b) Fluorescence decay curves of additional combinations of diameter and nominal loading concentration. The bead mass concentrations range from 0.1 to 1 mg/ml, $\lambda_{\mathrm{fl,ex}} = 500$ nm, $\lambda_{\mathrm{fl,em}} = 550$ nm (488 and 554 nm for solution in water). The PMMA matrix leads to generally faster decay. Loading concentration and bead size have an impact on the decay kinetics.
Previously published, adapted with permission from Ref. [52]. ©2018 American Chemical Society.

that small beads can even exhibit slower overall decay kinetics than intermediate beads when the nominal loading concentration in the small beads is significantly lower. However, small beads exhibit additional faster decay components when the nominal loading concentration is high.

The origin of the slower decay components in intermediately sized and small beads could be related to the increasing impact of surface effects with decreasing diameter: the smaller the bead, the larger the near-surface volume fraction that can be penetrated by water. As the dye has a slower decay in water than in PMMA, the near-surface dye molecules surrounded by a PMMA-water mixture would contribute with slower rates to the overall decay. This is supported by the fluorescence intensity decay curve of the small weakly loaded beads in Fig. 4.4(b) being similar to the decay behavior of dye in aqueous solution. The faster decay components in small beads, however, cannot be explained by such an impact on the radiative decay rate due to water penetration.

Thus, the additional dependence of the decay kinetics on the dye loading concentration must be considered. High loading concentration with close dye-dye proximity might enhance near-surface aggregation and inter-molecular interaction such as energy transfer between dye molecules. Whereas fluorescent aggregates that are subject to dynamic quenching in the excited state would

contribute to the fluorescence decay kinetics, non-fluorescent aggregates that are statically quenched in the ground state would not influence the fluorescence decay. If static quenching in aggregates and energy transfer occurred side by side, then the energy transfer could again represent an additional decay channel. This additional decay channel would be visible in fluorescence decay measurements also in combination with transport of excitation energy to statically quenched aggregates. Thus, the short decay components in beads with higher nominal dye loading concentration might be caused by fluorescent aggregates with faster decay or by an energy transport to (possibly non-fluorescent) aggregates close to the surface. Both effects would be enhanced in small beads due to the higher effective dye concentration with decreasing bead size (see Sec. 4.1).

Further insight into decay dynamics is given by time-resolved fluorescence emission spectra (TRES) presented in Fig. 4.5. For intermediate beads with a low nominal dye loading concentration, Fig. 4.5(a) shows that the emission spectrum does not change with time. In contrast, the area-normalized TRES (TRANES) of small beads with high nominal dye loading concentration displayed in Fig. 4.5(b) exhibit a strong time-dependence of the spectral shape. The fluorescence

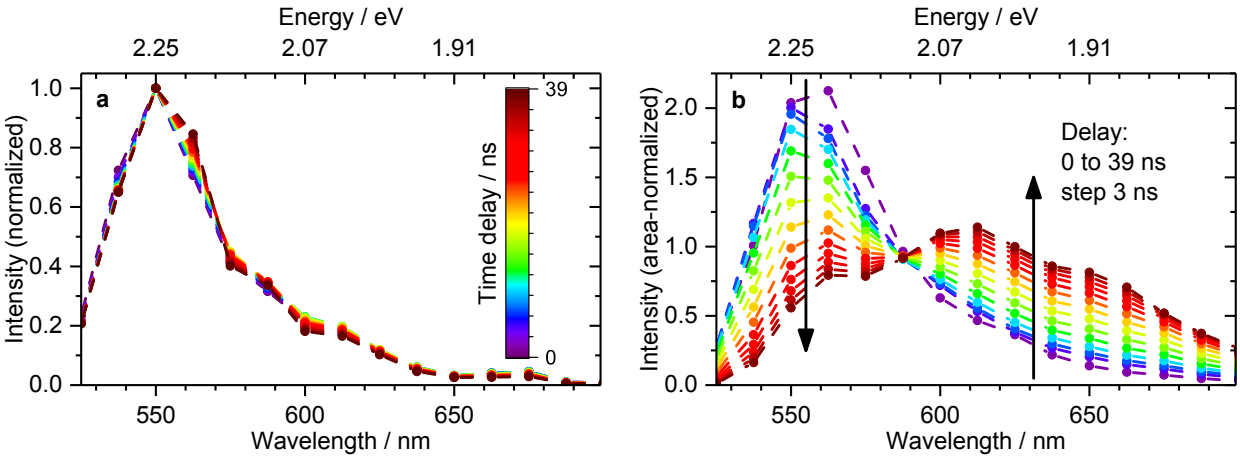

Figure 4.5: Time-resolved fluorescence emission spectra of beads with (a) 0.903 µmol/l nominal dye loading concentration, 5.45 µm mean diameter, 1 mg/ml bead mass concentration and (b) 361 µmol/l nominal dye loading concentration, 1.29 µm mean diameter, 10 µg/ml bead mass concentration. The spectra of intermediately sized, weakly loaded beads in (a) show no time dependence. The area-normalized spectra of small highly loaded beads in (b) clearly indicate different decay kinetics in different spectral regions.
Previously published, adapted with permission from Ref. [52]. ©2018 American Chemical Society.

intensity from spectral regions around the emission maximum decays significantly faster than the intensity on the long-wavelength side of the spectrum. Both regions are separated by an isosbestic point. Due to the much lower signal intensities at longer delay, there are no such striking differences in the steady-state spectra of the two samples.

The time-independence of the TRES of intermediately sized beads with low nominal loading concentration, Fig. 4.5(a), indicate that there is basically only one emissive species and no energy transfer processes except for possible homo-FRET. The TRANES with the isosbestic point in the small and highly loaded beads, Fig. 4.5(b), however, clearly indicate the presence of two species

with different fluorescence characteristics [1, 65].

Figure 4.6 shows the dependence of the mean lifetime on the emission wavelength. The mean lifetime is basically constant in large, weakly loaded beads within the limits of the measurement uncertainty. For small beads with high nominal dye loading concentration, a continuous increase of the mean lifetime at increased emission wavelengths is observed. Comparing the lifetime values

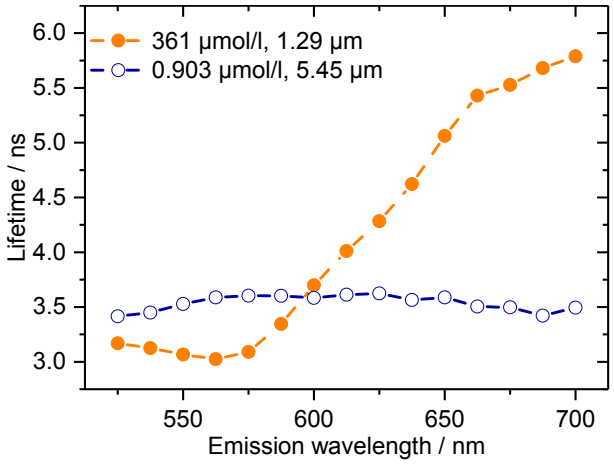

Figure 4.6: Fluorescence lifetime as a function of the emission wavelength for small, highly loaded beads (solid symbols) and intermediately sized beads with low nominal loading concentration (open symbols). Lifetimes were calculated by means of Eq. (3.3) from the fit curves. The lifetime in intermediate weakly loaded beads is basically wavelength-independent whereas small diameter and higher loading concentration lead to wavelength-dependent decay. This indicates different species and possible energy transfer in the latter.

across the two bead samples, one notices that the fluorescence decay in the small, highly loaded beads at shorter wavelengths is faster than the decay in intermediately sized, weakly loaded beads. Assuming an energy transfer, this accelerated decay is caused by the additional decay channel that transports excitation energy away from the ensemble of fluorescent core monomers to the near-surface aggregates. The fluorescence decay on the long-wavelength side of the spectrum may be dominated by the near-surface monomers. Possible water penetration into the near-surface regions of the beads prolongs the lifetime of these near-surface monomers by altering the radiative decay rate constant (cf. above). The low number of near-surface monomers could explain the weak impact on the steady-state spectra.
The changes in the fluorescence decay alone, however, only give indication for different species but do not prove the hypothesis of energy migration within the beads.

4.2.3. Fluorescence anisotropy

An energy transfer process such as FRET affects the fluorescence anisotropy due to depolarization even if it is energy transfer among equivalent molecules (homo-FRET) [27]. The concept of fluo-

rescence anisotropy was explained in Sec. 3.2.3. Irrespective of the bead diameter, such an energy transfer should cause a concentration-dependent decrease of the fluorescence anisotropy.

The spectrally resolved fluorescence emission anisotropy in intermediately sized and small beads of different nominal dye loading concentrations is shown in Fig. 4.7(a) and (b), respectively. The

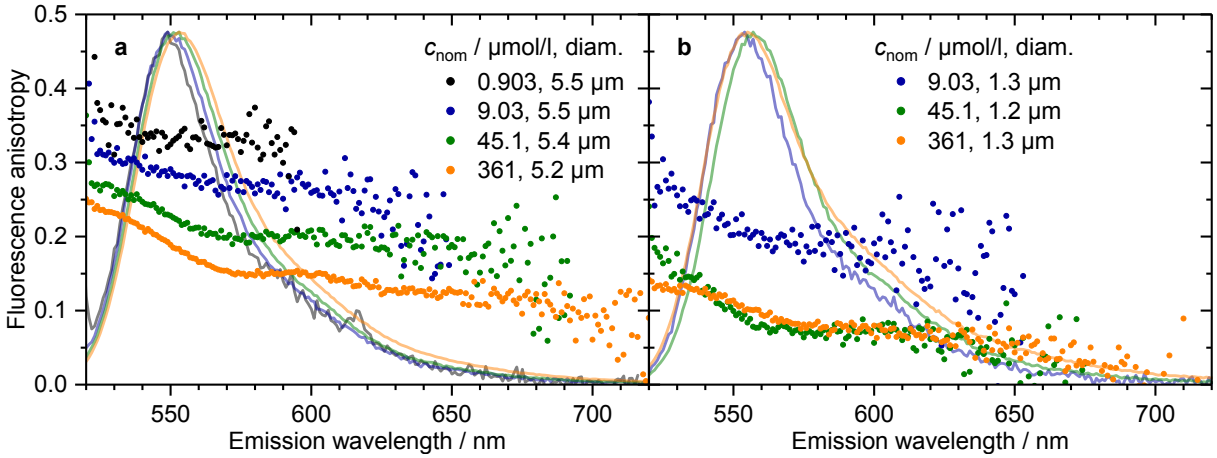

Figure 4.7: Fluorescence emission anisotropy spectra of (a) beads of intermediate size and (b) small beads, both with varying nominal dye loading concentrations. The excitation wavelength was $\lambda_{ex} = 500$ nm. Bead mass concentration were (a) 100 µg/ml and (b) 1 µg/ml. The emission spectra are displayed for association of the anisotropy features to spectral properties. Higher loading concentration results in lower anisotropy. The anisotropy is lower at longer wavelengths.

fluorescence anisotropy clearly depends on the nominal dye loading concentration for both (a) intermediately sized and (b) small beads. In both cases one observes a continuous decrease of the fluorescence anisotropy with increasing nominal dye loading concentration. The anisotropy is generally lower in small beads than in intermediately sized beads. However, there seems to exist a lower level of anisotropy which is reached in small beads at moderate nominal dye loading concentration. In addition, the fluorescence emission anisotropy depends on the emission wavelength: the anisotropy decreases with increasing wavelength. This wavelength dependence is more pronounced the higher the dye loading concentration is.

The spectrally integrated anisotropy values obtained from averaging within the FWHM of the emission bands are given in Fig. 4.8. It confirms the decrease of the anisotropy with increasing nominal dye loading concentration and the differences between small and intermediate beads. As the dye molecules are confined in the rigid polymer matrix of the beads, fluorescence anisotropy values close to the fundamental anisotropy are expected. The fundamental anisotropy is the theoretical maximum anisotropy in total absence of molecular motion [27]. In isotropic ensembles of luminophores with transition dipole moments of absorption and emission being parallel it amounts to 0.4 [1, 27]. The highest anisotropy should occur in the beads with the lowest loading concentration where energy transfer can be precluded. Among the beads studied, little depolarizing processes like energy transfer or reabsorption are expected for those with a nominal loading con-

centration of 0.903 µmol/l and a diameter of 5.5 µm. The spectrally integrated anisotropy for these beads is 0.34 ± 0.01, cf. Fig. 4.8, which is in acceptable agreement with the limiting anisotropy reported for Rh6G to be 0.372 in propane-1,2-diol [80]. Even though great care was taken re-

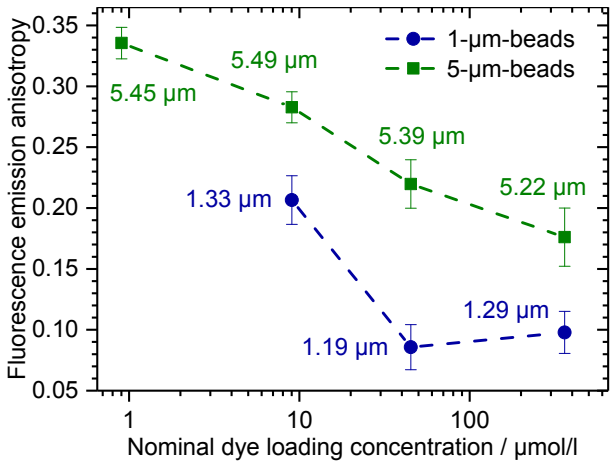

Figure 4.8: Spectrally integrated fluorescence emission anisotropy as a function of the nominal dye loading concentration for beads of small and intermediate diameters. The anisotropy decreases with increasing dye concentration. It is generally lower in smaller beads, indicating a higher probability for energy transfer.
Previously published, adapted with permission from Ref. [52]. ©2018 American Chemical Society.

garding appropriate bead concentrations, light scattering, which is known to depolarize light [27], cannot be completely avoided. Furthermore, torsional molecular motion may also occur in rigid environments at room temperature leading to a reduced anisotropy [81].

The observed decrease in fluorescence anisotropy with increasing nominal dye loading concentration gives evidence for a depolarization process that depends on the mean distance between the dye molecules and, therewith, for energy transfer or migration. The higher the dye concentration, the shorter the average distance between dye molecules and the higher the probability for energy transfer. The lower limit of the anisotropy in small beads indicates that the efficiency of the energy migration process is restricted. Such a behavior has been observed in Rh6G-doped films before [74] and it was explained by trapping of the excitation energy. When the traveling distance is large enough, the excitation energy will almost certainly be trapped. Theoretically possible longer traveling distances are not reached in practice and thus there is a lower limit of the anisotropy. A similar explanation holds true for energy migration in the beads: once the dye concentration is high enough, the excitation energy assuredly reaches the bead surface and will be trapped by the near-surface aggregates. The smaller the beads, the shorter is the maximum possible distance of an initially excited molecule to the surface and reaching the required dye concentration for maximum depolarization is more likely.

The wavelength dependence of the fluorescence emission anisotropy noticeable in Fig. 4.7 possibly has the following reason. The photon emission from the short-wavelength side competes with the relatively high FRET rates when neighboring molecules at short distances are present. Thus, photon emission on the short-wavelength side rather stems from molecules that only have neighbors

at further distance and they consequently do not take part in the energy migration process. These molecules then emit more polarized light. Molecules emitting on the long-wavelength side act as energy sinks for the transfer process. They trap the excitation energy after several transfer steps and consequently their polarization is uncorrelated with the excitation polarization.

As was shown in Fig. 4.8, the fluorescence anisotropy is generally lower in small beads than in intermediately sized beads. A contribution from rotational motion of the beads to the depolarization can, however, be excluded: the rotational correlation time Θ is given by [1, 82]

$$\Theta = \frac{\eta V}{k_\mathrm{B} T} ,$$

where η is the viscosity of the surrounding medium, $V = V_\mathrm{bead}$ is the volume of the bead, k_B denotes the Boltzmann constant, and T is the temperature. Even for beads with a diameter of only 1 µm, one obtains $\Theta > 100$ ms which exceeds the fluorescence lifetimes of the dye-loaded beads by several orders of magnitude. Thus, the differences in anisotropy between beads of different diameters but same nominal dye loading concentration are not related to size-dependent rotational speed. Rather the higher effective dye concentration in small beads (cf. Sec. 4.1) is responsible for a higher probability of energy transfer and consequently the stronger depolarization.

In summary, the dependence of the anisotropy on the dye loading concentration is evidence for energy migration in the beads.

4.2.4. Fluorescence quantum yield

So far, only effects on the fluorescence emission of the beads were considered. However, non-fluorescent aggregates are undetectable to fluorescence measurements. It is therefore unclear whether, or to which extent, the assumed near-surface aggregation actually quenches the excitation energy.

Figure 4.9 shows the quantum yield as a function of nominal dye loading concentration and sorted by bead diameter ranges. At low loading concentrations the quantum yield is as high as in aqueous solution, namely around 0.90. Increasing the nominal dye loading concentration results in decreasing quantum yield with significant differences between beads of different diameter. The decrease is minor for moderate loading concentrations in large and intermediately sized beads. It becomes notable only at high loading concentrations where the quantum yield is reduced to approximately 0.8. In contrast, small beads exhibit an extreme decrease in quantum yield. Here, the quantum yield decreases almost down to 0.2. The nominal dye loading concentration is comparable between the samples since the amount of MMA used and the overall reaction volume in the synthesis were the same for all samples (cf. Sec. 3.5).

A generally lower quantum yield in small beads is most likely caused by their much higher effective dye concentration which is not represented by Fig. 4.9 and differs from the nominal concentration (cf. Sec. 4.1). Especially the high dye concentrations in the stabilizer shell and the larger surface-to-volume ratio enhance the effect of the presumed surface-related aggregation and quenching. Higher dye concentrations in small beads favor not only aggregation, but also energy migration whose existence was already suggested by the measured dependence of the fluorescence anisotropy on the loading concentration. Such an energy transfer would further decrease the quantum yield: in

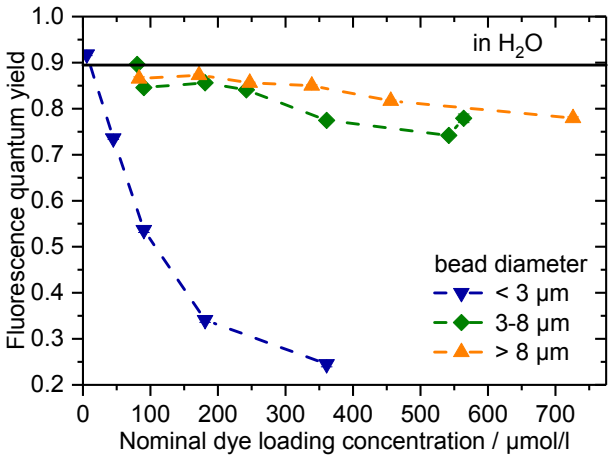

Figure 4.9: Dependence of the fluorescence quantum yield on the nominal dye loading concentration grouped by bead diameter. The quantum yield of Rh6G in aqueous solution is indicated by the horizontal line. The quantum yield in beads decreases with increasing nominal dye loading concentration, the effect is stronger in small beads.
Previously published, adapted with permission from Ref. [52]. ©2018 American Chemical Society.

addition to static quenching, it transports energy from fluorescent core monomers with potentially high quantum yield to quenched near-surface aggregates with very low quantum yield.

It is worthwhile to take into account the relation between quantum yield and lifetimes, Eq. (2.6). As stated earlier, static quenching by formation of non-fluorescent aggregates would be invisible to fluorescence measurements whereas it affects the quantum yield. The opposite, dynamic quenching, has an impact on both decay dynamics and quantum yield. It basically alters the non-radiative rate constant γ_{eq} in Eq. (2.5) and thus the overall decay rate constant γ. Under these circumstances, fluorescence quantum yield ϕ_{fl} and fluorescence lifetimes are related by [27]

$$\phi_{\mathrm{fl}} = \frac{\tau}{\tau_{\mathrm{ra}}} \,.$$

Thus, for dynamic quenching at constant radiative lifetime τ_{ra}, quantum yield and lifetime should exhibit a linear relation. Our experimental findings, however, show that the decrease in quantum yield, shown in Fig. 4.9, is much stronger than the decrease in fluorescence lifetime, shown in Fig. 4.4, for increasing the dye loading concentration. This indicates the contributions from some type of dynamic quenching as well as static quenching processes.

The dependence of the quantum yield on the nominal dye loading concentration and the bead diameter supports the assumption of quenched near-surface aggregates. The stronger quenching in small beads is due to the larger surface-to-volume ratio and the size-dependent dye loading efficiency.

4.2.5. Synopsis

There are two concurrent mechanisms for the incorporation of Rh6G in the PMMA microbeads. Core dye molecules are sterically incorporated during bead growth and stabilizer-dye complexes form a shell of near-surface dye monomers and aggregates. Thus, three distinct species of Rh6G occur in these PMMA beads: core monomers, near-surface monomers, and near-surface aggregates. This is illustrated in Fig. 4.10. The core monomers exhibit the optical-spectroscopic properties of

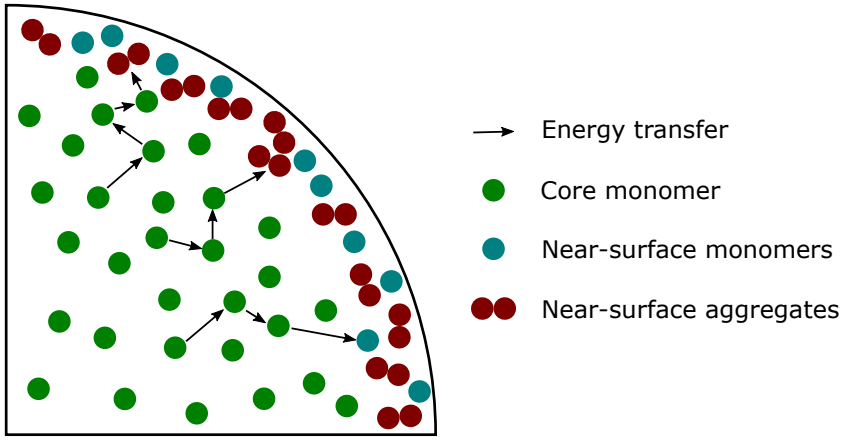

Figure 4.10: Schematic drawing of the assumed dye distribution in dye-loaded beads. The core of the bead mainly contains dye monomers with a possible concentration gradient towards the surface. Close to the surface, specific incorporation generates high local dye concentration and aggregation. Directed energy migration could contribute to dynamic quenching.

fluorescent monomers in PMMA environment which means slightly redshifted fluorescence excitation spectra and faster fluorescence decay compared to aqueous environment. The near-surface monomers are exposed to water that penetrates the outer regions of the PMMA beads. This causes slower fluorescence decay and the spectral broadening. The near-surface aggregates form at high nominal dye loading concentrations. They are assumed to be strongly quenched and thus reduce the fluorescence quantum yield. At high dye loading concentrations, the intermolecular distances become short enough to allow excitation energy migration due to FRET as shown in Fig. 4.10. A possible concentration gradient towards the surface could result in a directed energy migration. The energy migration then mainly transports energy from the core monomers to the near-surface aggregates. Thereby, it represents an additional decay channel and consequently adds fast components to the fluorescence decay behavior. Additionally, energy migration reduces the fluorescence anisotropy. All effects are more pronounced in small beads due to the larger surface-to-volume ratio.

To examine whether the proposed energy migration could indeed cause the observed changes in the decay kinetics and the quantum yield, a random walk model was developed and will be presented in the following section.

D	Nom. loading	Eff. loading		Dye-dye dist.	QY	τ
µm	µmol/l	nmol/mg	amol/µm^3	nm		ns
1.2	45.1	0.64(4)	0.76(5)	16.1(4)	0.74	3.94
1.3	361	3.90(9)	4.64(11)	8.81(7)	0.25	3.17
1.3	9.03				0.92	3.95
1.9	361	3.51(9)	4.18(11)	9.12(7)		3.52
1.9	45.1	0.57(4)	0.68(5)	16.7(4)		
2.3	181	1.98(6)	2.36(7)	11.0(1)	0.34	3.34
2.4	181	2.23(6)	2.65(7)	10.61(10)		
2.5	90.3	0.96(5)	1.14(6)	14.0(2)	0.54	3.08
3.0	181	2.18(6)	2.59(7)	10.7(1)		
3.9	361	2.02(5)	2.40(6)	10.96(10)		3.73
3.9	181	1.63(5)	1.94(6)	11.8(1)		
4.1	45.1	0.30(4)	0.36(5)	20.7(9)		3.43
4.1	9.03					3.57
4.2	181	1.22(5)	1.45(6)	13.0(2)		3.58
5.0	45.1	0.14(4)	0.17(5)	26(2)		
5.2	361	1.03(5)	1.23(6)	13.7(2)		
5.7	90.3				0.85	3.41
5.9	90.3	0.18(4)	0.21(5)	25(2)		
6.6	361	0.64(4)	0.76(5)	16.1(4)	0.77	3.31
6.6	542				0.74	3.30
6.7	181	1.1(2)	1.3(2)	13.5(8)	0.86	3.35
7.6	242				0.84	3.25
7.6	564				0.78	3.30
7.7	80.3	0.1(4)	0.1(5)	26(2)	0.90	3.38
8.1	726				0.78	3.37
9.5	456				0.82	3.34
10.0	172	0.23(4)	0.27(5)	23(1)	0.87	3.36
10.2	83.1	0.12(4)	0.14(5)	28(3)	0.87	3.37
10.2	247				0.86	3.33
11.0	339	0.40(4)	0.48(5)	18.8(6)	0.85	3.34
12.5	137	0.18(4)	0.21(5)	24(2)		
13.4	209	0.22(4)	0.26(5)	23(1)		
13.8	60.5	0.08(4)	0.10(5)	33(6)		
14.2	120	0.15(4)	0.18(5)	26(2)		

Table 4.1: Overview of the properties of all bead samples included in the study. The bead diameter is denoted D, τ is the intensity-averaged fluorescence lifetime. The nominal loading concentration is the dye concentration during synthesis. The effective loading concentration represents the actually incorporated amount of dye. The dye-dye distances were calculated by means of Eq. (4.4). Values in brackets give uncertainties.

4.3. Random walks for energy migration simulation

The model in Fig. 4.10 proposed for explaining the observed optical-spectroscopic characteristics includes an energy migration process that transports energy from molecules in the core of the beads along a possible concentration gradient towards a quenching shell of aggregates near the surface. Such a behavior can be simulated with the aid of a random walk algorithm. The random walk simulations should allow for comparison of the experimentally determined fluorescence decay kinetics and quantum yields with trends observed in the simulations. A quantitative comparison, however, is not attempted since the exact dye distribution in the beads is not known and therefore an assumed distribution must be used in the simulations.

Figure 4.11 illustrates how the general concept of Fig. 4.10 is implemented in the random walk model. A bead of radius R is divided into a core region with fluorescent molecules (green) and a shell of thickness d_{qs} (shaded region). The molecules in the shell are quenching centers (brown),

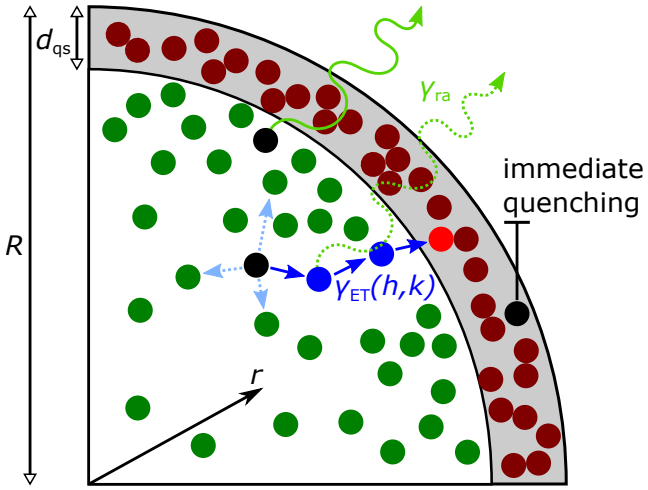

Figure 4.11: Schematic drawing of the principle of the random walk simulation. The bead of radius R is divided into a core and a quenching shell with thickness d_{qs}. Dye molecules in the core (green) may emit photons by radiative decay with rate constant γ_{ra} or transfer energy to neighboring molecules with rate constants γ_{ET}.

which means that they are unable to emit photons. An excited molecule (black) in the bead core can either lose its energy by radiative decay (green arrows) or transfer its energy to another molecule (blue arrows). Once the excitation energy reaches a molecule in the quenching shell (red) or is emitted as a photon, the random walk terminates. When a molecule in the quenching shell is directly excited, immediate quenching occurs and the random walk terminates. This model contains some simplifications with respect to Fig. 4.10 concerning molecular species and the strict distinction between quenching and emitting molecules.

The algorithm developed for the random walk is summarized in Fig. 4.12. At first, molecule positions have to be generated according to an appropriate radial distribution. As the actual dye distribution in the beads could not be measured, and for the sake of straightforward computation,

monomial distributions of the form

$$p(r) = \frac{\eta + 3}{R^{\eta+3}} r^{\eta}\,, \qquad \int_0^R r^2 p(r)\,\mathrm{d}r = 1 \tag{4.5}$$

are chosen. Here, r is the radial distance from the center of a bead with radius R as indicated in Fig. 4.11 and η is the monomial exponent that determines the steepness of the radial concentration gradient. More details on the random number distributions can be found in Sec. A.2.1. A run of the random walk algorithm begins with the random choice of a starting point (black circles in Fig. 4.11) from the generated molecule positions. This starting point represents the molecule that absorbed an incoming photon in an experiment. If this position is within the quenching shell, the excitation is assumed to be immediately quenched. For a position in the bead core, the next step is to calculate the transfer rate constants to all other molecules (indicated by the blue arrows in Fig. 4.11). These transfer rate constants γ_{ET} are of the Förster type [27]:

$$\gamma_{\mathrm{ET}}(h,k) = \gamma_{\mathrm{ra}} \frac{R_F^6}{d_{hk}^6}\,, \tag{4.6}$$

where R_F is the Förster radius and d_{hk} denotes the distance between two molecules. The orientation of the transition dipole moment is not considered as the molecules are assumed to be randomly oriented in the beads. Thus, the orientation of the molecules should, on average, play no role. An estimate of R_F [see Eq. (2.7)] based on a fluorescence excitation spectrum scaled to the molar

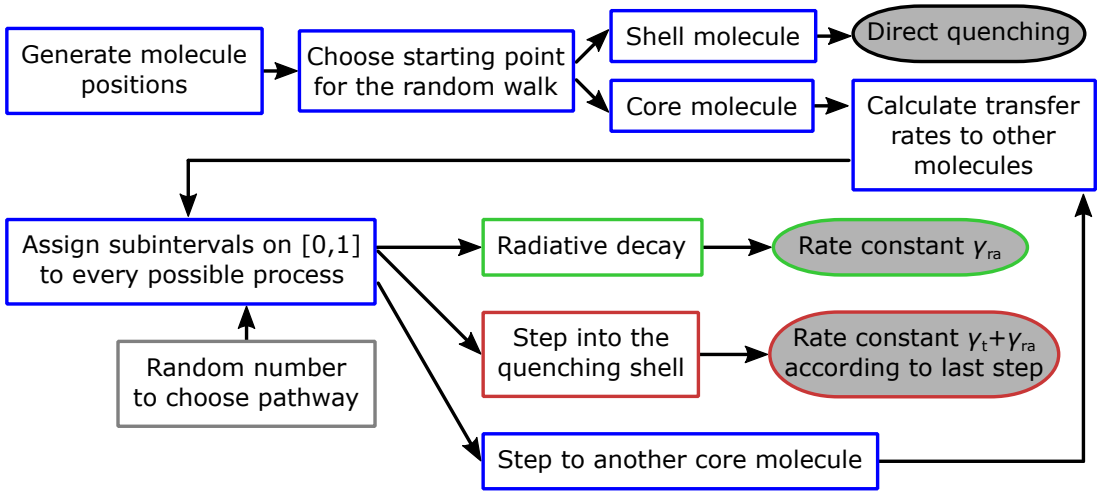

Figure 4.12: Flow chart of the random walk algorithm for simulation of energy migration depicting one run and the generation of the positions of the molecules. A run begins with the choice of a starting point for the random walk. The run either terminates directly due to immediate quenching or energy transfer rates to all other molecules are calculated. The next step is chosen from all possibilities according to the transfer rates. A step to another core molecule leads to recalculation of the transfer rates. Radiative decay or a step into the quenching shell terminate the run.

extinction coefficient of Rh6G in PMMA films [83] and a spectrally corrected, area-normalized emission spectrum gave $R_F \approx 5$ nm which is in reasonable agreement with values reported before [84]. Using this estimate in Eq. (4.6), the algorithm calculates the transfer rate constants to all surrounding molecules. The radiative decay rate constant is assumed to be $\gamma_{\mathrm{ra}} = (3.75\ \mathrm{ns})^{-1}$, which corresponds to the effective fluorescence lifetime of the large dye-loaded beads with low dye loading concentration. This was used as a standard since the impact of surface-related effects and energy transfer is expected to be negligible in this case. The probabilities for all transfer possibilities and radiative decay are calculated by dividing each respective rate constant by the sum of all rate constants. A subinterval on $[0, 1]$ with length equal to the probability is assigned to each possible process. Thus, pathways with higher probabilities correspond to larger subintervals. The value at the upper boundary of each subinterval is equal to the cumulative probability. This is illustrated in Fig. 4.13. Another random number is generated to choose the next step of the ran-

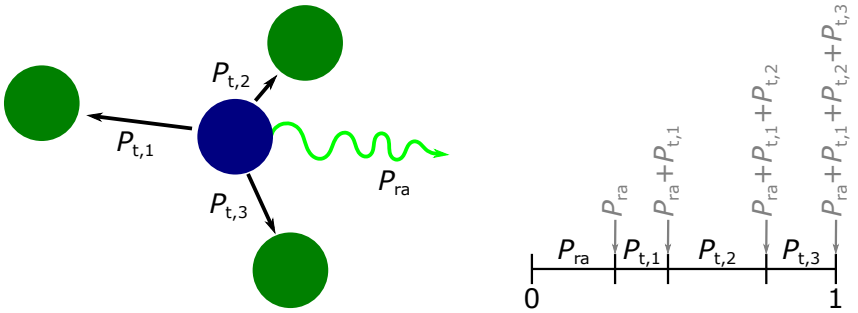

Figure 4.13: Assignment of the probabilities of all possibilities for the next step in the random walk to subintervals on $[0, 1]$. The borders of the subintervals are the cumulative probabilities. Another random number is used to choose one of the subintervals and thereby determine the next step of the random walk.

dom walk. Depending on which interval contains this random number, it determines whether the excitation energy is emitted as a photon by radiative decay or whether it is transferred to another molecule and if yes, to which. This procedure, though mathematically incorrect on uncountable sets, should yield correct results for discrete numbers. If radiative decay or transfer to the quenching shell occurs, the random walk terminates. Otherwise, the cycle starts over again and the rate constants and probabilities are recalculated according to the position of the now excited molecule. Thus, a run of the random walk only ends with radiative decay or reaching the quenching shell, as indicated by the gray terminal boxes in Fig. 4.12. The overall process is repeated several times and each such run corresponds to one absorbed photon.

In order to obtain a simulated decay curve based on this random walk simulation, a decay rate constant needs to be assigned to each run of the simulation. These decay rate constants are used to form a superposition of mono-exponential decays that represent the fluorescence decay curve. The rate constants are obtained considering the following. The rate of photon emission is given by the product of the radiative rate constant and the number of excited molecules, $\gamma_{\mathrm{ra}} n^*(t)$. In the case of isolated molecules, the only processes that change the number of excited molecules $n^*(t)$

are monomolecular processes:

$$\frac{\mathrm{d}n^*(t)}{\mathrm{d}t} = -\left(\gamma_{\mathrm{ra}} + \gamma_{\mathrm{iq}}\right) n^*(t)$$

where γ_{ra} and γ_{iq} are the rate constants of radiative de-excitation and internal quenching as in Eq. (2.2). Thus,

$$n^*(t) = n^*(0)\mathrm{e}^{-(\gamma_{\mathrm{ra}}+\gamma_{\mathrm{iq}})t}$$

and the fluorescence intensity shows a mono-exponential decay following $\gamma_{\mathrm{ra}} n^*(t)$. An energy transfer by FRET among an ensemble of identical molecules (homo-FRET), however, does not add an additional decay channel as the number of excited molecules $n^*(t)$ is not altered by such a homotransfer. This means that the observed fluorescence rate only depends on the number of excited molecules [63] and is not changed by homo-FRET [27]. Consequently, those runs of the random walk simulation that terminate with a radiative decay (green arrows in Fig. 4.11) contribute the radiative decay rate constant γ_{ra} to the overall decay, irrespective of the number of steps taken before in the random walk. In contrast, for runs that end with a step into the quenching shell, this last step affects the number of excited molecules $n^*(t)$ and the rate constant of this last transfer step (blue arrow into the shell in Fig. 4.11) increases the decay rate. Thus, each run is characterized by an individual effective decay rate constant: Either the radiative rate constant is obtained when the excitation energy is emitted in a radiative decay or the sum of the rate constant of the last energy transfer step which led to the quenching shell and the radiative rate constant (both together characterize the effective rate constant for this molecule) is assigned to that run. This approach contains a simplification as it neglects a detailed consideration of all possible decay channels other than the radiative decay and the step to one specific molecule in the shell. When the start position was within the quenching shell, the respective run does not contribute to the rate constants at all. The overall decay kinetics are a superposition of mono-exponential decay curves with the respective decay rate constants γ_j of each run. So, the overall decay is given by

$$I(t) = I(0) \sum_{j=1}^{M'} \mathrm{e}^{-\gamma_j t}$$

with M' being the subset of runs with start positions outside the quenching shell. All runs in M' contribute a decay curve with the same amplitude rather than the same area since

$$I_j(t) = \gamma_{\mathrm{ra}} n_j^*(t) = \gamma_{\mathrm{ra}} n_j^*(0)\mathrm{e}^{-\gamma_j t}$$

and $n_j^*(0) = 1 \;\forall\; j$. The simulated decay curves were convoluted with an instrument response function (IRF) of the TCSPC setup and random noise counts were added to allow straightforward comparison with experimental data. Finally, a simulated quantum yield was calculated as the ratio of runs ending with radiative decay to the total number of runs.

As an example, consider a random walk simulation with five runs: one that is terminated by immediate quenching, two that end with photon emission, and two that are terminated by a step into the quenching shell. The simulated decay curve consists of two identical exponential functions with the radiative rate constant and two exponential functions with additional transfer

rate constants depending on the distance in the last step:

$$I(t) \sim 2\mathrm{e}^{-\gamma_{\mathrm{ra}}t} + \mathrm{e}^{-(\gamma_{\mathrm{ra}}+\gamma_{\mathrm{ET},1})t} + \mathrm{e}^{-(\gamma_{\mathrm{ra}}+\gamma_{\mathrm{ET},2})t}\,.$$

The immediately quenched run does not contribute to the decay. The quantum yield is 0.4.

All numerical simulations have been performed with custom-made *Octave* [85] scripts. A more detailed description of the mathematics and the computation of the molecule distributions can be found in Sec. A.2. The number of runs in each random walk simulation was at least 1000 to ensure statistically reliable outcomes. For a discussion of convergence and reproducibility, see Sec. A.3.

4.3.1. Shape of the dye distribution

At first, the assumed class of functions, Eq. (4.5), for the dye distribution inside the beads has to be tested and, in case that the simulated results resemble the experimental data, the most suitable function of the set must be found. The smallest beads with highest dye loading concentration (1.29 µm diameter, 361 µmol/l nominal dye loading concentration) are the system of choice for comparison between experimental data and simulations as they show the most distinct indication for energy migration and an inhomogeneous dye distribution.

The effective dye loading concentration (cf. Fig. 4.1 and related discussion) in these beads amounts to 4.64 amol per $\mu\mathrm{m}^3$ bead volume and thus the mean dye-dye distance is 8.8 nm according to Eq. (4.4). For the simulations, this mean dye-dye distance is assumed to be $d_{\mathrm{dd}} = 8.5$ nm, the bead diameter is set to $D = 1.3$ µm. The thickness of the shell of quenching aggregates is set to $d_{\mathrm{qs}} = 1.4$ nm as a rough estimate of ten C-C bonds with σ and π contribution [56]. The undisturbed radiative lifetime $\tau_{\mathrm{ra}} = \gamma_{\mathrm{ra}}^{-1}$ of Rh6G in a PMMA matrix and the FRET radius R_{F} are set to $\tau_{\mathrm{ra}} = 3.75$ ns and $R_{\mathrm{F}} = 5$ nm as discussed previously. It turned out that the energy transfer rate constants obtained from simulations produce fluorescence decay kinetics whose initial decay is shorter than the IRF of the available spectroscopy equipment. Hence, if a sample in an experiment exhibited such short decay characteristics, it would be broadened by the IRF (FWHM ≈ 250 ps). This broadening would prevent a comparison between simulated and experimental data. Therefore, the simulated decay curves have been convoluted with the IRF of the setup as well. A typical set of parameters for the simulations is listed in Tab. A.1.

Simulated decay curves for varying exponent η in the dye distribution are displayed in Fig. 4.14(a) together with experimental data and the IRF of the employed setup. The spike-like feature in the decay curves at around 25 ns is caused by the convolution with the IRF which exhibits a secondary pulse. For small exponents η, the decay kinetics closely resemble that of decay without any energy transport processes. In other words, the decay curves are mono-exponential and similar to those of large weakly loaded beads for small values of η. With increasing values of η, the decay kinetics become increasingly multi-exponential. Reasonable similarity to the experimentally measured decay curves of the small and highly loaded beads is reached for $\eta \approx 120$.

Along with the changes in decay dynamics, a decrease of the fluorescence quantum yield was also observed in experiments. The simulated overall fraction of quenching in the de-excitation process is shown in Fig. 4.14(b) along with the contributions of quenching by transport of excitation

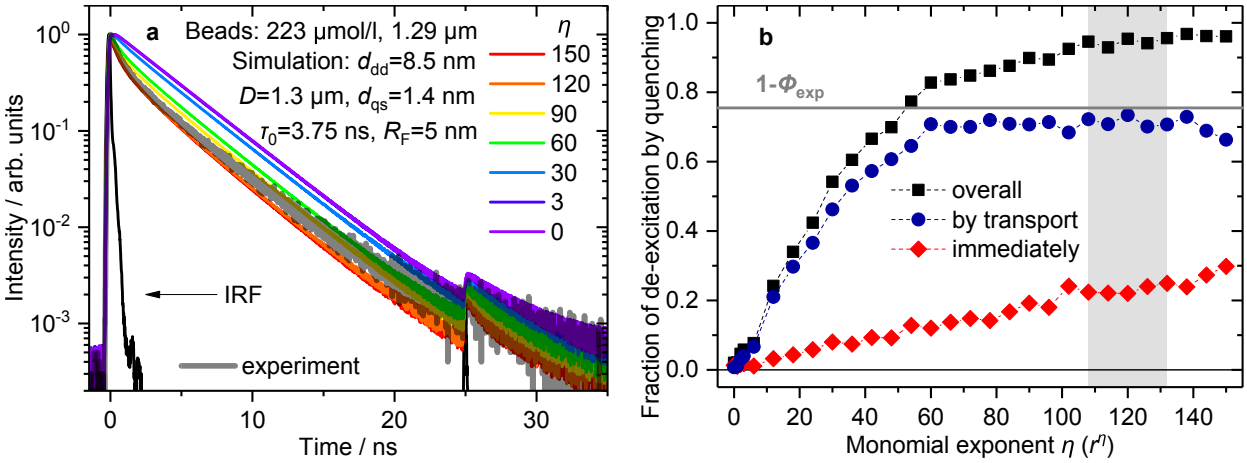

Figure 4.14: Effect of different exponents η in the radial r^η dye distribution. (a) Simulated decay curves color-coded for the respective exponent shown together with a measured decay curve of a bead sample (gray, semi-transparent line). Reasonable agreement is found for exponents as large as $\eta \approx 120$. The spike at 25 ns is caused by the convolution with the IRF. (b) Efficiency of different decay pathways in dependence on the exponent η. The horizontal gray line indicates the experimentally determined quenching efficiency. The simulated quenching efficiency tends to be too high.

energy to the quenching shell and the immediate (static) quenching due to excitation of molecules that are located in the quenching shell. The overall fraction is the sum of the transport and immediate quenching efficiency values (no other quenching pathways were included in the random walk simulations). The sum of fluorescence quantum yield and the overall quenching efficiency is unity by definition. For increasing values of η, Fig. 4.14(b) shows that the overall fraction of de-excitation due to quenching continuously increases until it reaches almost 100 %. Thus, quenching is apparently mainly driven by energy transport when strong concentration gradients and sufficiently short distances between the dye molecules exist. The steeper dye concentration gradients caused by the higher exponents η lead to strongly directed transport towards the surface. However, the efficiency of the quenching does not only increase due to the steeper concentration gradient and the resulting more directed transport. Also, a higher fraction of molecules is located closer to the surface in the case of distributions with larger exponent η. Consequently, the average distance to the surface decreases, which in turn decreases the distance that needs to be traversed by the transport process to reach the quenching shell. A maximum transport efficiency seems to be reached for $\eta \approx 60$. The increasing fraction of immediately quenched excitation energy simply stems from the larger fraction of molecules that are located in the quenching shell as η increases.

For comparison with experimental data, the experimentally observed quenching efficiency was calculated from the experimentally determined quantum yield ϕ_{exp} as $1 - \phi_{\text{exp}}$. The result for beads with 1.29 µm diameter and a nominal dye loading concentration of 361 µmol/l is indicated by the horizontal gray line in Fig. 4.14(b). The simulated overall quenching efficiency exceeds the experimental value for $\eta \approx 60$. Thus, a match with the experimental data is reached for much

lower values of η than are required to achieve decay kinetics that resemble experimental fluorescence decay curves, cf. Fig. 4.14(a). The shaded region in Fig. 4.14(b) indicates the values of η appropriate to generate simulated decay that is comparable with experimentally observed decay curves. Within this range, the overall quenching efficiency is clearly overestimated by the simulations. Possible reasons are either a finite non-zero quantum yield of the near-surface aggregates or a contribution of the near-surface monomers that were neglected in the simulations. In order to match the experimental results, the aggregates would have to exhibit a residual quantum yield of ≈ 0.2, which would be significantly higher than values on the order of 10^{-4} to 10^{-3} reported for solutions [84]. More likely, the near-surface monomers with redshifted emission and slower decay could act as radiative energy traps with finite quantum yield. The energy transfer could still introduce fast initial decay components for the core monomers but the quantum yield of the radiative traps was finite.

The simulations provide theoretical results comparable to experimental data. The meaning of the precise values of the exponent η required to reach this comparability, however, is questionable. Values of $\eta \approx 120$ lead to much higher molecular packing density close to the bead surface than in the core. In fact, such a distribution is rather step-like as depicted in the comparison between two distributions in Fig. 4.15. Panel (a) shows the radial distribution for $\eta = 3$ and panel (b)

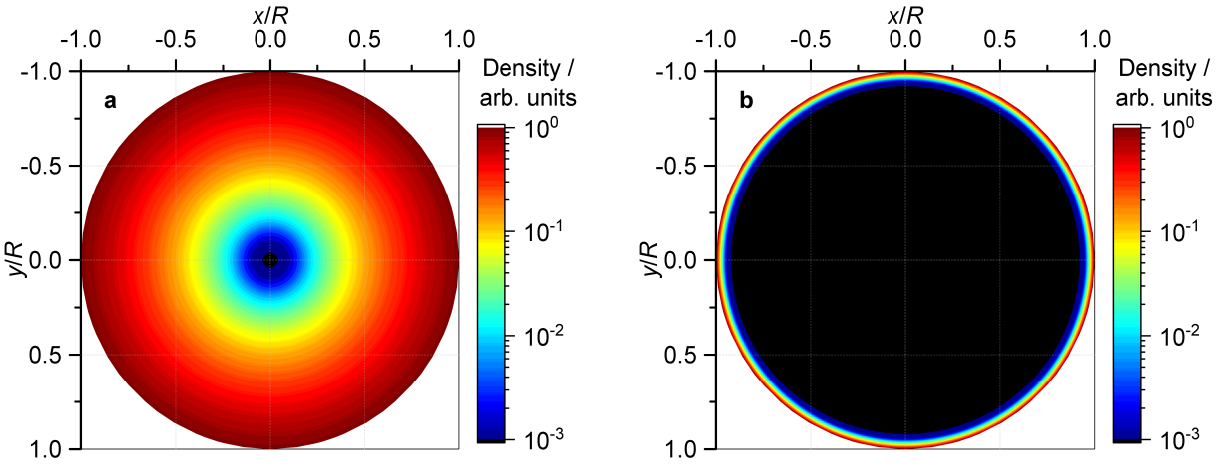

Figure 4.15: Representation of the radial dye distributions in a plane for (a) $\eta = 3$ and (b) $\eta = 120$. For the larger exponent, most of the dye molecules are located very close to the surface and the core is basically free of dye.

shows the radial distribution for $\eta = 120$. On the one hand, the precise values of such large exponents may not exactly be physically meaningful. On the other hand, a step-like distribution of the dye molecules is in line with the conclusion of an AOT-Rh6G shell drawn from the discussion in Sec. 4.1. With increasing exponent, the core of the beads will be basically free of molecules whereas most of the molecules are located very close to the surface. This complies with the very low value of the parameter describing the incorporation of the dye molecules in the core in the fit of Eq. (4.2) to the data in Fig. 4.1.

A more quantitative view on the dye distributions in the simulations is given in Fig. 4.16. Radial probability distributions integrated over intervals of size $\Delta r = 0.1$ nm for different η are shown for a bead diameter of 1.3 µm and a mean dye-dye distance of 8.5 nm. This means, the probability values represent the probability that a randomly picked molecule is located within a shell of 0.1 nm thickness around the respective radial position. The sum of all these probability values amounts to 1 since a molecule must be somewhere in the bead. For small exponents in the radial distributions,

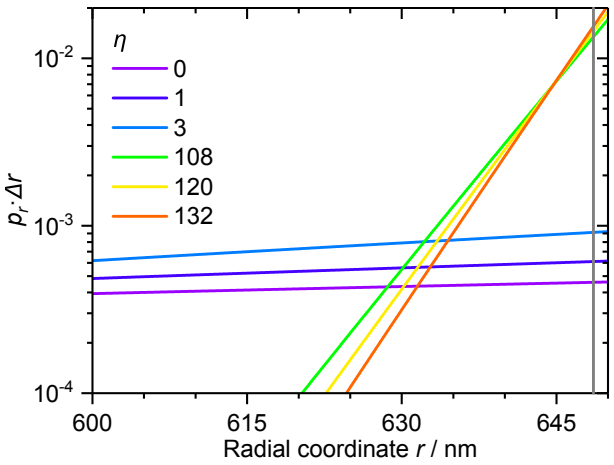

Figure 4.16: Probability distributions integrated within radial intervals of 0.1 nm in the outer 50 nm of a bead as a function of the radial coordinate for different exponents η. For the large exponents required to mimic the experimental data, the majority of the molecules is located within around 25 nm from the bead surface.

the molecules are distributed relatively evenly across the bead volume. The dependence on the diameter even for the constant distribution ($\eta = 0$) is caused by the increasing volume of a volume element with defined thickness in r with increasing distance from the origin, cf. Eq. (4.5) or Sec. A.2.1. Indeed, for distributions with large η (108–130), the probability of finding a molecule in a respective interval falls rapidly after moving only tens of nanometers away from the surface. Thus, for such large exponents only the region within around 25 nm from the surface plays a role in the simulation of the fluorescence of the beads as there are virtually no dye molecules further away from the surface. However, since the quenching shell is assumed to be only 1.4 nm thick (vertical gray line in Fig. 4.16, estimation based on molecular size of Rh6G), a majority of around 75 % of the molecules are still outside the quenching shell and may therefore participate in energy transfer processes. The distributions in larger beads will differ in absolute numbers as the overall probability is normalized to 1. Consequently, more dye molecules then have larger absolute distances to the surface but not relative to the bead diameter.

Since the actual dye distribution could not be determined, the class of monomial functions is assumed to represent the distribution within the framework of experimentally deduced knowledge. Nevertheless, the simulations do not take into account effects of possible water penetration into the near-surface region of the beads and respective change of the radiative rate constant. Thus, slower components that are present in the experimental data cannot be reconstructed by the simulations.

In summary, the random walk model is capable of approximating experimental findings. It may therefore be used to assess the hypothesis of energy migration in dye-loaded polymer beads by comparing experimental and simulated data in dependence on bead diameter and dye loading concentration.

4.3.2. Thickness of the quenching shell

The actual thickness of the quenching shell could not be determined by experimental methods and therefore has to be estimated. It is, however, crucial to the simulations as it determines the fraction of molecules that are considered being quenched. Moreover, it affects the maximum steepness of the dye distribution: the slope of the distribution is higher at closer proximity to the surface. Thus, the thicker the quenching shell is, the smaller the maximum slope for the molecules outside the shell.

When the thickness of the quenching shell is varied, the simulated decay kinetics show the response displayed in Fig. 4.17(a). For thick shells, the decay kinetics are mono-exponential. Only when the shell thickness is decreased can multi-exponential decay with fast components be observed. For a more comprehensive picture, the efficiencies of the different quenching pathways are given

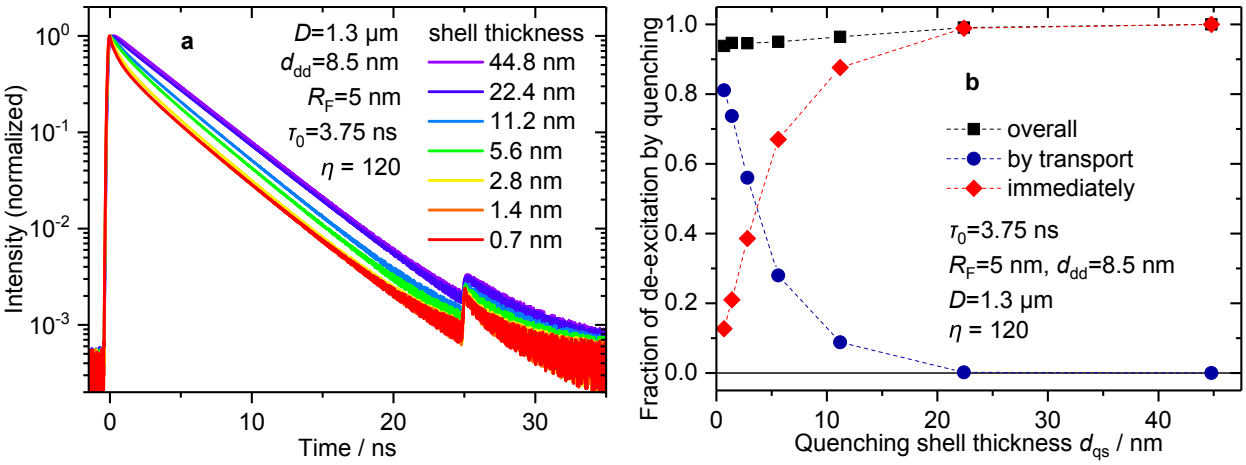

Figure 4.17: Influence of the variation of the thickness of the quenching shell. (a) Simulated fluorescence decay dynamics in dependence of the quenching shell thickness. The thicker the shell, the weaker the impact of energy migration on the decay dynamics. (b) Efficiency of de-excitation pathways for different values of quenching shell thickness. Immediate quenching drastically gains importance with increasing shell thickness.

in Fig. 4.17(b). The overall quenching efficiency is almost independent of the thickness of the quenching shell. The immediate quenching and transport efficiency, on the contrary, change significantly when the thickness of the quenching shell varies. Whereas the contribution of immediate quenching increases with increasing quenching shell thickness, the transport efficiency drastically decreases until it is basically zero.

The multi-exponential decay observed in Fig. 4.17(a) for decreasing thicknesses of the quenching shell is associated with the energy migration. Thus, thicker shells seem to diminish the efficiency of the energy transport. This is also in agreement with decreasing fraction of quenching due to transport with increasing quenching shell thickness in Fig. 4.17(b). In fact, the thicker the quenching shell, the more molecules are said to be quenched. In addition, the regions closest to the surface exhibit the highest packing density and the steepest slope of the distribution. As a result of thicker quenching shells, the residual (non-quenching) core molecules are not only lower in absolute number, but they also have larger spacing with a lower concentration gradient. This decreases the average rate constants for energy transfer of the molecules that could theoretically take part in an energy transfer process and subsequently gives rather mono-exponential decay kinetics closer to the undisturbed molecules which is in line with Fig. 4.17(a). The simultaneous increase in immediate quenching is simply due to the increased fraction of molecules located in the quenching shell. Therefore, also the probability increases that a molecule within and not outside the quenching shell is excited. Indeed, considering Figs. 4.15 and 4.16, the quenching shell contains the majority of the molecules in a bead for thicknesses of tens of nanometers and above. In case of $\eta = 120$, more than 50 % of the molecules are located within 4 nm distance from the surface.

Based on these findings, thicker quenching shells diminish the energy transfer efficiency. Considering the previous discussion on the shape of the dye distribution, the simulations already tend to underestimate the change in decay kinetics or overestimate the overall quenching efficiency compared to experimental results. Consequently, on the one hand the quenching shell thickness d_{qs} in simulations should be rather small to not impair the deviations from experimental results. On the other hand, it should retain a physically reasonable value as it represents a finite volume that contains dye molecules. Thus, it is kept at $d_{\mathrm{qs}} = 1.4$ nm as discussed in Sec. 4.3.1.

4.3.3. Mean dye molecule distance

Regarding energy transfer, the distance between neighboring molecules is the key parameter as it determines the transfer rate in each step and the probability for multiple steps. For an energy migration process with significant range relative to the size of micron-sized beads, a sufficiently close packing of dye molecules is required.

For simulations, the bead diameter has been set to $D = 1.3$ µm and an exponent of $\eta = 120$ was used. Different values for the mean dye-dye distance correspond to changes in the dye concentration. Following the experimental determination of the effective dye loading concentration in Sec. 4.1, the mean dye-dye distance is merely a measure for the number of dye molecules per bead. In the simulations, the mean dye-dye distance sets the number of dye molecules per bead by basically using Eq. (4.3). Thus, local distances between dye molecules deviate strongly from this mean value, especially for large η. Therefore, the mean dye-dye distance is a characteristic value rather than an actual measure of distances. Variation of the mean dye-dye distance results in a change in the simulated decay kinetics as displayed in Fig. 4.18(a). With decreasing mean dye-dye distance, faster decay components gain significance. Whereas the changes progress moderately at larger dye-dye distances, they become rapid when the mean dye-dye-distances are within the order of the assumed Förster radius $R_{\mathrm{F}} = 5$ nm. The dependence of the different de-excitation pathways on the mean dye-dye distance is given in Fig. 4.18(b). First of all, the fraction of de-excitation

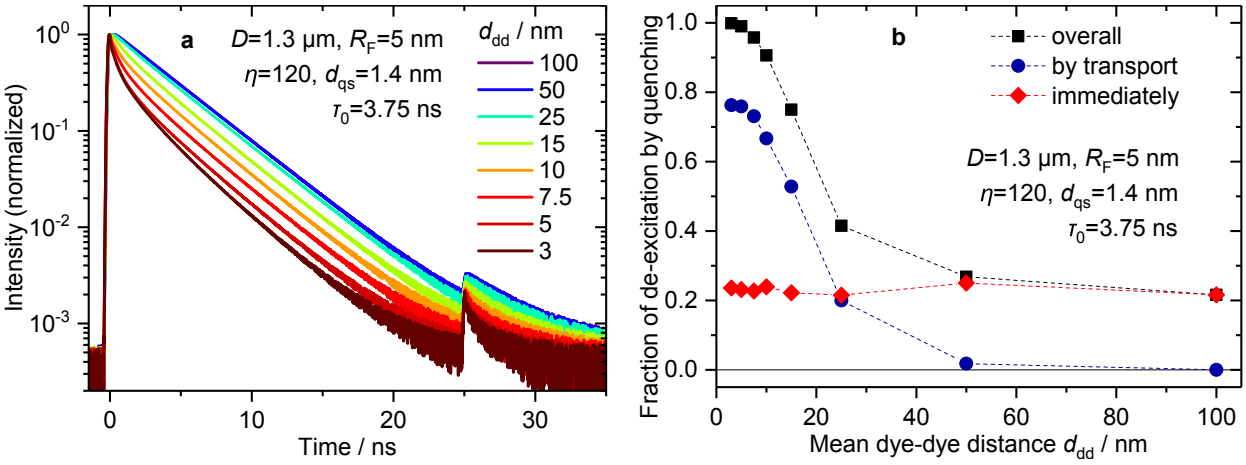

Figure 4.18: Effect of different mean dye-dye distances. (a) Simulated fluorescence decay curves. Shorter dye-dye distances affect the decay kinetics and lead to fast decay components. (b) Efficiency of the different decay pathways. The fraction of immediately quenched excitation energy is basically independent of the dye concentration whereas the transport efficiency drastically decreases with increasing molecular distances.

due to immediate quenching is virtually independent of the mean dye-dye distance. By contrast, the overall quenching efficiency decreases with increasing dye-dye distance. This is mainly due to the decrease of the transport efficiency with increasing mean dye-dye distances.

The occurrence of multi-exponential decay kinetics in Fig. 4.18(a) and the high fraction of quenching by transport in Fig. 4.18(b) indicate that energy transfer governs the decay dynamics at short mean dye-dye distances. The more pronounced multi-exponential decay at high dye concentrations is in agreement with experimental findings that were discussed before, see Fig. 4.4(b). The efficiency of the energy transfer drastically decreases with increasing mean distance between the molecules. Nevertheless, this decrease is still smaller than expected for simple FRET. There are two reasons for this. First, the multi-step energy migration helps to bridge larger distances than a single-step FRET would manage. Second, local dye-dye distances are much smaller than the mean value, so FRET can occur even when the average dye-dye distance greatly exceeds R_F. Hence, the efficiency of the transport can compete with the immediate quenching up to a mean dye-dye distance of around 25 nm. For larger dye-dye distances, the overall quenching efficiency is basically given by the fraction of molecules located in the quenching shell and most core molecules decay radiatively. At mean dye-dye distances $\gtrsim 50$ nm, the transport efficiency is virtually zero. The higher quenching efficiency, i.e. lower fluorescence quantum yield, at higher dye loading concentration agrees with experimental data, see Fig. 4.9.

The share of immediate quenching is basically independent of the mean dye-dye distance. The reason is that the relative number of molecules that are located in the quenching shell depends on the shape of the dye distribution but not on the absolute number of molecules. Consequently, the probabilities for a start of the random walk in or outside the quenching shell are independent of the mean dye-dye distance.

The mean dye-dye distance is only an estimate of the local distances between molecules. Especially for distributions with large exponents η, they vary between very large local distances at the center of the beads and much shorter distances close to the surface that may even become unphysically small. This issue is addressed in Fig. 4.19 which shows the probability of finding a certain number of neighboring molecules within a radius of 1.4 nm around randomly chosen molecule positions across the whole bead. For around half of the randomly chosen example positions, there are no

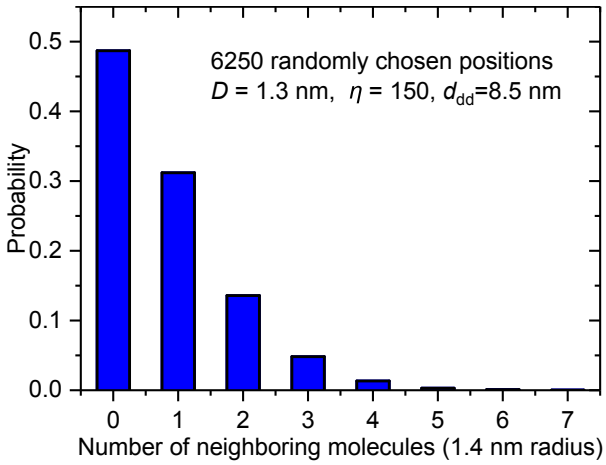

Figure 4.19: Number of neighboring molecules within a radius of 1.4 nm around randomly chosen positions from random data for a mean dye-dye-distance of 8.5 nm and an exponent η of 150. The majority of molecules have no or one neighbor within a distance of 1.4 nm. However, there are also molecules with questionably large numbers of neighboring molecules in very close proximity.

other molecules within a radius of 1.4 nm. Slightly more than 30 % of the molecules have one neighbor within 1.4 nm distance and almost 15 % have two of them. However, the situation is assumed to change with the exponent η. The results in Fig. 4.19 were generated at $\eta = 150$ and the situation is expected to be less severe for lower η. Moreover, since the assumed near-surface aggregation indeed requires high local molecule densities, local distances down to several nanometers or less might even occur in practice.

The simulations reproduce the general trend of multi-exponential decay behavior and reduced quantum yield at higher dye loading concentration observed in experimental data and support the hypothesis of energy transfer in these beads. The local distances between near-surface dye molecules can become very short. However, the majority of these closely packed molecules or aggregates have no or a reasonably low number of neighbors within critical distances.

4.3.4. Bead diameter

The bead diameter determines the surface-to-volume ratio and, for a fixed absolute thickness of the quenching shell, the volume fraction that contains quenching molecules. Moreover, it modifies the dye distribution in absolute terms. That means the typical distances of molecules to the surface depend on the bead diameter.

Upon varying the bead diameter in simulations while keeping all other parameters constant, the decay kinetics change as displayed in Fig. 4.20(a). Beads with larger diameters exhibit basically mono-exponential fluorescence decay. With decreasing diameter, short decay components gain significance and finally lead to strongly multi-exponential decay curves. The overall quenching

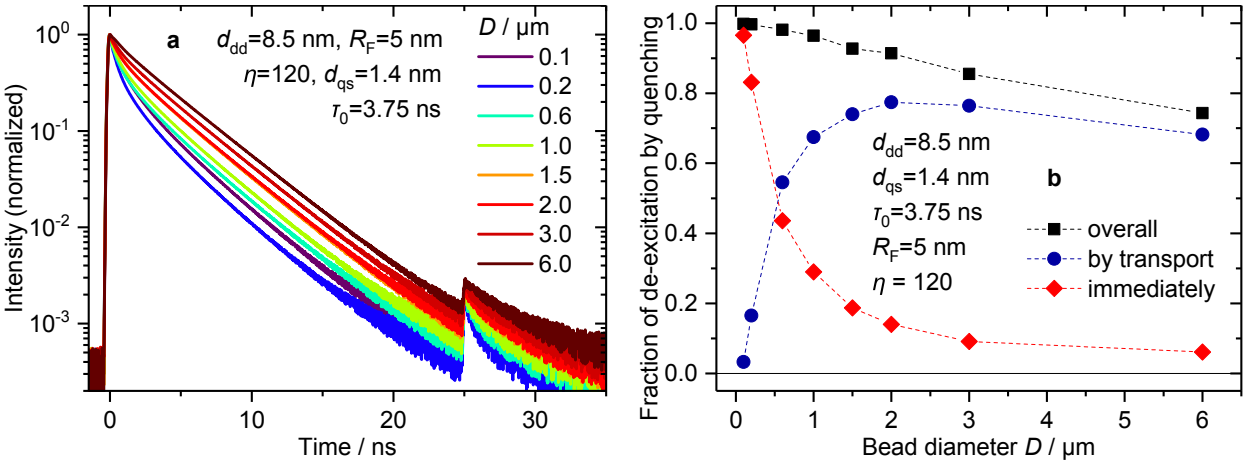

Figure 4.20: Impact of the bead diameter in random walk simulations. (a) Simulated fluorescence decay curves. Unlike larger beads, smaller beads exhibit significant impact of energy transfer and respective fast decay components. (b) Efficiency of the different decay mechanisms. Immediate quenching dominates in small beads. Quenching by transport has the highest efficiency for diameters around 2 µm.

efficiency exhibits a moderate dependence on the bead diameter whereas the shares of the individual decay pathways strongly depend on the bead diameter, see Fig. 4.20(b). The quenching efficiency for the given parameters is relatively high across the whole studied range of bead diameters. The simulations show that the immediate quenching plays an important role only in small beads. The efficiency of this quenching pathway strongly decreases with increasing bead diameter. Energy transport, in contrast, is rather insignificant in sub-micron beads and gains importance with increasing bead diameter with a maximum around a diameter of 2 µm.

The increasingly multi-exponential decay for decreasing bead diameters is in agreement with experimental data, where small beads tend to exhibit the most significant contribution of additional decay components, cf. Fig. 4.4(a). The simulations suggest that this trend would continue with decreasing diameters beyond the smallest beads studied experimentally. Apparently, the energy transport which is responsible for the variations in the decay dynamics is more efficient in smaller beads. This is due to the shorter distances of core molecules to the quenching shell at the surface. Claiming high transport efficiency, however, seems to be contradictory to the low fraction of quenching by transport for small bead diameters, see Fig. 4.20(b). In small beads, a high fraction of immediate quenching rather than energy transport is found in simulations. Since the thickness of the quenching shell was fixed to 1.4 nm, the volume fraction of this shell with respect to the overall bead varies with the bead diameter and is larger for small beads. Consequently, in small beads a larger fraction of the molecules is located in the quenching shell and is therefore immedi-

ately quenched. The transport efficiency is probably just outcompeted by the immediate quenching upon direct excitation of molecules in the quenching shell. This leads to a smaller contribution of energy transport to the overall quenching efficiency. Despite this, energy transport may still compete against radiative decay and eventually it is the balance of radiative decay and transport that determines the impact on the decay kinetics. The share of de-excitation by transport reaches a maximum for beads around 2 µm in diameter. Above this bead size, the transport efficiency decreases again as the mean distance of the core molecules to the quenching shell increases such that the probability for a radiative decay before reaching the surface is increased.

The finding of higher quenching efficiency, i.e. lower fluorescence quantum yield, with decreasing diameter complies with experimental data. However, simulation and experiment do not allow a direct comparison since the effective dye loading concentration differs from the nominal concentration depending on the bead diameter, cf. Fig. 4.1. The dye loading efficiency in intermediately sized and large beads is much lower than in small beads whereas the dye concentration for the simulations is set to the same value irrespective of the bead diameter. Therefore, fluorescence quantum yields in simulations tend to be strongly underestimated.

Even though a quantitative comparison with the experiment is hampered by the size-dependent dye incorporation efficiency, the tendency towards multi-exponential fluorescence decay and stronger quenching with decreasing bead diameter can be reproduced in the simulations.

4.4. Summary

Microbeads made of PMMA that are loaded with Rh6G exhibit an inhomogeneous dye distribution. This causes unexpected optical-spectroscopic properties that depend on the dye loading concentration and the diameter of the beads. The inhomogeneous dye distribution is presumably caused by a complexation of the stabilizer AOT and the dye Rh6G. During synthesis, the stabilizers PVP and AOT seem to form a shell around each bead yielding an AOT-Rh6G layer. This shell possibly has a high local dye concentration that enhances aggregation. Consequently, the dye molecules not only exist as fluorescent monomers in the core of the beads but also form aggregates depending on the dye concentration. The aggregates are preferentially located near the surface due to the higher dye concentration caused by the complexation. Moreover, near-surface monomers are exposed to water that penetrates the near-surface regions of the beads which changes the fluorescence characteristics compared to the core monomers. In addition, the interaction between AOT and Rh6G might cause a concentration gradient across the whole bead with higher dye concentration close to the surface.

The near-surface monomers introduce slower decay components to the overall fluorescence decay kinetics. Moreover, their fluorescence excitation spectra are blueshifted with respect to the core monomers. The near-surface aggregates reduce the overall quantum yield. At sufficiently high dye loading concentrations, the intermolecular distances become short enough to allow energy migration by FRET. This energy migration process transports excitation energy from the core monomers to the near-surface aggregates. The energy transfer to the near-surface aggregates adds additional fast decay components to the fluorescence decay kinetics. Furthermore, it reduces the observed fluorescence anisotropy.

A random walk algorithm was developed to simulate energy migration by Förster resonant energy transfer in the dye-loaded beads to verify the experiment-based hypothesis. The random walk model includes straightforward dye distributions with radially increasing dye concentration. The radial concentration gradient causes directed energy transport towards the shell of quenched near-surface aggregates. The simulations qualitatively reproduce the experimental findings, thereby supporting the supposed explanation.

5. Luminescence lifetime encoding in flow cytometry

Encoding strategies are employed for many analytical purposes, e.g. in bead-based assays or for the determination of specific properties of cells. To this end, analytes or cell populations are specifically labeled, or encoded beads are used that bind certain analytes. These labels and codes are often fluorescence-based and rely on the readout of spectral characteristics, intensities, or properties of scattered light. Measurements of luminescence decay kinetics in time-domain flow cytometry are meant to increase the information density obtained from such experiments and could enable novel analytical and scientific applications. In flow cytometry, the beads or cells are measured one by one and the respective labels of the cells or codes of the beads are detected for each object. Frequency-domain techniques have already been tested and approved for flow cytometry [18]. However, time-domain methods could be advantageous at lower signal intensities and for more straightforward data analysis. Yet there seems to be a lack of systematic studies on time-domain methods. For lifetime encoding, the goal is to optimize the possible discrimination between codes. Correct determination of the lifetimes of the encoding luminophores is not necessarily needed.

The lifetime flow cytometry (LT-FCM) prototype device from `Quantum Analysis GmbH` was briefly described in Sec. 3.4. This prototype device was assessed and optimized in terms of encoding capabilities [53] and combination with spectral encoding. The assessment encompassed time resolution, uncertainty of obtained lifetime values, reproducibility, and stability in dependence of measurement and data analysis parameters as well as overall measurement conditions. Additionally, simulated decay curves were used to understand and unravel superimposed effects, such as the impact of the collected photon counts and the signal-to-background ratio. The insights from these investigations were used to optimize the system and maximize the number of distinguishable codes. Moreover, the results can be used for further technical development in fast luminescence lifetime detection.

Luminophore-loaded polymer microbeads were used as model lifetime-encoded objects. The samples are described in the following section. Thereafter, a brief outline of the applied numerical simulations will be given. Subsequently, these simulations are employed in combination with experiments to assess the capabilities of the LT-FCM prototype. Finally, the achievable degree of multiplexing with this system and possible applications are discussed.

Parts of this chapter are based on Ref. [53].

5.1. Characterization of suitable lifetime-encoded luminophore systems

Polymer microbeads containing luminophores were used as lifetime-encoded model systems. A total of five lifetime codes were chosen, four of them using organic dyes and one based on semiconductor quantum dots (QDs). The five codes with their respective luminophores and mean bead diameter are listed in Tab. 5.1. Beads containing organic dyes (codes A-D) were synthesized and supplied by

LT code	Luminophore	Diameter / µm	λ_{ex} / nm	λ_{det} / nm	τ / ns
A	Red5 400	6.5	488	645 LP	1.72
B	Red/Red5 100/300	6.3	488	645 LP	2.71
C	Red 50 (400†)	9 (6.9†)	488	590 LP	5.54
D	Pink 400	6.8	488	645 LP	7.91
E	CdSe/CdS/ZnS QDs	6.2 ± 0.6	488 (425†)	645 LP	22.6

Table 5.1: Lifetime codes and respective luminophores with measurement parameters and obtained ensemble (reference) lifetimes calculated as intensity-weighted mean lifetimes from multi-exponential decay fits. Code B is a mixture of codes A and C.
† for steady-state spectroscopy

`PolyAn GmbH`. Beads containing quantum dots (code E) were provided by the `LRN (University of Reims Champagne Ardenne)` [86].

Ensembles of the beads in water were characterized by steady-state and time-resolved spectroscopy to have a basis and reference for the evaluation of the results from LT-FCM. The photoluminescence emission spectra of the lifetime code ensembles are displayed in Fig. 5.1(a). All samples except for code E were excited at 488 nm for comparability with LT-FCM measurements. Table 5.1

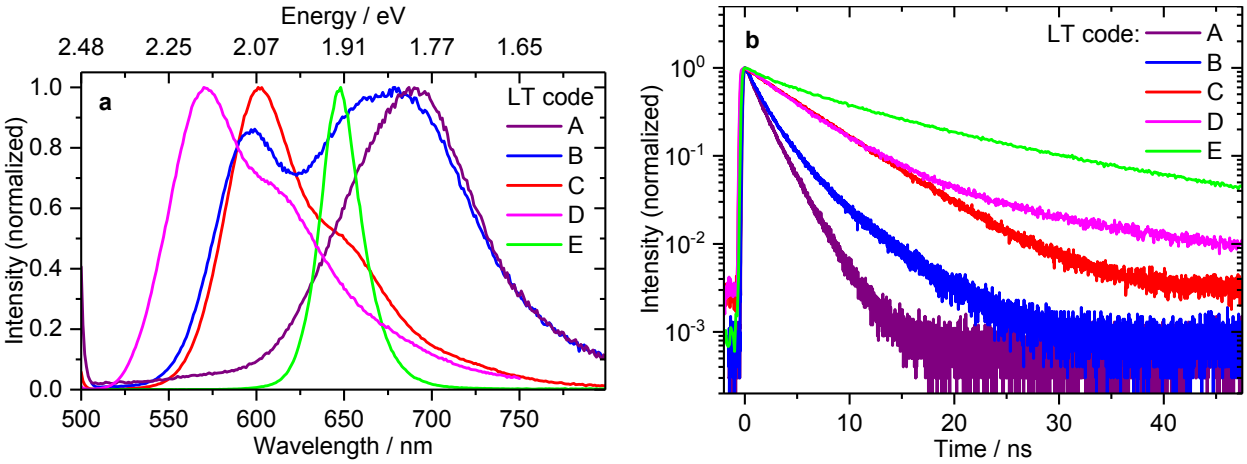

Figure 5.1: Optical spectroscopy on lifetime-encode bead ensembles. (a) Photoluminescence emission spectra. The lifetime codes could all be read within a common wavelength region though they differ in spectral properties. (b) Photoluminescence decay curves. The luminescence decays show significant differences as required for lifetime encoding.
Previously published, reproduced from Ref. [53] (`https://creativecommons.org/licenses/by/4.0/`).

summarizes the measurement conditions and lists the characteristics of the lifetime-encoded model systems. The total emission range of all codes extends from around 525 to more than 800 nm. All codes show significant signal intensity in the spectral range starting from 630 nm as required for application in our LT-FCM. Photoluminescence decay curves of the codes from ensemble measurements are shown in Fig. 5.1(b). Detection was carried out with a 590 nm (code C, for intensity reasons only) or 645 nm (all others) longpass filter and the monochromator set to zeroth diffraction order. Obviously, the decay kinetics differ significantly and should therefore be distinguishable in LT-FCM. The luminescence lifetimes were determined by least-squares curve fitting of multi-exponential decay functions to the data and are listed in Tab. 5.1.

5.2. Simulated decay curves and lifetime determination

Synthetic data permit the examination of the impact of certain parameters or conditions in isolation. The first step is the generation of an artificial intensity decay curve following the desired probability distribution, e.g. a mono- or multi-exponential decay

$$I(t) = \sum_j A_j \mathrm{e}^{-\frac{t}{\tau_j}} ,$$

where A_j and τ_j are the amplitude and lifetime of each exponential component. Photon arrival times are obtained by mapping uniformly distributed pseudo-random numbers onto a distribution according to the required decay function. This procedure is described in Sec. A.4. In photon counting techniques, a photoluminescence decay curve is basically a histogram of such arrival times, see Sec. 3.2.2. Thus, the randomly generated arrival times are binned with a set bin width. The number of arrival times represents the number of photons collected in an experiment. The same procedure is carried out for noise, though the noise counts are uniformly distributed. The resulting histogram is an artificial decay curve.

To mimic LT-FCM measurements, an appropriate number of decay curves is generated using identical parameters and a lifetime is calculated for each curve. Each simulated curve corresponds to one object measured in LT-FCM. Usually, 1000 repetitions, each generating an individual decay curve, were performed per parameter set if not stated otherwise. Mean values and standard deviations of calculated lifetimes are obtained from the repetitions. The standard deviations of the obtained lifetimes represents the width of the respective lifetime distribution.

From a decay curve (artificial or experimental), the mean lifetime is calculated through an adapted version of Eq. (2.4):

$$\begin{aligned} \tau_{\mathrm{mean}} &= \frac{\int_0^\theta t I(t) \mathrm{d}t}{\int_0^\theta I(t)\,\mathrm{d}t} \\ &\approx \frac{\sum_{j=1}^{j_{\max}} t_j I_j}{\sum_{j=1}^{j_{\max}} I_j} \end{aligned} \tag{5.1}$$

with the integration time range θ of choice and time bin indices j. Lifetime determination with Eq. (5.1) was chosen for its robustness and straightforward application.

5.3. Assessment of instrument capabilities and data analysis

The measurement time for a single object in LT-FCM is limited by the interaction time with the excitation laser spot. The situation is illustrated in Fig. 5.2. During the transit time of several

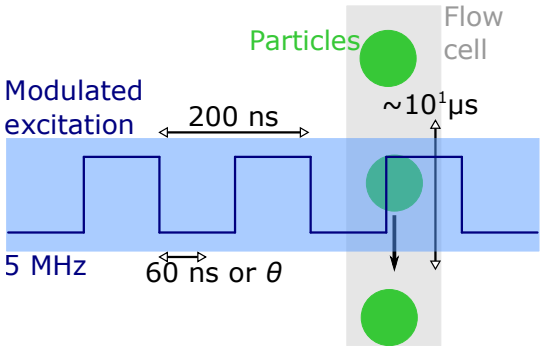

Figure 5.2: Schematic drawing of the interaction of an object with the laser spot in a flow cytometer. For LT-FCM, the excitation is modulated with a 5 MHz square wave. For an interaction time of 50 µs, a particle encounters around 250 excitation cycles.

tens of microseconds of a particle through the laser spot, the particle experiences multiple cycles of the modulated excitation light. In our LT-FCM prototype, the repetition rate is 5 MHz, which results in around 250 excitation cycles for a transit time of 50 µs. Following every excitation pulse, there is a maximum time range of 60 ns for luminescence photon detection. This time range θ can be further limited during data analysis, cf. Eq. (5.1). For each particle, a luminescence decay curve must be measured within the limited transit time.

Measurements performed with LT-FCM yield much lower numbers of photons per decay curve than the ensemble measurements shown in Fig. 5.1. This is demonstrated in Fig. 5.3(a) with the example of decay curves of single beads of all five codes considered for LT-FCM. These decay curves are based on only several hundreds instead of millions of counts as in the ensemble measurements in Fig. 5.1(b). Moreover, the signal-to-background ratio (SBR) is apparently much smaller in LT-FCM than for ensemble TCSPC. Also the coarse time binning, and consequently the time resolution, as well as the simple lifetime calculation with Eq. (5.1) are expected to have an impact on lifetime code distinction. The main outcome of an LT-FCM measurement is the lifetime distribution of the measured objects. This means that a lifetime is deduced from every single-particle decay curve by means of Eq. (5.1) and all lifetime values are binned to produce a histogram. Figure 5.3(b) displays representative lifetime distributions obtained from decay curves with low photon count numbers measured with the LT-FCM setup. The precision of a measurement is characterized by the width of the distribution, i.e. the standard deviation of the single values. The standard deviation also determines how well the individual codes can be distinguished. Along with the measured distributions of the bead samples, Fig. 5.3(b) also displays simulated lifetime distributions. It shows that lifetime distributions obtained from synthetic data sets can mimic those measured with the LT-FCM prototype. Thus, the synthetic data are considered suitable for the theoretical assessment of specific combinations of measurement conditions and parameters.

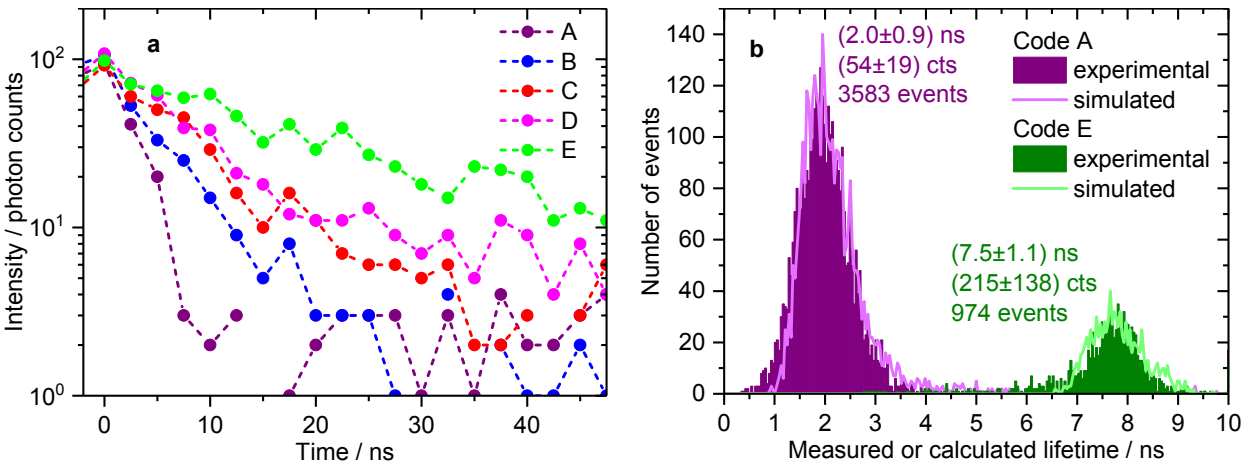

Figure 5.3: (a) Typical photoluminescence decay curves of single beads obtained with the LT-FCM setup. Compared to the decay curves of ensembles in Fig. 5.1(b) the number of counts is drastically decreased, which makes the lifetime determination challenging. (b) Comparison of measured and simulated distributions of lifetimes. The measured and simulated lifetime distributions show good agreement.

The term 'lifetime' will be used in various ways and it is necessary to consistently differentiate between them. Lifetimes obtained from ensemble measurements are called 'reference lifetimes' τ_{ref}, values used as input for simulations are 'notional lifetimes' τ_{not}, and those resulting from the simulations are denoted 'calculated lifetimes' τ_{cal}. Finally, values deduced from LT-FCM data are referred to as 'measured lifetimes'.

As pointed out by Fig. 5.3, distinction of beads based on their lifetime faces issues due to low photon count numbers, low *SBR*, and coarse time binning. Thus, we systematically investigated the impact of these parameters and conditions on the lifetimes measured in LT-FCM using simulations and experimental data.

5.3.1. Photon count number

The number of photons collected per object is crucial to the lifetime measurement within the short illumination time in flow cytometry. We simulated exponential decay curves with defined numbers of photon counts to study the theoretically obtainable mean value and the standard deviation of lifetime distributions in dependence of the count number. Simulated decay curves have the advantage over experimental data that they allow an isolated investigation without other influences such as background counts. For these simulated decay curves, a small bin width of 10 ps was chosen to avoid additional distortions and background was omitted.

The simulation results for mono-exponential decay are shown in Fig. 5.4(a). Within a range of 1 to 1000 photons per decay curve, the mean calculated lifetime stays constant, even down to a single photon per decay curve. The standard deviation and thereby the width of the lifetime distributions, however, drastically increases with decreasing number of counts. Thus, lifetime determination stays

accurate on average down to very low count numbers but suffers from broad distributions and therefore low precision. The lifetimes were calculated from the simulated decay curves by means of

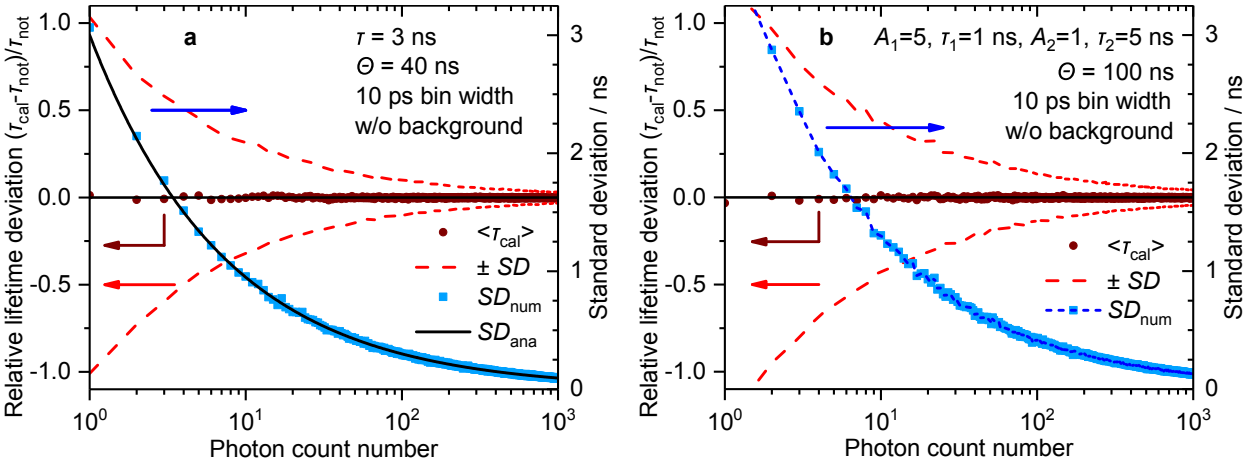

Figure 5.4: Simulated dependence of the relative deviation between calculated and notional lifetime and standard deviation on the photon count number. (a) Mono-exponential decay: The relative deviation is independent of the photon count number. The standard deviation decreases with increasing number of collected photons and follows Eq. (A.6). (b) Bi-exponential decay: The relative deviation is independent of the photon count number and the standard deviation decreases with increasing number of acquired photons.
(a) Previously published, reproduced from Ref. [53] (`https://creativecommons.org/licenses/by/4.0/`).

Eq. (5.1) which is a rather simplistic method. Thus, we compared the standard deviation calculated this way from the numerical results, SD_{num}, with an analytical expression of the standard deviation expected for least-squares curve fitting, SD_{ana}, Eq. (A.6) [87, 88]. The two respective graphs in Fig. 5.4(a) show perfect agreement. This means that, under the given circumstances, the simple and fast lifetime calculation based on Eq. (5.1) can compete with sophisticated curve fitting.

Luminophores employed as lifetime codes may not necessarily exhibit mono-exponential luminescence decay. Thus, to also consider multi-exponential decays, Fig. 5.4(b) shows the results of a simulation for bi-exponential decay with the same intensity-weighted mean lifetime as the mono-exponential decay studied before. Again, the mean value of the calculated lifetimes stays constant down to a single photon per decay curve. The standard deviation exhibits a dependence on the count number that is comparable to the case of mono-exponential decay, though the increase of the standard deviation with decreasing count number is steeper. This leads to broader distributions. However, as the mean value of the calculated lifetime is independent of the number of counts also in bi-exponential decay, we have evidence that luminophore systems applicable to lifetime encoding are not limited to those with mono-exponential decay kinetics.

Overall, a low number of detected photons introduces significant uncertainty, but no systematic deviation of the mean value. The standard deviation is around 1 ns for a mono-exponential decay with only 10 photon counts per decay curve. With 200 counts, the deviation theoretically reduces to 0.2 ns. For lifetime codes with multi-exponential decay, more photons are required. Namely, for the example of bi-exponential decay, twice as many photons are required for comparable precision.

5.3.2. Signal-to-background ratio

Background signal, whether it be electronic background or stray light reaching the detector, is present in every measurement and gains importance for low signal intensities. Lifetime measurements with analysis based on Eq. (5.1) are not background-corrected. The relevance of background counts for the data obtained with LT-FCM is demonstrated by the single-particle decay curves in Fig. 5.3(a). Thus, it is important to estimate the impact of possible background signal on the measured lifetimes. To that end, synthetic decay curves with a defined fraction of background counts were generated. We define the signal-to-background ratio as

$$SBR = \frac{integrated\ number\ of\ signal\ counts}{integrated\ number\ of\ background\ counts}\,. \tag{5.2}$$

Calculated lifetimes and standard deviations, SD_{num}, from simulations are shown as functions of the SBR in Fig. 5.5. A mono-exponential decay function with $\tau = 3$ ns was used in the simulations, each decay curve consisted of 100 counts. For a good, i.e. high, SBR, the calculated

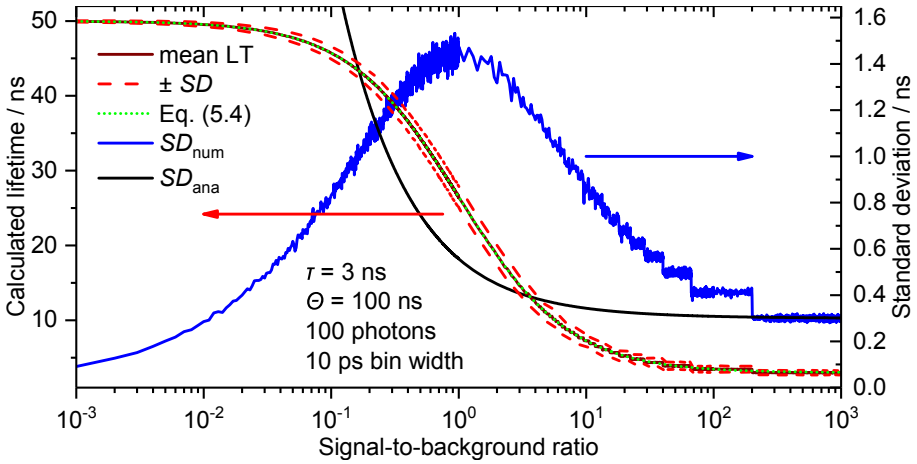

Figure 5.5: Simulated influence of the signal-to-background ratio on the calculated lifetime. The lifetime determination will be erroneous at low SBR as the calculated lifetime approaches $\theta/2$. The distribution width shows a maximum for SBR= 1. Thus, LT-FCM measurements at low SBR may exhibit narrow distributions but the mean value can be misleading. The analytical standard deviation SD_{ana} expected for curve fitting is given by Eq. (A.7). It would be superior to Eq. (5.1) for certain values of SBR.
Previously published, adapted from Ref. [53] (`https://creativecommons.org/licenses/by/4.0/`).

lifetime equals the notional lifetime. With decreasing SBR, we observe an increase of the calculated lifetime and it levels off for $SBR \to 0$. The strongest variation of the calculated lifetime occurs around $SBR = 1$, i.e. for an equal number of signal and background counts. The calculated standard deviation, SD_{num}, increases with decreasing SBR, reaches a maximum at $SBR = 1$, and decreases again with further decreasing SBR. The standard deviation reflects the width of a measured lifetime distribution and thus the precision of a measurement.

The dependence of the calculated lifetime values on the SBR can be explained as follows. Considering a mono-exponential decay with a constant background parameter, $Ae^{-t/\tau} + B$, and assuming

such a decay behavior in Eq. (5.1), one finds

$$\begin{aligned}\tau_{\text{mean,bg}} &= \frac{\int_0^\theta t\left(A\mathrm{e}^{-\frac{t}{\tau}}+B\right)\mathrm{d}t}{\int_0^\theta \left(A\mathrm{e}^{-\frac{t}{\tau}}+B\right)\mathrm{d}t} \\ &= \frac{A\tau\left(\tau-[\tau+\theta]\mathrm{e}^{-\frac{\theta}{\tau}}\right)+\frac{B}{2}\theta^2}{A\tau\left(1-\mathrm{e}^{-\frac{\theta}{\tau}}\right)+B\theta}\,. \end{aligned} \tag{5.3}$$

For better comparability to former discussions and experimental data, however, A and B should be replaced by the *SBR*. The relation between the parameters A and B in the mono-exponential decay and the *SBR* defined in Eq. (5.2) is

$$\frac{A}{B} = \frac{\theta}{\tau\left(1-\mathrm{e}^{-\frac{\theta}{\tau}}\right)}\cdot SBR$$

and the expected lifetime, Eq. (5.3), becomes

$$\tau_{\text{mean,bg}} = \frac{\frac{SBR}{1-\mathrm{e}^{-\frac{\theta}{\tau}}}\left(\tau-[\tau+\theta]\mathrm{e}^{-\frac{\theta}{\tau}}\right)+\frac{\theta}{2}}{SBR+1} \tag{5.4}$$

for $B > 0$. Equation (5.4) is plotted along with the simulated behavior in Fig. 5.5 (green dotted line) and both curves show perfect agreement. Also, considering very weak signal or high background intensity, i.e.

$$\lim_{SBR\to 0}\tau_{\text{mean,bg}} = \frac{\theta}{2}\,,$$

the calculated lifetime is expected to approach a value that is independent of the notional lifetime and only given by the time range θ. The simulation shows exactly the same finding: the calculated lifetime reaches 50 ns at very low *SBR* for $\theta = 100$ ns. This behavior is caused by the homogeneous distribution of background counts over the whole time range and will also be discussed in the following section. Despite the significant deviation from the real lifetime, the standard deviation decreases again at lower *SBR*. Consequently, the results at $SBR \ll 1$ appear as being very precise while actually being erroneous.

Figure 5.5 also shows a graph of the analytical expression for the standard deviation expected from curve fittings, SD_{ana}, Eq. (A.7) [87]. In contrast to the case without background counts displayed in Fig. 5.4, the numerically determined standard deviation from simulations and the analytical result show different behavior. For values of the *SBR* larger than $\approx 2\cdot 10^{-1}$, curve fitting is expected to result in lower deviations than lifetime determination by means of Eq. (5.1).

In summary, the ratio of signal and background intensity has a strong influence on the calculated lifetimes. Compared to the case without background, Fig. 5.4(a), the presence of background counts adds significant uncertainty already for an *SBR* on the order of 10^2. Considering the data for code B in Fig. 5.3(a), the background can be estimated with 2 counts per bin and the overall number of counts amounts to slightly below 300 within the full 60 ns. Thus, the estimated *SBR* is

around 5 and would consequently introduce both systematic deviation of the mean lifetime value and drastically increased standard deviation. The relative deviation from the reference lifetime due to the background would be around 250 %, and the standard deviation larger than 1 ns. Moreover, a low SBR not only results in systematic deviations of the calculated lifetimes from the notional lifetimes. It also gives the misleading impression of increasing precision with decreasing SBR for $SBR < 1$ as the standard deviation decreases again. Therefore, the SBR seems to be even more critical to lifetime determination or encoding than the actual number of photon counts.

5.3.3. Time range

Experimental data sets are naturally limited to a finite time range. This was already indicated by the upper integration limit θ in Eq. (5.1). Practically, the time range θ determines for how long after the end of the excitation pulse possible photon counts are considered. It may be either given by technical limitations as it cannot be longer than the time between two excitation pulses (cf. Fig. 5.2) or it can be set during analysis.

We therefore studied the impact of a limited time range on the measured lifetimes of the five codes obtained with the LT-FCM setup. The mean values of measured lifetimes for varying θ are displayed in Fig. 5.6(a), the error bars indicate the standard deviations of the respective distributions. The data points indicate a continuous increase of the measured lifetimes with increasing

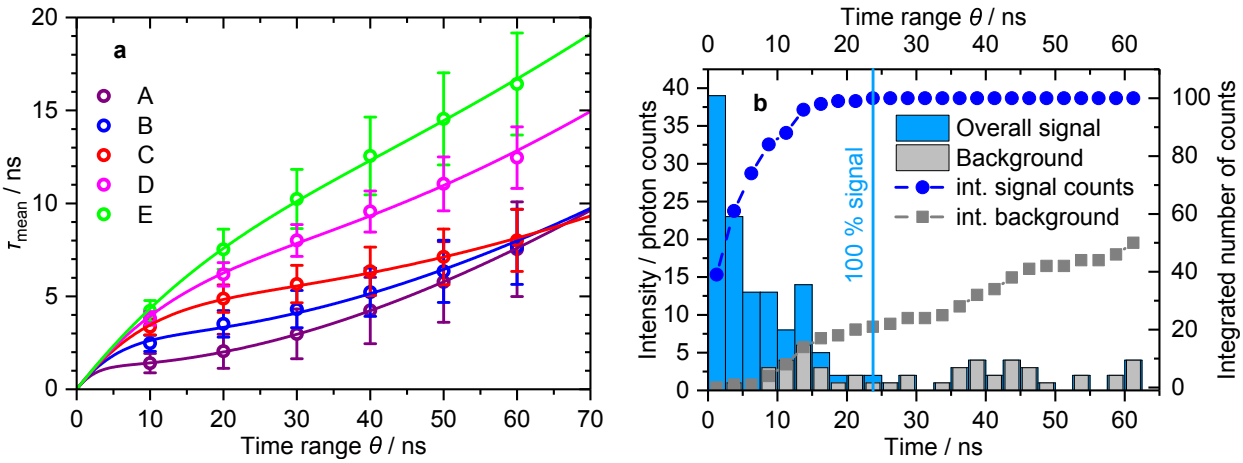

Figure 5.6: Influence of the integration time range θ. (a) Dependence of the measured lifetime on θ. Symbols represent data from experiments, solid lines are fits of Eq. (5.3) to the data. The error bars represent the standard deviations of the respective lifetime distributions. The measured lifetimes vary with the chosen time range. However, the time range can also be used to optimize the discrimination of the codes. (b) Simulated decay curves and integrated count numbers for signal and background illustrating the interplay of background counts and time range.
(a) Previously published, reproduced from Ref. [53] (`https://creativecommons.org/licenses/by/4.0/`).

time range θ. The slope is generally steeper for those lifetime codes that have the longer reference lifetimes. Thus, the time range determines how well different lifetime codes can be separated. The

three codes with the shortest lifetimes exhibit a point of intersection at around 60 ns. Moreover, for short time ranges, all measured lifetimes approach zero.

Assuming a mono-exponential decay, Eq. (5.1) yields

$$\begin{aligned}\tau_{\text{mean}} &= \frac{\int_0^\theta t\mathrm{e}^{-\frac{t}{\tau}}\mathrm{d}t}{\int_0^\theta \mathrm{e}^{-\frac{t}{\tau}}} \\ &= \tau - \frac{\theta}{\mathrm{e}^{\frac{\theta}{\tau}}-1}\,.\end{aligned} \tag{5.5}$$

The derivative of Eq. (5.5) with respect to θ (not shown) indicates steeper slopes with increasing reference lifetime in agreement with Fig. 5.6(a). Considering the limit $\theta \to 0$, one finds

$$\begin{aligned}\lim_{\theta\to 0}\tau_{\text{mean}} &= \lim_{\theta\to 0}\left(\tau - \frac{\theta}{\mathrm{e}^{\frac{\theta}{\tau}}-1}\right) \\ &= \tau - \lim_{\theta\to 0}\frac{\theta}{\mathrm{e}^{\frac{\theta}{\tau}}-1} = \tau - \lim_{\theta\to 0}\frac{1}{\frac{1}{\tau}\mathrm{e}^{\frac{\theta}{\tau}}} \\ &= \tau - \tau\lim_{\theta\to 0}\frac{1}{\mathrm{e}^{\frac{\theta}{\tau}}} = \tau - \tau = 0\end{aligned}$$

which describes the observed convergence to zero for all lifetime codes for short θ. For $\theta \to \infty$,

$$\lim_{\theta\to\infty}\tau_{\text{mean}} = \tau$$

which tells us that the measured values should approach the reference values, and therewith the correct lifetimes, for large θ. Such a behavior is not observed in the measured data, cf. Fig. 5.6(a). Rather, a steady increase with varying slope is present. Moreover, Eq. (5.5) does not cover the collapsing of the three shortest codes for $\theta \approx 60$ ns. In Sec. 5.3.2 we have seen that the ratio of signal and background is relevant to the obtained lifetime values. Consequently, a constant offset B representing background with respect to the decay amplitude A is introduced. The modified relation was already given in Eq. (5.3) and reads

$$\tau_{\text{mean,bg}} = \frac{A\tau\left(\tau - [\tau+\theta]\mathrm{e}^{-\frac{\theta}{\tau}}\right) + \frac{B}{2}\theta^2}{A\tau\left(1-\mathrm{e}^{-\frac{\theta}{\tau}}\right) + B\theta}\,. \tag{5.3}$$

In the range of small θ, the impact of the background parameter B is small and Eq. (5.3) could still be approximated by Eq. (5.5). However, when $\theta \gg \tau$, the number of background counts within the time range θ steadily increases which in turn increases the obtained lifetime values with increasing θ. Fits of Eq. (5.3) to the data in Fig. 5.6(a) (solid lines) show perfect agreement with the course of the data points. Even though Eq. (5.3) is based on the assumption of a mono-exponential decay which oversimplifies the actual decay kinetics [cf. Fig. 5.1(b)] it clearly reproduces the intersection point of the three shortest codes. Despite this, the values of τ obtained as fit parameters [A: 1.25(9) ns, B: 2.8(1) ns, C: 4.9(1) ns, D: 7.1(2) ns, E: 11.1(8) ns] which should

resemble the reference lifetimes (Tab. 5.1) are systematically too small. This underestimation of the lifetimes could be due to the relatively coarse bin width of 2.5 ns or the simplifying assumption of mono-exponential decays. The slight indication of a flattening of the curves around 20 to 30 ns for the shorter codes is caused by a trade-off between approaching the reference lifetime with longer θ and the continuously increasing values caused by the accumulation of background counts.

The way background counts influence the lifetime determination is also exemplified by Fig. 5.6(b). The bars show a simulated decay curve ($\tau = 5$ ns, 100 counts) and background signal ($SBR = 2$). Additionally, the integrated count numbers for only signal counts and only background counts in dependence on the time range θ are displayed. When θ exceeds 22.5 ns (vertical blue line), all of the acquired signal counts are incorporated into the calculation. Thus, further increasing θ does not provide any further information about the actual decay. It only increases the number of background counts that are detrimental to the lifetime determination. The background counts increase the obtained lifetime values with increasing time range.

Altogether, a finite time range for lifetime determination causes significant deviations from the actual lifetime that depend on the reference lifetimes. On the one hand, too short a time range results in shortened measured lifetimes with respect to the reference lifetimes. On the other hand, too long a time range can lead to longer measured lifetimes due to possible background signal. The actual effects on the measured lifetimes depend on the sample under investigation and the *SBR*. Thus, the optimum value of θ should be individually determined for each measurement task. However, the adaption of the time range to a certain set of lifetime codes can also be used to improve the distinguishing capabilities and to avoid overlap of codes by limiting the influence of the background signal. Ultimately, the separation of codes is more important than the correct determination of the encoding luminophore lifetime.

5.3.4. Bin width

The precision of arrival time measurements in the custom-built LT-FCM is limited by the time bin width of 2.5 ns. This value also determines the lower limit of the data bin width. To evaluate the effect of such coarse binning, synthetic decay curves with different notional lifetimes were generated. Each simulated decay curve consisted of 1000 counts, the integration time range was set to $\theta = 100$ ns, and zero background counts were assumed. The time values assigned to bins are the lower bounds of the bins. Thus, the first bin has $t = 0$ ns.

The relative deviation of the mean calculated lifetimes from the notional lifetimes obtained in simulations with respect to the bin width is shown in Fig. 5.7(a). Calculated lifetimes are always shorter than their respective notional lifetimes. The deviation is stronger the wider the bins are and the shorter the notional lifetimes are. The latter is also illustrated by the simulation results in Fig. 5.7(b) for a fixed bin width of 2.5 ns, which corresponds to the smallest technically possible bin width of the LT-FCM setup. For intermediate lifetimes, the relative deviation may easily exceed 30 % when using 2.5 ns bins, in case of short lifetimes it approaches almost 100 %. Thus, the bin width is critical for an accurate lifetime measurement. Moreover, it introduces systematic errors that depend on the actual lifetime of a certain code.

The dependence of the calculated lifetime on the bin width could also explain the underestimation of the lifetimes obtained as fit parameters when applying Eq. (5.3) to the data in Fig. 5.6(a):

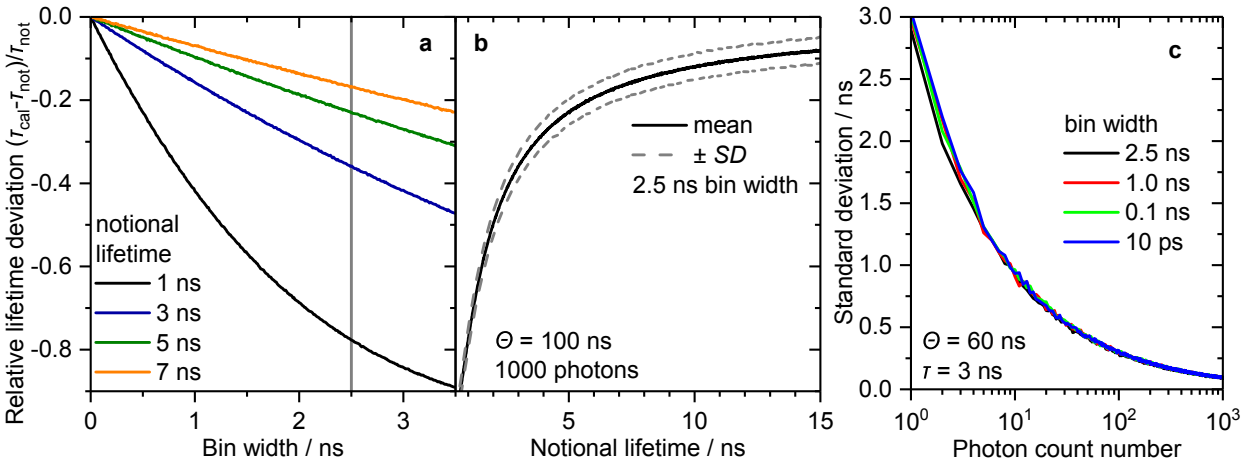

Figure 5.7: Simulated impact of the bin width on calculated lifetimes. (a) Dependence of the relative deviation between calculated and notional lifetime on the bin width for different notional lifetimes. The larger the bin width, the more severe the deviation. Short lifetimes are affected more strongly. (b) Calculated lifetime in dependence on the notional lifetime for 2.5 ns bins as used in the prototypical LT-FCM. (c) Dependence of the standard deviations of simulated lifetime distributions on the number of acquired photons and the bin width. The bin width does not influence the distribution width.
Previously published, adapted from Ref. [53] (`https://creativecommons.org/licenses/by/4.0/`).

the measured lifetimes are based on binned counts and therefore tend to be shorter than the reference lifetimes. Equation (5.3), however, uses an integral representation without binning. This discrepancy leads to shorter lifetime parameters in the fits.

The simulated standard deviation, i.e. the width of the distribution of calculated lifetimes, turned out to be independent of the bin width, see Fig. 5.7(c). That means, the width of a distribution is not expected to change when a sample is analyzed at different bin widths.

Obviously, coarse data binning introduces systematic errors in lifetime determination. In addition, it affects short notional lifetimes stronger than long ones. Consequently, differences in measured lifetimes may become larger than the respective differences in the reference values. For code A (1.72 ns), the shortest code in the test set, the measured lifetime would be reduced by more than 50 % with respect to the reference lifetime. Code D would be subject to around 15 % deviation whereas for code E the deviation decreases well below 10 %.

5.3.5. Detector operating range

On the one hand, a large number of detected photons decreases the standard deviation of calculated lifetimes as discussed in Sec. 5.3.1. A decreased standard deviation is obviously beneficial for a more precise lifetime determination. On the other hand, the detector dead time limits the acceptable signal rate and thus the count number within a given time window. The response of our LT-FCM detection system to varying rates of impinging photons was tested using neutral density filters while keeping all other parameters constant.

Exemplarily, distributions of measured lifetimes obtained with our LT-FCM setup for code B with different filter transmittance are given in Fig. 5.8(a). We observe a shift of the distributions of

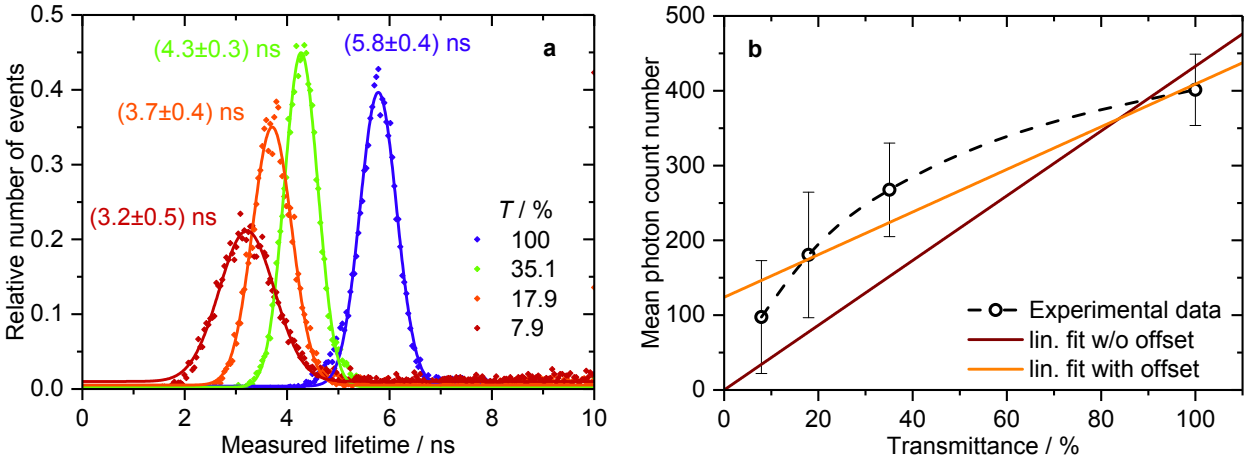

Figure 5.8: Response of the detection system of the LT-FCM to different signal rates. (a) Distributions of measured lifetimes of code B at different transmittance values. The solid curves are Gaussian fits to the data and serve as guides to the eye. The measured lifetime depends on the rate of impinging photons. (b) Number of detected photons as a function of the filter transmittance. The deviation from a linear correlation indicates that the detector is operated beyond the linear range.
Previously published, adapted from Ref. [53] (`https://creativecommons.org/licenses/by/4.0/`).

the measured lifetimes towards longer lifetimes with increasing filter transmission and therefore increasing number of counts. Also, a minor decrease of the width of the distributions occurs. Since the observed shifts of the distribution (> 2.5 ns) are much larger than the FWHMs (≈ 1 ns) and the differences between some reference lifetimes ($\approx$ 1–5 ns), the shifts constitute a severe distortion in the lifetime determination.

As the preceding discussion in Sec. 5.3.1 has shown, the number of acquired photon counts should alter the distribution width but the mean value of the lifetime distribution should stay unaffected. Thus, the varying number of photons alone does not explain the observed behavior from a theoretical point of view. Changing the amount of light impinging on the detector by using filters of different transmittance could also have an impact on the *SBR*. A decreasing *SBR* might cause a shift to higher lifetime values, cf. Sec. 5.3.2. However, an increasing signal intensity was rather expected to improve the *SBR*. Hence, also a possible change of the *SBR* does not provide a satisfactory explanation.

Presumably, the shift of the distributions is due to an issue of the detection system. Assuming an already quite long interaction time with the laser spot of 50 µs would mean 250 laser pulses per object. The technically determined time range following a pulse is 60 ns long. Thus, the total time for photon detection sums up to 15 µs per object. If 500 photons per particle were collected, the average time between two photons impinging on the detector would be 30 ns (disregarding detector efficiency). The emission intensity drastically changes during the course of the luminescence decay and the peak intensity immediately after the end of the excitation pulse might easily be orders of

magnitude higher than the average intensity. Thus, even though the overall number of collected photons is relatively low, high fluxes occur within short time intervals. The detector is not capable of separating and detecting all photons and therefore omits part of the signal. This causes detector saturation and consequently only a smaller fraction of the impinging photons can be detected. As a result, the detection efficiency at longer delays after the pulse appears to be higher than immediately after the end of the pulse since the signal intensity is lower and the fraction of impinging photons that are detected is higher. This gives rise to a disproportional accumulation of counts at longer delays and therefore seemingly longer lifetimes.

As a support to the assumption of too high signal intensity, Fig. 5.8(b) shows the number of detected photons as a function of the filter transmittance. If the detector was operated within the linear range, the dependence of the number of photons on the filter transmittance should be linear and follow either the linear function without offset (disregarding background) or with offset (assuming electronic background independent of the signal intensity). The data points clearly indicate that the dependence is non-linear and the measured intensity levels off with increasing transmittance.

The issue of detector saturation while only accumulating several hundreds of photon counts illustrates the bottleneck of lifetime determination in flow. A trade-off must be made between acceptable photon statistics and reasonable signal intensity while maintaining convenient sample throughput. Consequently, the higher the desired throughput is, the larger the spacing between the lifetime codes has to be.

5.3.6. Flow speed

A key feature of FCM is high sample throughput. The throughput is determined by two factors, the speed and the diameter of the sample stream. The former determines how fast an object in the sample moves through the laser spot and therewith the time that can be used to measure a photoluminescence decay curve. It is controlled by the pressure applied to the flow cell. The latter determines the sample speed and the spacing between objects in the stream. Higher flow speed shortens the interaction time and therefore results in less photon counts, which broadens the lifetime distributions.

Figure 5.9 shows the dependence of the mean of the measured lifetimes and their standard deviation on the applied pressure for code D. A pressure variation from 180 to 30 hPa corresponds to interaction times roughly between 10 and 70 µs. With increasing pressure, the mean of the measured lifetimes as well as the standard deviation show a slight increase. The former indicates a decreased *SBR* whereas the latter could be a direct consequence of the lower number of collected photons (cf. Secs. 5.3.1 and 5.3.2) due to the faster flow speed. The decreased *SBR* most likely stems from the fixed measurement time window: after an object triggered its start of the measurement, the instrument collects data for a fixed time span. For higher flow speed, an object might have left the laser spot before this time span is over and additional background counts without signal from the sample are collected giving rise to a decreased *SBR* and consequently longer measured lifetimes. This problem could be circumvented by a dynamic adaption of the measurement time window.

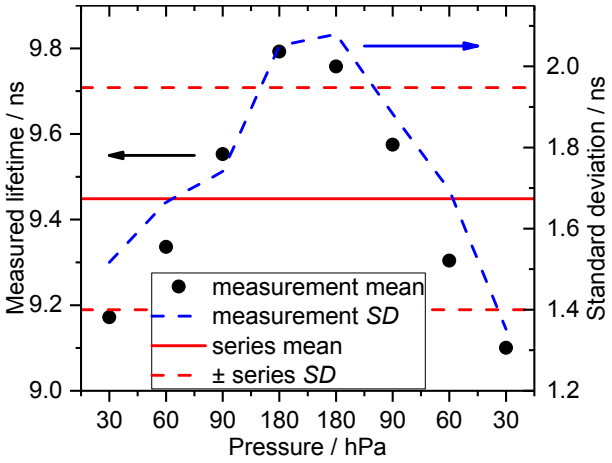

Figure 5.9: Influence of the applied pressure on the measured lifetimes. The deviations introduced by the different flow speeds are detectable even though they stay within the widths of the obtained lifetime distributions. Series mean and standard deviation involve all measurements at different pressures.
Previously published, reproduced from Ref. [53] (`https://creativecommons.org/licenses/by/4.0/`).

As expected, lower flow speeds allow for more precise lifetime measurements due to longer measurement time spans per particle. Thus, lifetime encoding could benefit from slower flow speeds. However, back diffusion of objects and ill-defined interaction times with the laser spot can reduce resolution for intensity-based encoding schemes.

5.3.7. Synopsis

The final results of lifetime measurements in time-domain flow cytometry depend on several parameters and conditions. We studied the impact of the number of acquired photon counts, the signal-to-background ratio, the integration time range, and the bin width, as well as the influence of technical parameters such as the detector operating range and applied flow speed on the lifetime determination.

It turned out that the most critical parameters are the signal-to-background ratio and the maximum intensity that the detector can handle without being saturated. Thus, care must be taken to avoid background counts and the recorded number of photons is mainly limited by the linear range of the detection system. However, since the mean of the lifetime values is independent of the number of detected photons, a low number of collected photons may not lead to high precision but still provides reproducible results. The coarse time binning only introduces predictable deviations that could be considered and corrected for, if necessary. A suitable choice of the integration time range for data analysis can be used to suppress the detrimental effects of strong background signals.

5.4. Encoding capabilities

The five lifetime code candidates presented in Sec. 5.1 serve as the model system to evaluate the capabilities of our LT-FCM setup. The outcomes of the preceding discussion in Sec. 5.3 can be used to optimize the discrimination capabilities and avoid obstacles. First, the signal intensity at the detector was balanced using neutral density filters to give acceptable photon statistics while avoiding non-linearity as good as possible, cf. Fig. 5.8. The accumulated photon counts for codes A to C could be kept below 200 counts per object. For codes D and E, however, the intensities were higher. Then, the time range for data analysis was chosen according to Fig. 5.6 to achieve best possible discrimination. Consequently, the integration time range is set to $\theta = 20$ ns. While this does not provide the best agreement between measured and reference lifetimes, it does provide the least overlap of lifetime codes and therefore the best discrimination. The pressure on the flow cell has been set to 40 hPa to ensure low flow speed and therewith longer interaction time per object as suggested by Fig. 5.9. This also avoids measuring background counts after an object has left the laser spot, improving the *SBR*. Resulting lifetime distributions of three codes are displayed in Fig. 5.10(a). The single distributions are clearly separated with small overlaps of 2.3 and 7.3 %.

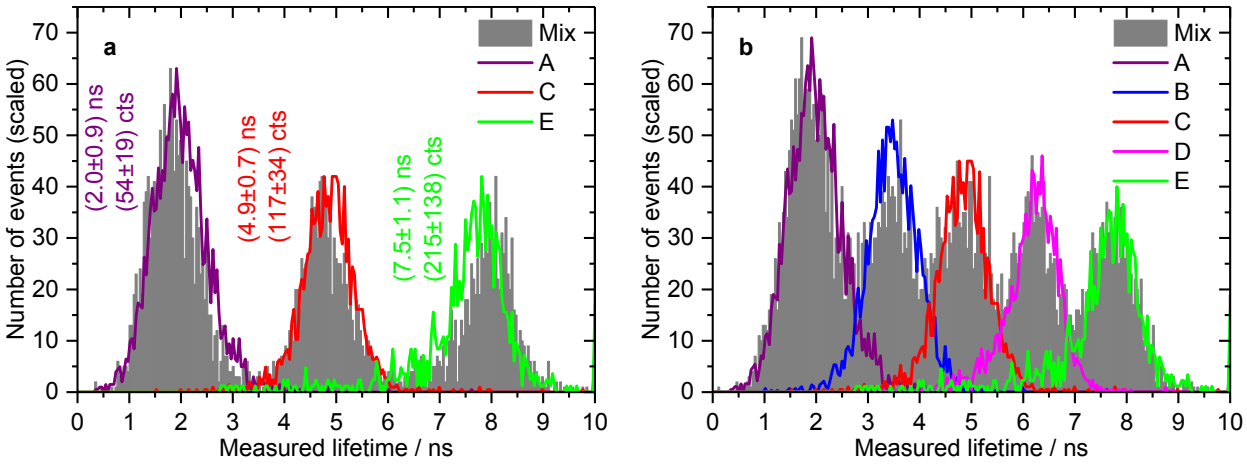

Figure 5.10: Lifetime distributions measured with the LT-FCM setup. (a) Three out of five available codes. Almost complete discrimination of the codes can be achieved. (b) All five codes. The detection of the five populations could be achieved. A quantitative assignment of each measured bead, however, is not possible.
(b) Previously published, adapted from Ref. [53] (`https://creativecommons.org/licenses/by/4.0/`).

For the calculation of the overlap, two distributions in question were area-normalized and the sum of the respective smaller value for each point of the two distributions were summed. Due to the limited time range θ, all lifetime code values are shifted with respect to the reference values in Tab. 5.1. Especially the long-lifetime code E deviates significantly from its reference value. This, however, was to be expected as the time range was adapted for maximum discrimination rather than accurate lifetime determination, and the coarse bin width systematically shortens the measured or simulated lifetimes, cf. Fig. 5.7. The shift of the lifetime distributions with respect to the reference lifetimes does not interfere with the concept of lifetime encoding since exact lifetime

determination is not necessarily required.

When the number of codes is increased to five, one obtains the distributions shown in Fig. 5.10(b). Even though there is distinct overlap of the distributions now hampering a strict discrimination, the respective distributions of the single codes are still recognizable. This might not be sufficient for applications like cell sorting were discrimination on a single-object level is required, but it could still allow for some rather qualitative analysis. In both cases, with only three or all five codes, the distributions of one-code samples and those of the mixtures show good agreement demonstrating the reproducibility from measurement to measurement.

Overall, these experiments prove the general feasibility of lifetime encoding. The luminescence lifetime could thus be used as an additional or stand-alone encoding parameter.

5.5. Application of lifetime encoding

A possible field of application for luminescence lifetime encoding is bead-based assays. The components involved in a typical bead-based immunoassay for two analytes are depicted in Fig. 5.11. The

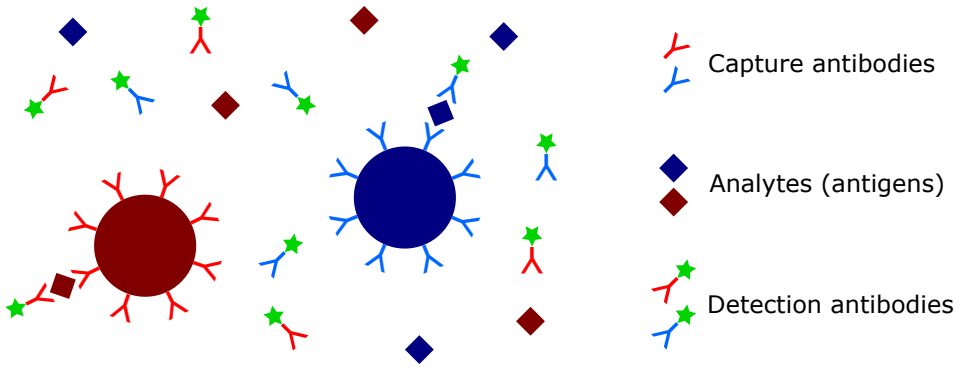

Figure 5.11: Schematic drawing of the components of a bead-based sandwich assay with two analytes. The encoded beads carry capture antibodies on their surfaces that specifically bind a certain antigen. Upon binding of the antigen, labeled detection antibodies are added that will bind to their respective antigens thereby forming a sandwich-like structure.

cores of the beads are encoded by means of some characteristic feature (e.g. spectral properties, fluorescence intensity, bead size). Each type of bead is surface-modified to carry analyte-specific bioligands or capture antibodies. Thus, there is a defined assignment of the bead code to the analyte to be captured by the bead. The capture antibodies on the bead surface bind the corresponding antigen if it is present in the sample. Additional labeled detector antibodies are then added to bind to the antigens that are attached to the capture antibodies. The result is a sandwich-like structure. In a flow cytometer, the code of the bead is read to determine the type of the bioligand attached to the bead surface and hence the analyte. The intensity of the fluorescent label of the detection antibody is used as a measure of the antigen concentration. Combining both pieces of information allows to detect the analyte and to determine its concentration.

Here, a proof-of-concept system based on streptavidin and biotin interaction using two lifetime codes for the beads is presented. This way it is still possible to validate the basic principle from a technical point of view without the complications of an optimization of a sophisticated assay. The bead codes A and C already given in Tab. 5.1 were used and fluorescently labeled biotin is bound to the streptavidin-modified bead surface. In the following, the labeled biotin will be referred to as the ligand.

The CLSM images in Fig. 5.12 exemplarily show the morphology of beads with lifetime code C and fluorescent ligands attached to the surface. The sample was excited at two wavelengths, 488

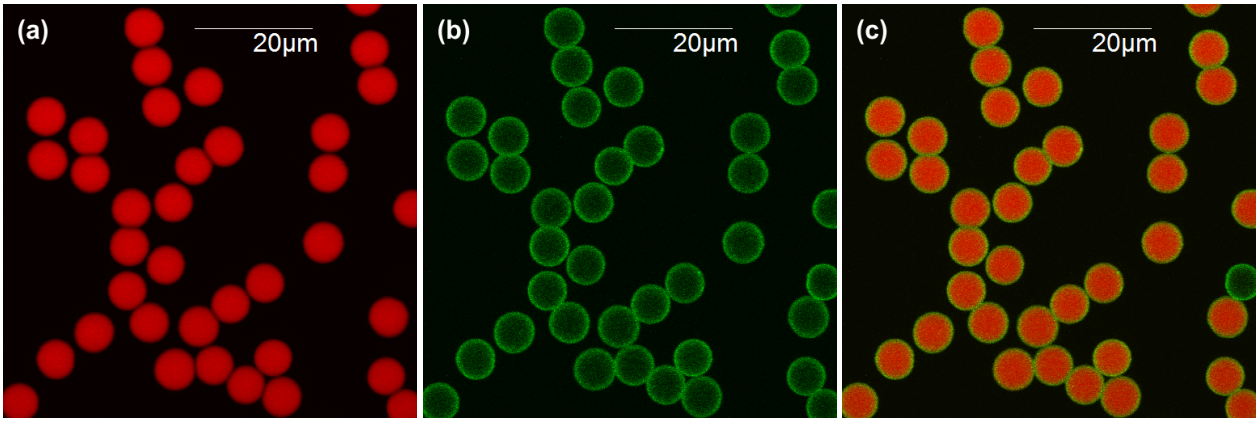

Figure 5.12: False-color CLSM images of PMMA beads loaded with dye Red (code C). (a) Spectral region of the core staining. (b) Spectral region of the fluorescently labeled ligands. (c) Overlay of both spectral channels. The spectrally different core encoding and the labeling of the ligands are clearly visible. Excitation wavelengths: 488 and 543 nm, DM351/488/543, first channel: 515(30) nm, second channel: 605(100) nm, 60x water immersion objective.

and 543 nm. The resulting fluorescence emission was measured in two channels: (605 ± 50) nm [Fig.5.12(a)] and (515 ± 15) nm [Fig. 5.12(b)]. The third panel, Fig. 5.12(c), shows an overlay of the intensity in the two channels. The panels of Fig. 5.12 clearly show the distinction between the lifetime-encoded core of the beads and the fluorescence from the biotin ligands attached to the streptavidin at the surface of the beads. Thus, two spectral channels can be used to read out the system. One channel covers the spectral region of emission from the bead cores and provides the time resolution. The second channel is used to detect the fluorescence intensity of the labeled biotin ligand and represents a measure for the quantification of the analyte.

More detailed information on the spectral properties of the bead-ligand system can be obtained from the ensemble spectra in Fig. 5.13(a). The excitation wavelength was set to 488 nm which matches the available excitation wavelength in the LT-FCM setup. It allows for single-wavelength excitation of both the lifetime-encoded beads and the fluorescent ligands. The emission of the fluorescent ligands has its maximum around 525 nm, the fluorescence spectra from the lifetime-encoded beads extend from around 550 nm into the near-infrared region. Thus, the fluorescent ligands can be detected with a bandpass filter whereas a longpass filter can be used for the lifetime

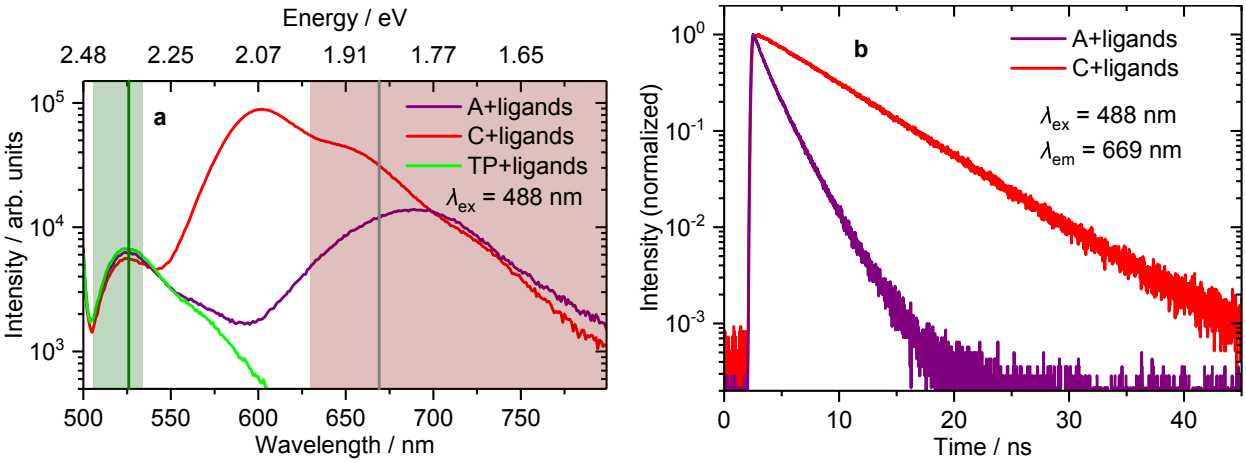

Figure 5.13: Optical-spectroscopic properties of bead ensembles of codes A and C with fluorescent ligands and a control sample TP without staining of the beads. (a) Fluorescence emission spectra. The fluorescent ligands emit in a spectral region around 525 nm. The lifetime codes could be detected with a suitable bandpass or longpass filter. The respective spectral regions used for LT-FCM are indicated by the shaded areas. (b) Fluorescence intensity decay curves of the two codes A and C. There is a significant difference in their decay dynamics.

encoding channel. It should be noted that the overlap of the emission spectra of code C and the fluorescent ligands may interfere with the ligand quantification. The fluorescence decay kinetics of both codes are displayed in Fig. 5.13(b). The two codes exhibit a substantial difference in their decay kinetics and their discrimination also proved to be straightforward at low count numbers, cf. Fig. 5.10.

For the demonstration of simultaneous lifetime encoding and readout of an analyte quantification signal, four samples were prepared: one negative sample without fluorescent ligands for each code and one positive sample with fluorescent ligands attached for each code. The flow cytometer setup described in Sec. 3.4 was used to analyze a mixture of the prepared samples.

A dotplot of lifetime code values and ligand fluorescence intensity, where each data point represents one detected object, can be found in Fig. 5.14. One can recognize four populations that represent

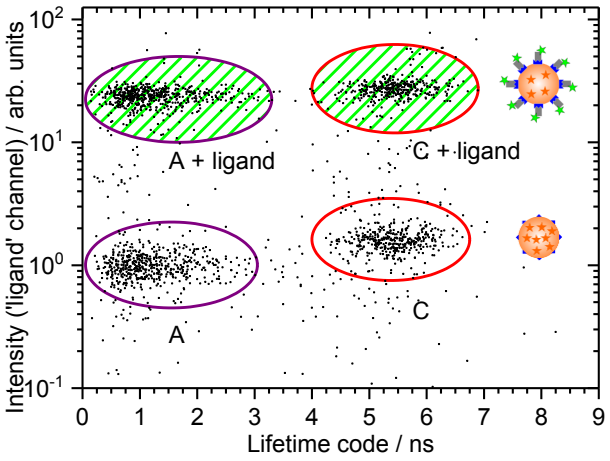

Figure 5.14: Dotplot of the ligand fluorescence intensity and the lifetime code obtained with the LT-FCM setup. Four populations are recognizable that represent two lifetime codes and resemble two different analyte concentrations in an actual assay.

the four different samples. Positive and negative samples are separated by more than one order of magnitude in fluorescence intensity in the respective spectral channel. This confirms that the ligand fluorescence signal could be exploited for the quantification of an analyte. The lifetime discrimination allows for reliable distinction between the two codes. Thus, it could be shown that lifetime encoding can be combined with ligand detection using different spectral channels while employing only one excitation light source.

5.6. Summary

Lifetime encoding in time-domain flow cytometry was demonstrated to be generally feasible. The accuracy of the lifetime determination depends not only on certain measurement conditions such as the number of acquired photons for a luminescence decay curve or the signal-to-background ratio. It also depends on technical limitations or parameters chosen for the data analysis: the bin width of the decay curves or the integration time range. Moreover, the trade-off between collecting as many photons as possible for each object while maintaining an acceptable throughput and considering the limited maximum intensity at the detector presents a major challenge. Thus, the data analysis and the signal intensities have to be optimized for each set of lifetime code carriers. With the current prototype setup, three codes can be fully discriminated and five codes can be identified.

As a first step towards bead-based assays with lifetime encoding, it was shown that lifetime codes from beads and ligand fluorescence intensities in a separate spectral channel can be detected simultaneously. Only one excitation wavelength was required.

6. Conclusions & Outlook

The concept of luminescence lifetime encoding in time-domain flow cytometry is intended to extend the parameter space for encoding in analytical applications. Luminophore-loaded beads are often used as a carrier system for multiplexing codes and may also be employed for instrument performance checks and calibration. Thus, an in-depth study of the optical-spectroscopic properties of exemplary dye-loaded polymer microbeads was carried out. The following assessment of lifetime encoding in time-domain flow cytometry was based on measurements with lifetime-encoded luminescent beads and a prototype lifetime flow cytometer combined with the analysis of synthetic data. Finally, the applicability of lifetime encoding for the readout of bead-based assays was demonstrated.

The study of Rh6G-loaded PMMA microbeads made in a dispersion polymerization process showed the expected influence of the polymer matrix on the incorporated dye. With respect to aqueous environment, shifts in the fluorescence excitation spectra occurred as well as a faster fluorescence intensity decay due to the difference in the refractive index between water and PMMA. Moreover, a high fluorescence anisotropy in weakly loaded beads confirmed the rigid confinement of the dye molecules. However, in addition a close connection between the synthesis conditions and characteristic optical-spectroscopic properties of the beads was revealed resulting in the following model. The anionic stabilizer AOT used during bead synthesis and the cationic dye Rh6G presumably form a complex that is preferentially incorporated close to the bead surface. This behavior leads to a size-dependent dye incorporation efficiency: small beads with a large surface-to-volume ratio exhibit a higher effective dye loading concentration than larger beads synthesized with the same nominal dye loading concentration. The high dye concentration in the resulting shell of the AOT-Rh6G complexes facilitates dye aggregation. Thus, three species of Rh6G exist in these beads: monomeric core dye molecules, near-surface monomers, and near-surface dye aggregates. The near-surface monomers and aggregates are exposed to water penetrating the outer regions of the beads. This partially counter-balances the spectral shifts introduced by the PMMA environment. Moreover, aggregation can lead to spectral broadening. Likewise, the fluorescence intensity decay of the near-surface monomers is more similar to that in aqueous environment due to the water penetration. This mainly affects the decay kinetics in small, weakly loaded beads. At higher dye loading concentration, aggregation gains importance and can drastically reduce the fluorescence quantum yield. In addition, shorter distances between dye molecules encourage intermolecular interactions. Evidence for an excitation energy migration process was found due to changes in the fluorescence decay kinetics and fluorescence anisotropy depending on the dye loading concentration. This energy migration presumably transports energy from the core monomers to the near-surface aggregates and monomers via a concentration gradient with increasing concentration towards the surface. The hypothesis of energy migration could be validated with the aid of random walk simulations.

The study of Rh6G-loaded PMMA microbeads shows the complex dependencies of fluorescence properties on the synthesis parameters. The findings thus underline the need for more detailed studies of fluorophore-loaded microbeads, which are used as standards and reference materials. With advances in measurement techniques, the rather small changes in these properties may become relevant for applications.

Further work should include dyes with different chemical properties, in particular neutral and anionic dyes, to gain deeper insight into incorporation mechanisms and the interaction between dyes and reagents. The synthesis conditions could be systematically modified to replace currently used stabilizers and surfactants with alternatives. This would help to clarify the mechanism behind the surface-specific incorporation and aggregation during synthesis. Also, the bead diameter range should be extended to include smaller beads. Ideally, an experimental procedure to determine the actual dye distribution in small polymer beads should be found. To this end, however, the conflict between insufficient spatial resolution in fluorescence-based methods, low sensitivity to the small differences in chemical composition between the dye molecules and the matrix in techniques for elemental analysis, and poor stability with respect to electron-based techniques such as cathodoluminescence needs to be circumvented. An approach might be possible using fluorophores with heavy atoms to allow for detection in, e.g., energy-dispersive X-ray spectroscopy. Also, depth profiles of the elemental composition could be determined by means of secondary-ion mass spectrometry.
Furthermore, improved random walk simulations could include the transition dipole moment orientation and therefore also provide information on fluorescence anisotropy. Additionally, more species of molecules could be included in the simulations to, e.g., also represent near-surface monomers that contribute slower decay due to water penetration. Also, a refined dye distribution that, e.g., includes another parameter for the dye concentration in the bead core could be applied.

A prototype flow cytometer capable of time-resolved measurements on the nanosecond time scale was assessed experimentally with a set of lifetime-encoded microbeads and by means of simulations with synthetic data. The synthetic data allowed for isolated analysis of certain parameters such as the number of acquired photons, the signal-to-background ratio, time bin width, and the data analysis procedure. The different parameters exhibit interfering effects on the obtained results, i.e. the lifetime distributions. A major concern in time-resolved flow cytometry is the low number of photons that can be acquired within the limited interaction time with the excitation light spot. Indeed, low photon count numbers increase the width of the lifetime distribution and therewith reduce the precision of lifetime code reading. However, even down to a single photon, the mean of the distributions stays constant and thus, statistically speaking, the lifetime determination remains correct. On the one hand, low photon count numbers are detrimental for a precise lifetime determination. On the other hand, technical complications can arise due to limitations in detection systems that face saturation and non-linearity at high intensities. These effects counter the advantages of more acquired photons as saturation can result in false mean values of distributions. The signal-to-background ratio turned out to strongly affect the lifetime distributions in diverse ways. A high signal-to-background ratio naturally provides the most reliable outcome. An increasing fraction of background counts not only deteriorates the precision, it also shifts the mean of the distribution to higher lifetimes. The shift steadily increases until the mean of the lifetime distribution reaches a constant defined by the time range used for analysis. Concurrently, the width of

the lifetime distribution begins to decrease again starting from the point at which the background is stronger than the signal. Consequently, measurements under high background conditions will give the illusion of precise results while providing systematically erroneous values. The size of the time bins for the decay curves has a systematic impact on the mean value of the obtained lifetime distributions that depends on the actual lifetime. The width of the distribution, however, remains unaffected. Thus, a coarse time binning introduces systematic, yet predictable deviations. Since exact measurements of the lifetimes of the encoding luminophores are not required for lifetime encoding approaches, systematic predictable deviations do not pose a fundamental issue.
With the current prototype flow cytometer, three lifetime codes can be strictly distinguished and the populations in a mixture of five codes can be identified upon optimization of the time range for data analysis and the luminescence intensity of the code-carrying beads. Moreover, the simultaneous readout of a spectrally different ligand fluorescence signal could be achieved. This demonstrates the applicability for the readout of bead-based immunoassays.

The reported outcomes can be used to make luminescence lifetime encoding ready for routine applications in time-domain flow cytometry. Apparently, the main challenges are the trade-off between avoiding detector saturation while acquiring as many photons as possible for each decay curve at high throughput, and the impact of background on the measured lifetimes. Concerning the former, it would be advantageous to change from square-wave excitation to pulsed excitation and to increase the repetition rate. At least two excitation pulses could replace one excitation phase of the square wave and the number of excitation-emission cycles would be at least doubled. As a result, the effective time for decay curve measurements would increase and thus allow distribution of the required number of photons over a larger measurement time window which reduces the load impinging on the detector. Generally, to distinguish a lower number of codes, also lower numbers of detected photons might be sufficient. For the latter, background suppression could be improved by using an adaptive time window for the measurement per object instead of a fixed time span after triggering. This would avoid measuring additional background after an object has left the excitation light spot. A better housing of the optical path and possible cooling of the detector could help to reduce stray light and electronic detector noise. Moreover, optical components should be carefully checked for possible autofluorescence and the excitation light source system must be designed such that residual emission in the 'off'-state is effectively suppressed. More sophisticated data analysis such as least-squares curve fitting, maximum likelihood approaches, or even artificial neural networks should be considered to handle remaining background. Another issue is the coarse time binning. This, however, is a rather predictable factor and could, at least for the purpose of lifetime encoding, be accepted or even corrected as a systematic offset.

A. Appendix

The appendix provides additional information on measurement artifacts due to bead concentration effects and the mathematical background for some of the concepts used in the presented studies.

A.1. Measurement artifacts due to bead concentration effects

In photoluminescence spectroscopy, there are two commonly known sources of artifacts related to luminophore concentration: excitation and emission inner filter effects [27]. These effects were described in Sec. 3.2.4. In short, the excitation inner filter effect causes broadening or inversion-like distortion of excitation spectra due to weakened excitation of the focal volume and the emission inner filter effect results in spectral distortion of emission spectra caused by reabsorption of photons.

The situation for particulate samples is additionally complex due to light scattering. Scattering of the excitation light increases the optical density of the sample which enhances the excitation inner filter effect without increasing the actual luminophore concentration. Scattering of emitted light could diminish the detectable signal intensity and increase the path length of emitted photons within the cuvette [89] and thereby increases the probability for reabsorption. Additionally, scattering is wavelength-dependent and depends on the bead size. In order to figure out the limits of the optical-spectroscopic characterization, measurements at different bead mass concentration (mg beads per ml sample volume) were performed. Figures A.1(a) and (b) display fluorescence excitation and emission spectra of Rh6G-loaded beads with 361 µmol/l nominal loading concentration and a mean diameter of 6.6 µm. Only for bead mass concentrations as high as 10 mg/ml (0.84 vol%, $\approx$ 32 µm mean free path between beads) a distinct broadening of the excitation spectrum and a redshift of the emission spectrum is observed. In comparison, the effect of bead concentration is much stronger in case of smaller beads with a mean diameter of 1.29 µm and the same nominal dye loading concentration as before. This is depicted in Figs. A.2(a) and (b). Here, the broadening and shifting sets in at around 0.1 mg/ml ($8.4 \cdot 10^{-3}$ vol%, $\approx$ 29 µm mean free path) and already exceeds that in larger beads when the concentration is only 0.5 mg/ml. At higher bead concentrations, the before mentioned inversion-like distortion of the excitation spectra and a continuous shifting of the emission spectra occur.

On the one hand, the effective dye loading concentration is higher in smaller beads as discussed in Sec. 4.1. On the other hand, this difference does not suffice to explain the deviations between the differently sized beads. Thus, the bead size or the bead number density (number of beads per ml sample volume) must play an important role for inner filter effects in particulate samples. For beads made of PMMA and diameters of several microns, scattering is dominated by forward scattering. Repetitive light scattering in could increase the effective path length for photons in the sample as was observed for smaller particles of different material [89]. Therefore, increased probability for scattering due to the larger number of beads in the sample with smaller beads

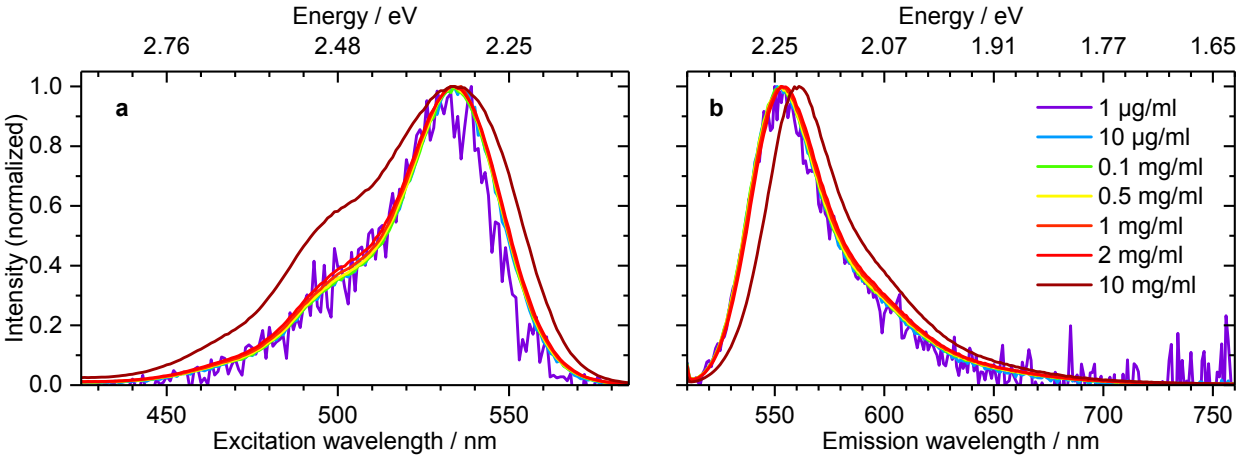

Figure A.1: Impact of the bead mass concentration of Rh6G-loaded beads (361 µmol/l nominal loading concentration) with 6.6 µm diameter on (a) the measured fluorescence excitation spectrum ($\lambda_{em} = 600$ nm) and (b) the measured fluorescence emissions spectrum ($\lambda_{ex} = 500$ nm). High bead concentrations lead to spectral broadening and shifts.

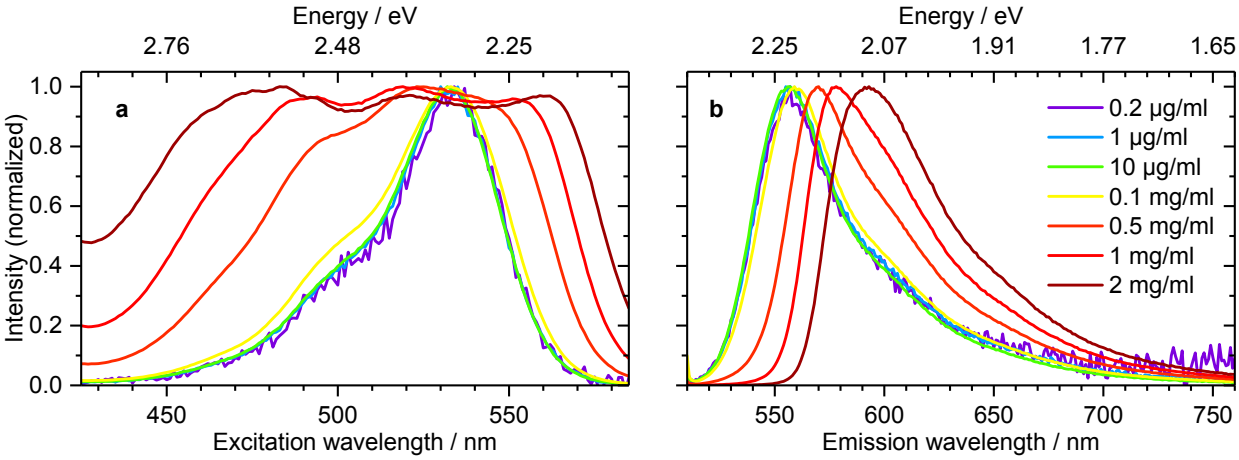

Figure A.2: Impact of the bead mass concentration of Rh6G-loaded beads (361 µmol/l nominal loading concentration) with 1.29 µm diameter on (a) the measured fluorescence excitation spectrum ($\lambda_{em} = 600$ nm) and (b) the measured fluorescence emissions spectrum ($\lambda_{ex} = 500$ nm). Already moderate bead concentrations lead to spectral distortions.

increases the actual path length for both incident and emitted photons. Hence, the probabilities for absorption and reabsorption rise and inner filter effects would be amplified.

The spectral shift in emission for both types of beads is displayed in dependence on the bead mass concentration and the bead number density in Figs. A.3(a) and (b), respectively. Clearly, the shifting sets in at much lower bead mass concentration for small beads, cf. Fig. A.3(a), whereas the onset is at a similar bead number density for both bead diameters, see Fig. A.3(b). Hence, the

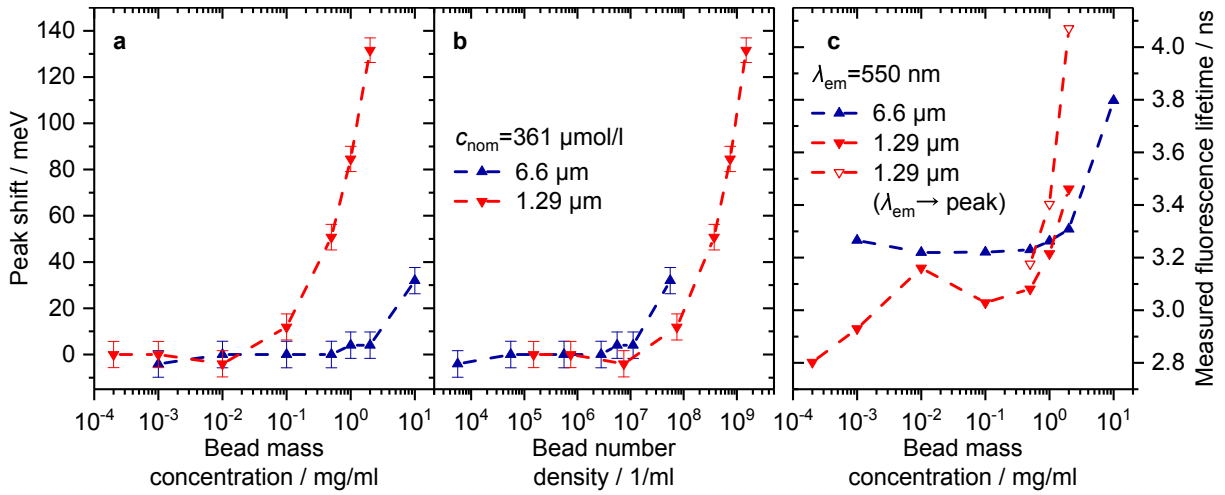

Figure A.3: Shift of the fluorescence emission peak position in dependence of (a) the bead mass concentration and (b) the bead number density. The dependence of the fluorescence lifetime on the bead mass concentration is shown in (c). Lifetimes have been calculated as intensity-weighted average lifetimes from multi-exponential decay fits to the data. For small beads, the detection wavelength had to be adapted due to the peak shift. Apparently, the extent of spectral shifts is determined by the bead number density instead of bead mass concentration. The fluorescence lifetime increases with increasing bead concentration.

parameter governing the magnitude of the shift is the number of beads, not the present polymer mass and therefore not only the amount of dye. This makes a notable difference compared to solutions where the inner filter effect is directly related to the amount of dye. Thus, light scattering indeed seems to amplify inner filter effects and has to be considered in measurements on particulate scattering systems.

Moreover, the emission inner filter effect is also known to increase the measured luminescence lifetime of a sample [27, 67, 90]. It does not change the molecular luminescence lifetime, i.e. the average time a molecule resides in an excited state. Rather, reabsorption might delay photon escape from the sample by introducing multiple emission steps before a photon actually leaves the sample. Figure A.3(c) shows the course of the measured fluorescence lifetime against the bead mass concentration. For the beads of intermediate size, there is a wide range of bead concentration without significant distortion of the lifetime determination. In case of small beads, however, a trend towards increasing lifetimes already starts at very low concentrations.

Based on these findings on distortion of results due to bead concentration effects, all measurements were carried out with appropriately low bead concentrations according to Fig. A.3 to ensure reliable results.

A.2. Mathematical background for the random walk simulations of energy migration

A certain dye distribution was assumed for the random walk simulations presented in Sec. 4.3. The positions of molecules were produced with a pseudo-random number generator (PRNG) according to the chosen distribution. For memory capacity reasons, and based on the spherical symmetry, only one eighth of a full sphere was considered. Hard wall boundary conditions were implemented at the side faces, which means that there are no molecule sites coupled to the outside of the considered octant. It is assumed that the deviations caused by runs close to the side faces of the volume are negligible. Molecules located within a minimum distance were excluded from the calculation to prevent quasi-infinite loops for a fictive trap at molecules in unphysically close proximity.

All numerical simulations have been carried out with custom-made *Octave* [85] scripts.

A.2.1. Generation of dye molecule distributions

Spherical coordinates are chosen as coordinate system (r: radial distance from the origin, φ: azimuth, ϑ: polar angle). The transformation is as usual [91]:

$$\begin{aligned} x &= r\cos(\varphi)\sin(\vartheta) \\ y &= r\sin(\varphi)\sin(\vartheta) \\ z &= r\cos(\vartheta)\,. \end{aligned}$$

The molecules have to be positioned according to chosen distributions being functions of r, φ and ϑ instead of x, y, z and the change of the volume element size with r and ϑ, namely $r^2\sin(\vartheta)$, has to be considered.

Radial monomial distributions

The actual distribution of the dye molecules inside the beads is unknown. Results from dissolving the beads suggest a very high concentration near the surface and low concentration in the center of the beads. Such a behavior might be described by a monomial dye distribution in r. Moreover, monomial distributions are straightforward to implement. The assumed distributions are independent of ϑ and φ and have an r^η-dependence on the radial position in the bead. Random values of φ can be generated directly from a PRNG as there is no φ-dependent term in the Jacobian determinant. Therefore, we only consider the probability distributions

$$\begin{aligned} p(r) &= \alpha_r r^\eta\,, \\ p(\vartheta) &= \alpha_\vartheta\,. \end{aligned}$$

The distributions have to be normalized to 1. Thus,

$$\int_0^R \mathrm{d}r\, r^2 p(r) \stackrel{!}{=} 1$$
$$\int_0^R \mathrm{d}r\, \alpha_r r^\eta r^2 = \alpha_r \frac{1}{\eta+3} R^{\eta+3} = 1$$
$$\Rightarrow \alpha_r = \frac{\eta+3}{R^{\eta+3}}$$

and

$$\int_0^{\frac{\pi}{2}} \mathrm{d}\vartheta\, \sin(\vartheta) p(\vartheta) \stackrel{!}{=} 1$$
$$\int_0^{\frac{\pi}{2}} \mathrm{d}\vartheta\, \alpha_\vartheta \sin(\vartheta) = \alpha_\vartheta \cdot 1 = 1$$
$$\Rightarrow \alpha_\vartheta = 1\,.$$

That means

$$p(r) = \frac{\eta+3}{R^{\eta+3}} r^\eta\,.$$

The transformation from uniformly distributed values generated by the PRNG to the desired distributions is required. The simulation range, and therefore the required coordinate values, is restricted to one eighth of a sphere (cf. above). With ζ being homogeneously distributed on $[0,1]$, the random numbers can be found as follows (see, e.g., Ref. [92] and Sec. A.4 for more details):

$$\begin{aligned}\zeta(r) &= \int_0^r \mathrm{d}r'\, r'^2\, p(r') \\ &= \int_0^r \mathrm{d}r'\, \frac{\eta+3}{R^{\eta+3}} r'^\eta r'^2 = \frac{\eta+3}{R^{\eta+3}} \frac{r^{\eta+3}}{\eta+3} = \frac{r^{\eta+3}}{R^{\eta+3}} \\ \Rightarrow r &= R\, \sqrt[\eta+3]{\zeta}\end{aligned}$$

and

$$\begin{aligned}\zeta(\vartheta) &= \int_0^\vartheta \mathrm{d}\vartheta' \sin(\vartheta') p(\vartheta') \\ &= \int_0^\vartheta \mathrm{d}\vartheta'\, \sin(\vartheta') = 1 - \cos(\vartheta) \\ \Rightarrow \vartheta &= \arccos(1-\zeta)\,.\end{aligned}$$

The generation of values of φ is given by

$$\varphi = \frac{\pi}{2}\zeta\,.$$

A.2.2. Parameters

Typical parameters used in the simulations are listed in Tab. A.1. As explained in Sec. 4.3, the use of these parameters leads to results that resemble those experimentally obtained for beads with a nominal dye loading concentration of 361 µmol/l and a diameter of 1.29 µm.

symbol	source code	description	typical value
R	R	bead radius	650 nm
d_{dd}	dd	mean dye-dye distance	8.5 nm
V_{mol}	VM	mean volume per molecule, $VM = \frac{4}{3}\pi(\frac{dd}{2})^3$	
	N	number of molecules	$5 \cdot 10^5$
r	r	radial coordinate	
η		exponent in dye distribution	120
φ	phi	polar angle coordinate	
ϑ	$theta$	azimuthal angle coordinate	
x, y, z	x, y, z	Cartesian coordinates	
R_F	$R0$	FRET radius	5 nm
τ_0	$tau0$	undisturbed lifetime of the molecules	3.75 ns
γ_{ra}	$gammar$	undisturbed rate of the molecules, $gammar = \frac{1}{tau0}$	
	$mindist$	minimum distance taken into account for steps	1.4 nm
d_{qs}	qs	thickness of the quenching shell	1.4 nm
M	M	number of runs	1000

Table A.1: Typical parameters in the random walk simulation.

A.3. Convergence behavior and reproducibility of the random walk simulations

This section is devoted to the question of reproducibility of the results presented in Sec. 4.3. Convergence and reproducibility are tested with respect to the number of runs, i.e. the number of simulated excitation-emission/quenching cycles, for a certain set of parameters. As a reference parameter set, the following values were used: exponent $\eta = 120$, bead diameter $D = 1.3$ µm, mean dye-dye distance $d_{\mathrm{dd}} = 8.5$ nm, quenching shell thickness $d_{\mathrm{qs}} = 1.4$ nm, Förster radius $R_{\mathrm{F}} = 5$ nm, undisturbed lifetime $\tau_0 = 3.75$ ns. Simulations with this parameter set but differing number of runs M have been performed. The simulated fluorescence decay curves obtained from this series are shown in Fig. A.4(a). Differences occur between the simulations with only 10 and ≥ 100 runs. For 100 runs and more, the decay curves show perfect agreement. The simulated efficiency of the different quenching pathways in dependence on the number of runs is depicted in Fig. A.4(b). Only for an unreasonable low number of 10 runs a significant deviation from the results at larger number of runs is observed. In summary, sufficiently accurate results are assumed for 1000 runs which is the minimum for all presented results from simulations. However, the reproducibility of the simulated decay curves also depends on the fraction of immediate quenching. If this fraction is too high, only a small number of runs will actually contribute to the decay kinetics since no

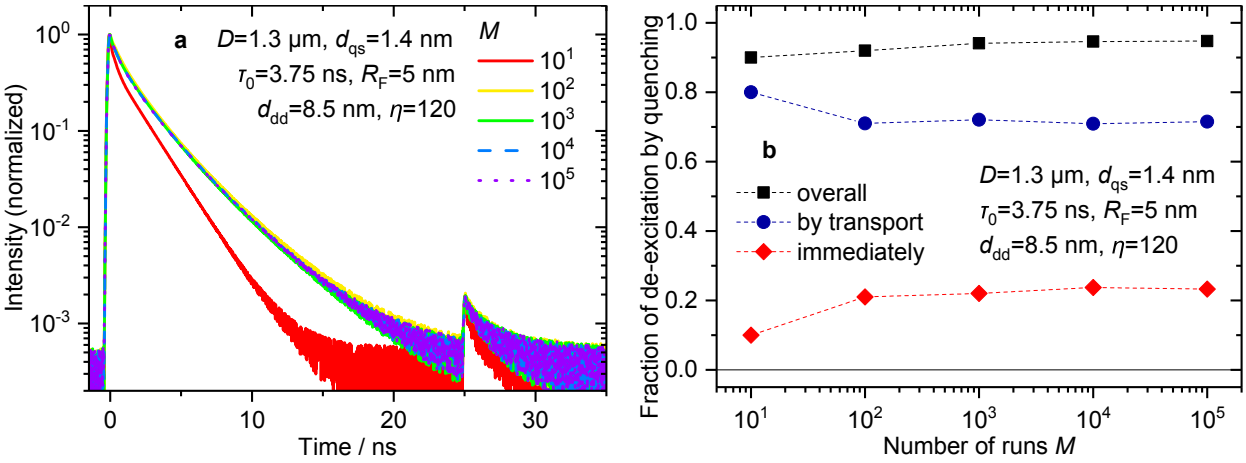

Figure A.4: Convergence behavior of the random walk simulations with respect to the number of runs. (a) Simulated fluorescence decay curves. (b) Efficiency of the different decay mechanisms. Convergence for this set of parameters is reliably given for 1000 runs which is the typical number of runs used throughout the presented simulation results. Simulations with less than 100 runs excluding immediate quenching should not be trusted.

decay rate constant is assigned to runs terminated by immediate quenching. The assumption of 1000 runs being sufficient holds true for a fraction of immediate quenching of around 20 %, cf. Fig. A.4(b). This limit is significantly exceeded for parts of the investigation of the impact of the bead diameter in Fig. 4.20 and most of the data points in the investigation concerning the quenching shell thickness in Fig. 4.17. However, a repetition of the simulations on the quenching shell thickness with 10^4 runs did not exhibit any notable differences. For the bead diameter series, simulations with small diameters have been performed with 10^5, 10^4, or $5 \cdot 10^3$ runs to ensure an adequate fraction of rate constants from energy transfer. Hence, all the presented results are statistically sound.

A.4. Numerical simulation of luminescence decay curves

Synthetic data were used in Sec. 5.3 to separately study influencing factors on the lifetime determination. To that end, randomly distributed counts following the probability distribution of photoluminescence decays (here: mono- and multi-exponential decays) are required. Thus, the output of a standard pseudo-random number generator (PRNG) which is usually uniform on $[0, 1]$, has to be transformed to the desired distributions. Two methods to achieve this transformation are briefly introduced in the following based on the text by `Koonin` [92].

A.4.1. Analytical approach for mono-exponential decays

In case of mono-exponential decay curves, the transformation can be done analytically. Assume, we need a random number distribution that displays a mono-exponential decay curve such as

$$I(t) = A\mathrm{e}^{-\frac{t}{\tau}}.$$

That means, we look for a probability distribution of t on $[0, \infty[$ with

$$w(t) = \frac{1}{\tau}\mathrm{e}^{-\frac{t}{\tau}} \qquad \text{and} \qquad \int_0^\infty \mathrm{d}t\, w(t) = 1\,.$$

In order to start from a uniform distribution as provided by most software for numerical analysis, we apply a change in variables to

$$\zeta(t) = \int_0^t \mathrm{d}t' w(t') \tag{A.1}$$

which gives $t \in [0, \infty[\rightarrow \zeta \in [0, 1]$. Uniformly distributed values of ζ can be transformed into the required distribution of t if Eq. (A.1) can be solved for t. For mono-exponential decay, we find

$$\begin{aligned}\zeta(t) &= \int_0^t \mathrm{d}t' \,\frac{1}{\tau}\mathrm{e}^{-\frac{t'}{\tau}} \\ &= \frac{1}{\tau}(-\tau)\left[\mathrm{e}^{-\frac{t'}{\tau}}\right]_0^t \\ &= 1 - \mathrm{e}^{-\frac{t}{\tau}}\,,\end{aligned}$$

which can be easily inverted:

$$t = -\tau \log_\mathrm{e}(1 - \zeta)\,. \tag{A.2}$$

Thus, for mono-exponential decays the problem has been reduced to generating a uniform distribution of ζ and using Eq. (A.2) to calculate the mono-exponential distribution of t. The method, however, cannot be applied to multi-exponential decays since the equivalent of Eq. (A.1) has no analytical solution for t.

A.4.2. Von Neumann rejection for multi-exponential decays

For cases, where Eq. (A.1) may not be inverted, the so-called von Neumann rejection can be used. Again, we assume that we need random variables t distributed as $w(t)$. Now we have to find a second distribution $w'(t)$ with $w'(t) > w(t)\,\forall t$. The distribution $w'(t)$ might also be a constant and its definite integral is, of course, larger than 1. The only requirement is that we are able to generate random numbers according to $w'(t)$ following, e.g., the analytical approach described above. One then generates pairs of values t_i (distributed according to w') and ξ (distributed uniformly on $[0, 1]$). For each pair, the value of t_i is accepted when

$$w(t_\mathrm{i})/w'(t_\mathrm{i}) > \xi \Rightarrow t_\mathrm{i} \text{ accepted} \tag{A.3}$$

and discarded otherwise. The process is repeated until the desired number of random values has been generated.

For multi-exponential decay,

$$w(t) = \frac{1}{\sum_j A_j \tau_j} \sum_j A_j \mathrm{e}_j^{-\frac{t}{\tau_j}} \qquad \text{and} \qquad \int_0^\infty \mathrm{d}t\, w(t) = 1$$

and a suitable choice of w' could be

$$w'(t) = \frac{\sum_j A_j}{\sum_j A_j \tau_j} \mathrm{e}^{-\frac{t}{\tau_\mathrm{m}}} ,$$

where $\tau_\mathrm{m} = \max(\tau_j)$. The values of $w'(t)$ are always larger than or equal to $w(t)$ since $w'(0) = w(0) = \frac{\sum_j A_j}{\sum_j A_j \tau_j}$ and $\mathrm{e}^{-\frac{t}{\tau_\mathrm{m}}}$ decays slower than the sum of exponential functions. To generate the random number distribution of w', we again need

$$\begin{aligned} \zeta'(t) &= \int_0^t \mathrm{d}t'\, w'(t') \\ &= \int_0^t \mathrm{d}t' \frac{\sum_j A_j}{\sum_j A_j \tau_j} \mathrm{e}^{-\frac{t'}{\tau_\mathrm{m}}} \\ &= \frac{\sum_j A_j}{\sum_j A_j \tau_j} \tau_\mathrm{m} \left[1 - \mathrm{e}^{-\frac{t}{\tau_\mathrm{m}}}\right] , \end{aligned}$$

which can be solved for t yielding

$$t = -\tau_\mathrm{m} \log_\mathrm{e} \left(1 - \frac{\sum_j A_j \tau_j}{\sum_j A_j} \frac{\zeta'}{\tau_\mathrm{m}}\right) \tag{A.4}$$

for $\zeta' \in [0, \int_0^\infty \mathrm{d}t\, w'(t)]$. Since in most cases $\int_0^\infty \mathrm{d}t\, w'(t) = \frac{\sum_j A_j}{\sum_j A_j \tau_j} \tau_\mathrm{m} \neq 1$, one would need to extend the range of the PRNG. However, defining

$$\begin{aligned} \zeta^* &= \left[\int_0^\infty \mathrm{d}t\, w'(t)\right]^{-1} \zeta' \\ &= \frac{\sum_j A_j \tau_j}{\sum_j A_j} \frac{\zeta'}{\tau_\mathrm{m}} \end{aligned} \tag{A.5}$$

and inserting Eq. (A.5) in Eq. (A.4) provides

$$t = -\tau_\mathrm{m} \log_\mathrm{e}(1 - \zeta^*)$$

with $\zeta^* \in [0, 1]$, which is in perfect similarity to Eq. (A.2). A loop generates pairs of t_i and ξ and checks the condition of Eq. (A.3) each time. The loop ends when the required number of accepted t_i has been generated.

A.5. Analytical expression for the standard deviation of lifetimes obtained from curve fitting

The standard deviation of lifetime distributions from numerical simulations has been compared to the standard deviation that would be expected for curve fitting to the data in Sec. 5.3. When background is absent, the expected variance of the lifetime estimation in mono-exponential least-square curve fitting is [87, 88]

$$\mathrm{var}_\tau = \frac{1}{N}\tau^2\frac{k^2}{r^2}\left(1-\mathrm{e}^{-r}\right)\left[\frac{\mathrm{e}^{r/k}\left(1-\mathrm{e}^{-r}\right)}{\left(\mathrm{e}^{r/k}-1\right)^2}-\frac{k^2}{\mathrm{e}^r-1}\right], \tag{A.6}$$

where N is the number of photon counts, τ the actual lifetime, θ the integration time range, k the number of bins, and $r=\theta/\tau$. In case of background signal being present, the expression changes to [87]

$$\begin{aligned}
\mathrm{var}_{\tau,\mathrm{bg}} &= -\left[\frac{T^2}{\tau^4}\sum_{i=1}^{k} y_i\frac{\partial^2 \ln y_i}{\partial r^2}\right]^{-1}\\
y_i = Np_i &= \frac{N}{k}\frac{1}{1-\mathrm{e}^{-r}}\left[b\left(1-\mathrm{e}^{-r}\right)+k(1-b)\left(\mathrm{e}^{\frac{1-i}{k}r}-\mathrm{e}^{-\frac{i}{k}r}\right)\right]\\
\frac{\partial^2 \ln y_i}{\partial r^2} &= \frac{\mathrm{e}^r}{\left(1-\mathrm{e}^r\right)^2}+\frac{-b\mathrm{e}^{-r}+k(1-b)\left[\left(\frac{1-i}{k}\right)^2\mathrm{e}^{\frac{1-i}{k}r}-(\frac{i}{k})^2\mathrm{e}^{-\frac{i}{k}r}\right]}{k(1-\mathrm{e}^{-r})p_i}\\
&\quad-\left[\frac{b\mathrm{e}^{-r}+k(1-b)\left(\frac{1-i}{k}\mathrm{e}^{\frac{1-i}{k}r}-\mathrm{e}^{-\frac{i}{k}r}\right)}{k(1-\mathrm{e}^{-r})p_i}\right]^2\\
b &= \left[1+SBR\right]^{-1}.
\end{aligned} \tag{A.7}$$

Bibliography

[1] J. R. Lakowicz (ed.): *Principles of Fluorescence Spectroscopy*. Springer US; 3rd edn., 2006; ISBN 978-0-387-46312-4; doi:10.1007/978-0-387-46312-4.

[2] G. Henel & J. L. Schmitz: *Basic Theory and Clinical Applications of Flow Cytometry*. Laboratory Medicine 38(7), pp. 428–436, 2007; doi:10.1309/ghlewlv0cd8025jl.

[3] V. V. Tuchin (ed.): *Advanced Optical Flow Cytometry*. Wiley-VCH Verlag GmbH & Co. KGaA, 2011; doi:10.1002/9783527634286.

[4] O. S. Wolfbeis: *An overview of nanoparticles commonly used in fluorescent bioimaging*. Chemical Society Reviews 44(14), pp. 4743–4768, 2015; doi:10.1039/c4cs00392f.

[5] S. Birtwell & H. Morgan: *Microparticle encoding technologies for high-throughput multiplexed suspension assays*. Integrative Biology 1(5–6), pp. 345–362, 2009; doi:10.1039/b905502a.

[6] S. P. Perfetto, P. K. Chattopadhyay & M. Roederer: *Seventeen-colour flow cytometry: unravelling the immune system*. Nature Reviews Immunology 4(8), pp. 648–655, 2004; doi:10.1038/nri1416.

[7] S. Rödiger, C. Liebsch, C. Schmidt, W. Lehmann, U. Resch-Genger, U. Schedler & P. Schierack: *Nucleic acid detection based on the use of microbeads: a review*. Microchimica Acta 181(11–12), pp. 1151–1168, 2014; doi:10.1007/s00604-014-1243-4.

[8] S. Schmutz, M. Valente, A. Cumano & S. Novault: *Spectral Cytometry has Unique Properties Allowing Multicolor Analysis of Cell Suspensions Isolated from Solid Tissues*. PLoS ONE 11(8), p. e0159961, 2016; doi:10.1371/journal.pone.0159961.

[9] P. K. Chattopadhyay & M. Roederer: *Cytometry: Today's technology and tomorrow's horizons*. Methods 57(3), pp. 251–258, 2012; doi:10.1016/j.ymeth.2012.02.009.

[10] C. Chen, L. Ao, Y.-T. Wu, V. Cifliku, M. Cardoso Dos Santos, E. Bourrier, M. Delbianco, D. Parker, J. M. Zwier, L. Huang & N. Hildebrandt: *Single-Nanoparticle Cell Barcoding by Tunable FRET from Lanthanides to Quantum Dots*. Angewandte Chemie International Edition 57(41), pp. 13686–13690, 2018; doi:10.1002/anie.201807585.

[11] A. I. Skilitsi, T. Turko, D. Cianfarani, S. Barre, W. Uhring, U. Hassiepen & J. Léonard: *Towards sensitive, high-throughput, biomolecular assays based on fluorescence lifetime*. Methods and Applications in Fluorescence 5(3), p. 034002, 2017; doi:10.1088/2050-6120/aa7f66.

[12] P. Sarder, D. Maji & S. Achilefu: *Molecular Probes for Fluorescence Lifetime Imaging.* Bioconjugate Chemistry 26(6), pp. 963–974, 2015; doi:10.1021/acs.bioconjchem.5b00167.

[13] K. Hoffmann, T. Behnke, M. Grabolle & U. Resch-Genger: *Nanoparticle-encapsulated vis- and NIR-emissive fluorophores with different fluorescence decay kinetics for lifetime multiplexing.* Analytical and Bioanalytical Chemistry 406(14), pp. 3315–3322, 2014; doi:10.1007/s00216-013-7597-3.

[14] K. Hoffmann, T. Behnke, D. Drescher, J. Kneipp & U. Resch-Genger: *Near-Infrared-Emitting Nanoparticles for Lifetime-Based Multiplexed Analysis and Imaging of Living Cells.* ACS Nano 7(8), pp. 6674–6684, 2013; doi:10.1021/nn4029458.

[15] L. Marcu: *Fluorescence Lifetime Techniques in Medical Applications.* Annals of Biomedical Engineering 40(2), pp. 304–331, 2012; doi:10.1007/s10439-011-0495-y.

[16] M. Grabolle, P. Kapusta, T. Nann, X. Shu, J. Ziegler & U. Resch-Genger: *Fluorescence Lifetime Multiplexing with Nanocrystals and Organic Labels.* Analytical Chemistry 81(18), pp. 7807–7813, 2009; doi:10.1021/ac900934a.

[17] T. Mayr, C. Moser & I. Klimant: *Luminescence decay time encoding of magnetic micro spheres for multiplexed analysis.* Analytica Chimica Acta 597(1), pp. 137–144, 2007; doi:10.1016/j.aca.2007.06.030.

[18] J. P. Houston, Z. Yang, J. Sambrano, W. Li, K. Nichani & G. Vacca: *Overview of Fluorescence Lifetime Measurements in Flow Cytometry*; pp. 421–446. Springer New York, New York, NY, 2018; ISBN 978-1-4939-7346-0; doi:10.1007/978-1-4939-7346-0_18.

[19] L. Bene & L. Damjanovich: *The other side of the coin: Time-domain fluorescence lifetime in flow.* Cytometry Part A 87(2), pp. 101–103, 2015; doi:10.1002/cyto.a.22615.

[20] R. Cao, M. A. Naivar, M. Wilder & J. P. Houston: *Expanding the potential of standard flow cytometry by extracting fluorescence lifetimes from cytometric pulse shifts.* Cytometry Part A 85(12), pp. 999–1010, 2014; doi:10.1002/cyto.a.22574.

[21] R. Cao, V. Pankayatselvan & J. P. Houston: *Cytometric sorting based on the fluorescence lifetime of spectrally overlapping signals.* Optics Express 21(12), pp. 14816–14831, 2013; doi:10.1364/oe.21.014816.

[22] J. P. Houston, M. A. Naivar & J. P. Freyer: *Digital analysis and sorting of fluorescence lifetime by flow cytometry.* Cytometry Part A 77A(9), pp. 861–872, 2010; doi:10.1002/cyto.a.20930.

[23] J. F. Keij & J. A. Steinkamp: *Flow cytometric characterization and classification of multiple dual-color fluorescent microspheres using fluorescence lifetime.* Cytometry 33(3), pp. 318–323, 1998; doi:10.1002/(sici)1097-0320(19981101)33:3<318::aid-cyto5>3.0.co;2-c.

[24] J. A. Steinkamp & H. A. Crissman: *Resolution of fluorescence signals from cells labeled with fluorochromes having different lifetimes by phase-sensitive flow cytometry.* Cytometry 14(2), pp. 210–216, 1993; doi:10.1002/cyto.990140214.

[25] T. Niehörster, A. Löschberger, I. Gregor, B. Krämer, H.-J. Rahn, M. Patting, F. Koberling, J. Enderlein & M. Sauer: *Multi-target spectrally resolved fluorescence lifetime imaging microscopy.* Nature Methods 13(3), pp. 257–262, 2016; doi:10.1038/nmeth.3740.

[26] H. Wang, Y. Qi, T. J. Mountziaris & C. D. Salthouse: *A portable time-domain LED fluorimeter for nanosecond fluorescence lifetime measurements.* Review of Scientific Instruments 85(5), p. 055003, 2014; doi:10.1063/1.4873330.

[27] B. Valeur & M. N. Berberan-Santos: *Molecular Fluorescence.* Wiley-VCH Verlag GmbH & Co. KGaA; 2nd edn., 2012; ISBN 978-3-527-32837-6.

[28] J. A. Steinkamp & J. F. Keij: *Fluorescence intensity and lifetime measurement of free and particle-bound fluorophore in a sample stream by phase-sensitive flow cytometry.* Review of Scientific Instruments 70(12), pp. 4682–4688, 1999; doi:10.1063/1.1150143.

[29] C. Deka, L. A. Sklar & J. A. Steinkamp: *Fluorescence lifetime measurements in a flow cytometer by amplitude demodulation using digital data acquisition technique.* Cytometry 17(1), pp. 94–101, 1994; doi:10.1002/cyto.990170112.

[30] J. A. Steinkamp, T. M. Yoshida & J. C. Martin: *Flow cytometer for resolving signals from heterogeneous fluorescence emissions and quantifying lifetime in fluorochrome-labeled cells/particles by phase-sensitive detection.* Review of Scientific Instruments 64(12), pp. 3440–3450, 1993; doi:10.1063/1.1144265.

[31] B. G. Pinsky, J. J. Ladasky, J. R. Lakowicz, K. Berndt & R. A. Hoffman: *Phase-resolved fluorescence lifetime measurements for flow cytometry.* Cytometry 14(2), pp. 123–135, 1993; doi:10.1002/cyto.990140204.

[32] J. Nedbal, V. Visitkul, E. Ortiz-Zapater, G. Weitsman, P. Chana, D. R. Matthews, T. Ng & S. M. Ameer-Beg: *Time-domain microfluidic fluorescence lifetime flow cytometry for high-throughput Förster resonance energy transfer screening.* Cytometry Part A 87(2), pp. 104–118, 2015; doi:10.1002/cyto.a.22616.

[33] A. V. Gohar, R. Cao, P. Jenkins, W. Li, J. P. Houston & K. D. Houston: *Subcellular localization-dependent changes in EGFP fluorescence lifetime measured by time-resolved flow cytometry.* Biomedical Optics Express 4(8), pp. 1390–1400, 2013; doi:10.1364/boe.4.001390.

[34] H. H. Cui, J. G. Valdez, J. A. Steinkamp & H. A. Crissman: *Fluorescence lifetime-based discrimination and quantification of cellular DNA and RNA with phase-sensitive flow cytometry.* Cytometry Part A 52A(1), pp. 46–55, 2003; doi:10.1002/cyto.a.10022.

[35] B. L. Sailer, J. G. Valdez, J. A. Steinkamp, Z. Darzynkiewicz & H. A. Crissman: *Monitoring Uptake of Ellipticine and Its Fluorescence Lifetime in Relation to the Cell Cycle Phase by Flow Cytometry.* Experimental Cell Research 236(1), pp. 259–267, 1997; doi:10.1006/excr.1997.3717.

[36] C. Deka, B. E. Lehnert, N. M. Lehnert, G. M. Jones, L. A. Sklar & J. A. Steinkamp: *Analysis of fluorescence lifetime and quenching of FITC-conjugated antibodies on cells by phase-sensitive flow cytometry.* Cytometry 25(3), pp. 271–279, 1996; doi: 10.1002/(sici)1097-0320(19961101)25:3<271::aid-cyto8>3.0.co;2-i.

[37] B. Sailer, A. Nastasi, J. Valdez, J. Steinkamp & H. Crissman: *Interactions of intercalating fluorochromes with DNA analyzed by conventional and fluorescence lifetime flow cytometry utilizing deuterium oxide.* Cytometry 25(2), pp. 164–172, 1996; doi:10.1002/(sici) 1097-0320(19961001)25:2<164::aid-cyto5>3.0.co;2-h.

[38] C. Deka & J. A. Steinkamp: *Time-resolved fluorescence-decay measurement and analysis on single cells by flow cytometry.* Applied Optics 35(22), pp. 4481–4489, 1996; doi:10.1364/ ao.35.004481.

[39] W. Li, G. Vacca, M. Castillo, K. D. Houston & J. P. Houston: *Fluorescence lifetime excitation cytometry by kinetic dithering.* ELECTROPHORESIS 35(12–13), pp. 1846–1854, 2014; doi:10.1002/elps.201300618.

[40] J. Léonard, N. Dumas, J.-P. Caussé, S. Maillot, N. Giannakopoulou, S. Barre & W. Uhring: *High-throughput time-correlated single photon counting.* Lab Chip 14(22), pp. 4338–4343, 2014; doi:10.1039/c4lc00780h.

[41] J. P. Nolan & F. Mandy: *Multiplexed and microparticle-based analyses: Quantitative tools for the large-scale analysis of biological systems.* Cytometry Part A 69A(5), pp. 318–325, 2006; doi:10.1002/cyto.a.20266.

[42] S. P. Perfetto, D. Ambrozak, R. Nguyen, P. K. Chattopadhyay & M. Roederer: *Quality assurance for polychromatic flow cytometry using a suite of calibration beads.* Nature Protocols 7(12), pp. 2067–2079, 2012; doi:10.1038/nprot.2012.126.

[43] T. Kalina, , J. Flores-Montero, V. H. J. van der Velden, M. Martin-Ayuso, S. Böttcher, M. Ritgen, J. Almeida, L. Lhermitte, V. Asnafi, A. Mendonça, R. de Tute, M. Cullen, L. Sedek, M. B. Vidriales, J. J. Pérez, J. G. te Marvelde, E. Mejstrikova, O. Hrusak, T. Szczepański, J. J. M. van Dongen & A. Orfao: *EuroFlow standardization of flow cytometer instrument settings and immunophenotyping protocols.* Leukemia 26, pp. 1986–2010, 2012; doi:10.1038/leu.2012.122.

[44] A. Mittag & A. Tárnok: *Basics of standardization and calibration in cytometry – a review.* Journal of Biophotonics 2(8-9), pp. 470–481, 2009; doi:10.1002/jbio.200910033.

[45] R. M. Zucker, P. Rigby, I. Clements, W. Salmon & M. Chua: *Reliability of confocal microscopy spectral imaging systems: Use of multispectral beads.* Cytometry Part A 71A(3), pp. 174–189, 2007; doi:10.1002/cyto.a.20371.

[46] R. M. Zucker & O. T. Price: *Statistical evaluation of confocal microscopy images.* Cytometry 44(4), pp. 295–308, 2001; doi:10.1002/1097-0320(20010801)44:4<295::aid-cyto1121> 3.0.co;2-c.

[47] A. Schwartz, G. E. Marti, R. Poon, J. W. Gratama & E. Fernández-Repollet: *Standardizing flow cytometry: A classification system of fluorescence standards used for flow cytometry.* Cytometry 33(2), pp. 106–114, 1998; doi:10.1002/(sici)1097-0320(19981001)33:2<106::aid-cyto4>3.0.co;2-h.

[48] V. Zenger, R. Vogt, F. Mandy, A. Schwartz & G. Marti: *Quantitative flow cytometry: Inter-laboratory variation.* Cytometry 33(2), pp. 138–145, 1998; doi:10.1002/(sici)1097-0320(19981001)33:2<138::aid-cyto8>3.0.co;2-f.

[49] A. Reisch & A. S. Klymchenko: *Fluorescent Polymer Nanoparticles Based on Dyes: Seeking Brighter Tools for Bioimaging.* Small 12(15), pp. 1968–1992, 2016; doi:10.1002/smll.201503396.

[50] A. P. Green & A. R. Buckley: *Solid state concentration quenching of organic fluorophores in PMMA.* Physical Chemistry Chemical Physics 17(2), pp. 1435–1440, 2015; doi:10.1039/c4cp05244g.

[51] T. Behnke, C. Würth, E.-M. Laux, K. Hoffmann & U. Resch-Genger: *Simple strategies towards bright polymer particles via one-step staining procedures.* Dyes and Pigments 94(2), pp. 247–257, 2012; doi:10.1016/j.dyepig.2012.01.021.

[52] D. Kage, L. Fischer, K. Hoffmann, T. Thiele, U. Schedler & U. Resch-Genger: *Close Spectroscopic Look at Dye-Stained Polymer Microbeads.* The Journal of Physical Chemistry C 122(24), pp. 12782–12791, 2018; doi:10.1021/acs.jpcc.8b02546.

[53] D. Kage, K. Hoffmann, M. Wittkamp, J. Ameskamp, W. Göhde & U. Resch-Genger: *Luminescence lifetime encoding in time-domain flow cytometry.* Scientific Reports 8(1), p. 16715, 2018; doi:10.1038/s41598-018-35137-5.

[54] N. J. Turro: *Modern Molecular Photochemistry.* University Science Books, 1991; ISBN 0-935702-71-7.

[55] D. Andrews: *Molecular Photophysics and Spectroscopy.* Morgan & Claypool Publishers, 2014; ISBN 978-1-627-05288-7; doi:10.1088/978-1-627-05288-7.

[56] J. B. Birks: *Photophysics of Aromatic Molecules.* John Wiley & Sons Ltd., 1970; ISBN 0-471-07420-9.

[57] M. J. S. Dewar & R. C. Dougherty: *The PMO theory of organic chemistry.* Plenum Press, 1975; ISBN 0-306-30779-0.

[58] A. Szabo & N. S. Ostlund: *Modern Quantum Chemistry.* Dover Publications Inc., 1996; ISBN 978-0-486-69186-2.

[59] H. Haken & H. C. Wolf: *Molekülphysik und Quantenchemie.* Springer-Verlag; 5th edn., 2006; ISBN 978-3-540-30314-5; doi:10.1007/3-540-30315-4.

[60] J. I. Steinfeld: *Molecules and Radiation: An Introduction to Modern Molecular Spectroscopy.* Dover Publications, Inc.; 2nd edn., 2005; ISBN 978-0-486-44152-8.

[61] J. W. Verhoeven: *Glossary of terms used in photochemistry (IUPAC Recommendations 1996)*. Pure and Applied Chemistry 68(12), pp. 2223–2286, 1996; doi:10.1351/pac199668122223.

[62] T. Förster: *Zwischenmolekulare Energiewanderung und Fluoreszenz*. Annalen der Physik 437(1-2), pp. 55–75, 1948; doi:10.1002/andp.19484370105.

[63] N. Gfeller & G. Calzaferri: *Energy Migration in Dye-Loaded Hexagonal Microporous Crystals*. The Journal of Physical Chemistry B 101(8), pp. 1396–1408, 1997; doi:10.1021/jp962776l.

[64] D. V. O'Connor & D. Phillips: *Time-correlated Single Photon Counting*. Academic Press, Inc., 1984; ISBN 0-12-524140-2.

[65] A. S. R. Koti, M. M. G. Krishna & N. Periasamy: *Time-Resolved Area-Normalized Emission Spectroscopy (TRANES): A Novel Method for Confirming Emission from Two Excited States*. The Journal of Physical Chemistry A 105(10), pp. 1767–1771, 2001; doi:10.1021/jp004361c.

[66] S. E. Braslavsky: *Glossary of terms used in photochemistry, 3rd edition (IUPAC Recommendations 2006)*. Pure and Applied Chemistry 79(3), pp. 293–465, 2007; doi:10.1351/pac200779030293.

[67] J. Baumann, G. Calzaferri & T. Hugentobler: *Self-absorption and re-emission in wavelength-dependent fluorescence decay*. Chemical Physics Letters 116(1), pp. 66–72, 1985; doi:10.1016/0009-2614(85)80127-5.

[68] S. Shen, E. D. Sudol & M. S. El-Aasser: *Dispersion polymerization of methyl methacrylate: Mechanism of particle formation*. Journal of Polymer Science Part A: Polymer Chemistry 32(6), pp. 1087–1100, 1994; doi:10.1002/pola.1994.080320611.

[69] C. M. Tseng, Y. Y. Lu, M. S. El-Aasser & J. W. Vanderhoff: *Uniform polymer particles by dispersion polymerization in alcohol*. Journal of Polymer Science Part A: Polymer Chemistry 24(11), pp. 2995–3007, 1986; doi:10.1002/pola.1986.080241126.

[70] R. Reisfeld, R. Zusman, Y. Cohen & M. Eyal: *The spectroscopic behaviour of rhodamine 6G in polar and non-polar solvents and in thin glass and PMMA films*. Chemical Physics Letters 147(2-3), pp. 142–147, 1988; doi:10.1016/0009-2614(88)85073-5.

[71] A. Shundo, K. Hori, D. P. Penaloza, K. Yoshihiro, M. Annaka & K. Tanaka: *Nonsolvents-induced swelling of poly(methyl methacrylate) nanoparticles*. Physical Chemistry Chemical Physics 15(39), pp. 16574–16578, 2013; doi:10.1039/c3cp52673a.

[72] K. Tanaka, Y. Fujii, H. Atarashi, K. i. Akabori, M. Hino & T. Nagamura: *Nonsolvents Cause Swelling at the Interface with Poly(methyl methacrylate) Films*. Langmuir 24(1), pp. 296–301, 2008; doi:10.1021/la702132t.

[73] F. Stevens: *Spectrophotometric measurement of swelling of polymer films by very poor solvents*. Journal of Applied Polymer Science 97(3), pp. 1082–1089, 2005; doi:10.1002/app.21611.

[74] P. Bojarski: *Concentration quenching and depolarization of rhodamine 6G in the presence of fluorescent dimers in polyvinyl alcohol films*. Chemical Physics Letters 278(4–6), pp. 225–232, 1997; doi:10.1016/s0009-2614(97)00971-8.

[75] A. P. Demchenko (ed.): *Advanced Fluorescence Reporters in Chemistry and Biology II*; *Springer Series on Fluorescence*, vol. 9. Springer Berlin Heidelberg, 2010; ISBN 978-3-642-04701-5; doi:10.1007/978-3-642-04701-5.

[76] D. Toptygin: *Effects of the Solvent Refractive Index and Its Dispersion on the Radiative Decay Rate and Extinction Coefficient of a Fluorescent Solute*. Journal of Fluorescence 13(3), pp. 201–219, 2003; doi:10.1023/a:1025033731377.

[77] D. Magde, R. Wong & P. G. Seybold: *Fluorescence Quantum Yields and Their Relation to Lifetimes of Rhodamine 6G and Fluorescein in Nine Solvents: Improved Absolute Standards for Quantum Yields*. Photochemistry and Photobiology 75(4), pp. 327–334, 2002; doi:10.1562/0031-8655(2002)0750327fqyatr2.0.co2.

[78] N. Sultanova, S. Kasarova & I. Nikolov: *Dispersion Properties of Optical Polymers*. Acta Physica Polonica A 116(4), pp. 585–587, 2009; doi:10.12693/aphyspola.116.585.

[79] D. R. Lide (ed.): *CRC Handbook of Chemistry and Physics*. CRC Press; 84th edn., 2003; ISBN 9780849304842.

[80] L. B.-Å. Johansson: *Limiting fluorescence anisotropies of perylene and xanthene derivatives*. Journal of the Chemical Society, Faraday Transactions 86(12), pp. 2103–2107, 1990; doi:10.1039/ft9908602103.

[81] A. Kawski, A. Kubicki, I. Weyna & I. Janić: *Temperature Dependence of Limiting Fluorescence Anisotropy of POPOP in Cellulose Acetate Film*. Zeitschrift für Naturforschung 40a, pp. 559–561, 1985.

[82] T. Förster: *Fluoreszenz organischer Verbindungen*. Vandenhoeck & Ruprecht, 1982; ISBN 978-3-525-42312-7.

[83] C. On, E. K. Tanyi, E. Harrison & M. A. Noginov: *Effect of molecular concentration on spectroscopic properties of poly(methyl methacrylate) thin films doped with rhodamine 6G dye*. Opt. Mater. Express 7(12), pp. 4286–4295, 2017; doi:10.1364/ome.7.004286.

[84] A. Penzkofer & W. Leupacher: *Fluorescence behaviour of highly concentrated rhodamine 6G solutions*. Journal of Luminescence 37(2), pp. 61–72, 1987; doi:10.1016/0022-2313(87)90167-0.

[85] J. W. Eaton, D. Bateman, S. Hauberg & R. Wehbring: *GNU Octave version 4.4.0 manual: a high-level interactive language for numerical computations*, 2018; URL `https://www.gnu.org/software/octave/doc/v4.4.0/`.

[86] A. Sukhanova, A. S. Susha, A. Bek, S. Mayilo, A. L. Rogach, J. Feldmann, V. Oleinikov, B. Reveil, B. Donvito, J. H. M. Cohen & I. Nabiev: *Nanocrystal-Encoded Fluorescent Microbeads for Proteomics: Antibody Profiling and Diagnostics of Autoimmune Diseases*. Nano Letters 7(8), pp. 2322–2327, 2007; doi:10.1021/nl070966+.

[87] M. Köllner & J. Wolfrum: *How many photons are necessary for fluorescence-lifetime measurements?* Chemical Physics Letters 200(1), pp. 199–204, 1992; doi:10.1016/0009-2614(92)87068-z.

[88] P. Hall & B. Selinger: *Better estimates of exponential decay parameters*. The Journal of Physical Chemistry 85(20), pp. 2941–2946, 1981; doi:10.1021/j150620a019.

[89] C. Würth & U. Resch-Genger: *Determination of Photoluminescence Quantum Yields of Scattering Media with an Integrating Sphere: Direct and Indirect Illumination*. Applied Spectroscopy 69(6), pp. 749–759, 2015; doi:10.1366/14-07679.

[90] M. N. Berberan-Santos, E. J. N. Pereira & J. M. G. Martinho: *Dynamics of radiative transport*; chap. 3 in Resonance Energy Transfer, pp. 108–149. John Wiley & Sons, Inc., 1999; ISBN 978-0-471-98732-1.

[91] W. Nolting: *Grundkurs Theoretische Physik 1*. Springer-Verlag Berlin Heidelberg; 8th edn., 2006; ISBN 978-3-540-34833-7; doi:10.1007/978-3-540-34833-7.

[92] S. E. Koonin: *Computational Physics*. The Benjamin/Cummings Publishing Company, Inc., 1985; ISBN 0-8053-5430-1.

Danksagung

Im Laufe der vergangenen fast vier Jahre innerhalb derer diese Arbeit und die dafür notwendigen Ergebnisse entstanden sind, haben mich diverse Freunde, Kollegen, Familienangehörige und Bekannte unterstützt – nicht nur bei der Arbeit an sich, auch persönlich – und mich damit das ein oder andere Mal vor der Verzweiflung bewahrt. Nun möchte ich mich bei all diesen Leuten möglichst gebührend bedanken und hoffe, dass ich niemanden vergessen werde.

Besonderer Dank gilt hier zuallererst Katrin, die für inhaltliche, organisatorische und moralische Fragen und Diskussionen rund um meine Arbeit und die Wissenschaft an sich immer eine geduldige Beraterin war. Sie hat sich unermüdlich für mich eingesetzt, hat mit ihrer rationalen Art Ziele gesetzt, aber auch immer klar gemacht, dass es Dinge gibt, die wichtiger als die Arbeit sind. Ob ohne Katrins Unterstützung diese Zeilen hier stehen würden, ist wenigstens fraglich.
Zudem möchte ich Ute und Stefan für die fachliche Unterstützung danken und dafür, dass dieses Promotionsvorhaben überhaupt beginnen konnte.
Nur mit Thomas, Uwe und Heike von PolyAn sowie Marc, Jens und Wolfgang von Quantum Analysis war dieses Projekt so gut, kooperativ, angenehm und erfolgreich zu bearbeiten. Insbesondere danke ich Marc und Jens für die lockere Zusammenarbeit und tolle Unterstützung bei den Mess-Besuchen in Münster, sowie Thomas für die Erfüllung immer neuer und ausgefeilterer Partikel-Wünsche. Für die Bereitstellung von weiteren Proben danke ich dem LRN der URCA.

Die Zeit im Büro wäre ohne die anderen Doktoranden und Studenten nicht so heiter gewesen. Ich freue mich, dass insbesondere Florian mich so lange im Büro ertragen hat und mir den Einstieg an der BAM erleichtert hat, und dass auch Oleks und Cui mich ausgehalten haben. Nithi hatte immer ein offenes Ohr, sowohl fachlich als auch persönlich. Ich danke Elina, Florian (F.), Lorena, Bettina, Marco und den vielen anderen für gesellige Pausen und Zusammenarbeit. Weiterhin einen Dank an Thomas (S.) und Matthias für die Präzisions-Einwaagen und die Bestimmung des Extinktionskoeffizienten, an Arne für technische Unterstützung, und an Elina und Sebastian für die Hilfe für inkompetente Physiker beim Gefriertrocknen.

Bei Katie möchte ich mich für den mentalen Ausgleich im Alltag, auf langen Wanderungen, in Urlauben, bei anderen Unternehmungen und dann sogar beim Rudern bedanken. Es ist einfach schön, jemanden bei sich zu haben, der für einen da ist und so ausdauernd mit Geduld und Verständnis unterstützt! Auch die inhaltlichen Diskussionen sowie die ausführliche Sprachkorrektur waren großartig. Ein großes Dankeschön an meine Familie, insbesondere meinen Vater der mir auch in den vergangenen vier Jahren wieder mit Pragmatismus und Tatkraft zur Seite stand und mir damit durch aufreibende persönliche und familiäre Situationen geholfen hat.

Zudem waren viele Freunde vom Ruderverein nicht nur für gute Zeiten auf dem Wasser, sondern auch am Wasser oder manchmal sogar weiter weg vom Wasser verantwortlich: nicht nur ganz besonders Karo, Rebecca und Ruth, sondern auch Charlotte, Kirsten, Dominik, Julian, Dirk und viele andere. Vom Gefrierpunkt bis zu brütender Hitze, bei Regen und Wind, von der Ausbildung bis zum 24-h-Rudern, hatten wir tolle Fahrten. Und wenn das Wasser nicht mehr flüssig war, oder auch einfach mal so, hat man halt was anderes unternommen.

Ich danke Stefan (P.) dafür, dass er da ist, wenn man Hilfe braucht. Damit es nicht klingt „als ob jemand gestorben wäre“, führe ich das nicht weiter aus. Ich danke ihm aber trotzdem noch dafür, dass er immer wieder meine Pflanzen und den Briefkasten gehütet hat, wenn ich in der Weltgeschichte unterwegs war. Mara war immer eine gute Ansprechpartnerin für Sorgen und Nöte. Natürlich nicht nur dafür, wir hatten auch viele lustige und spannende Gespräche! Zusammen mit Thomas (K.) hatten wir regelmäßig angenehm alberne Mittagspausen, aus denen man Energie schöpfen konnte. Ich freue mich auf die Firmengründung zur Herstellung von innovativen Eisbecherbroten. Andrea, Stuff und Ulli haben auch immer gute Laune verbreitet und für Zerstreuung gesorgt. Vielen Dank an euch für Ausflüge und einen sehr schönen Urlaub.

Selbstständigkeitserklärung

Ich erkläre, dass ich die Dissertation selbstständig und nur unter Verwendung der von mir gemäß § 7 Abs. 3 der Promotionsordnung der Mathematisch-Naturwissenschaftlichen Fakultät, veröffentlicht im Amtlichen Mitteilungsblatt der Humboldt-Universität zu Berlin Nr. 42/2084 am 11.07.2018 angegebenen Hilfsmittel angefertigt habe.

Berlin, den 15.05.2019 Daniel Kage